**Title**
Soil moisture in complex terrain: quantifying effects on atmospheric boundary layer flow and providing improved surface boundary conditions for mesoscale models



**Author**
Daniels, Megan Hanako

**Publication Date**
2010

Peer reviewed|Thesis/dissertation

**Soil moisture in complex terrain: quantifying effects on atmospheric boundary layer flow and providing improved surface boundary conditions for mesoscale models**

by

Megan Hanako Daniels

A dissertation submitted in partial satisfaction
of the requirements for the degree of

Doctor of Philosophy

in

Engineering – Civil and Environmental Engineering

in the

GRADUATE DIVISION

of the

UNIVERSITY OF CALIFORNIA, BERKELEY

Committee in charge:

Professor Fotini K. Chow, Chair
Professor Mark T. Stacey
Professor Jon Wilkening
Professor Reed M. Maxwell

Fall 2010

Soil moisture in complex terrain: quantifying effects on atmospheric boundary layer flow and providing improved surface boundary conditions for mesoscale models



by

Megan Hanako Daniels

## Abstract

Soil moisture in complex terrain: quantifying effects on atmospheric boundary layer flow and providing improved surface boundary conditions for mesoscale models

by

Megan Hanako Daniels

Doctor of Philosophy in Engineering – Civil and Environmental Engineering

University of California, Berkeley

Professor Fotini K. Chow, Chair

Soil moisture affects flow in the atmospheric boundary layer (ABL) through relative partitioning of surface energy fluxes. Surface conditions significantly affect flow in the ABL under quiescent synoptic conditions (weak forcing) over flat terrain, but strong wind forcing often dominates land surface effects. Over complex terrain, it is unclear what role soil moisture plays. Due to a lack of data at the appropriate resolution, surface conditions are often interpolated from coarse grids as part of a standard intialization procedure for mesoscale atmospheric models. In this work, simulations of the ABL are performed using the Advanced Regional Prediction System (ARPS) in a horizontally nested grid configuration for the complex terrain of Owens Valley, California, site of the Terrain-Induced Rotor Experiment (T-REX) in March and April, 2006. Effects of surface conditions on simulations of ABL flow in complex terrain under both weak and strong synoptic forcing are investigated through a sensitivity study and through comparisons to observations. Coupled hydrologic modeling using PF.CLM, a coupled groundwater-land-surface model, is presented as a physically-based alternative to standard initialization procedures. Soil moisture measurements were carried out during T-REX and are used to validate results of the coupled hydrologic modeling. Results of the sensitivity study indicate that simulations of the ABL are sensitive to surface soil moisture initialization under both weak and strong synoptic forcing. Comparisons of simulation results to observations show significant improvements in most simulations with more accurate soil moisture. Coupled hydrologic modeling is a promising alternative to standard initialization procedures; even simple two-dimensional simulations successfully capture soil moisture trends across Owens Valley. Simple adjustments to standard initial soil moisture based on field observations yield significant improvements in comparisons to observations as well.

# Contents

# List of Figures

# List of Tables

## Acknowledgements

Thank you to my friends and colleagues in the Environmental Fluid Mechanics group at Berkeley. To my advisor, Prof. Tina Chow for sharing with me her energy and enthusiasm, and for allowing me to study the mountains of California that I love so well. To my mentor, Prof. Reed Maxwell for giving my research a whole new perspective. To Prof. Mark Stacey for introducing me to environmental fluid mechanics. To Prof. Jon Wilkening for his excellent teaching of graduate level mathematics, which I could appreciate even though I am en engineer. Special thanks to Katie Lundquist, Maureen Downing-Kunz, Lissa MacVean, Mary Cousins, and Rebecca Leonardson for many helpful discussions on the topic of fluid mechanics as well as other facets of life! Thanks also to Bowen Zhou, Rudi Schuech, Rusty Holleman, Andreas Brand, Paul Koster Van Groos, Beverly Coleman, and Jean Toilliez for your help along the way.

Thank you to the members of my family, who have supported me in all my endeavors. To my grandmother, Lily Ikuta who has always been a good listener and provider of positive outlooks on any situation. To my cousins, Benjamin and Amelia who always impress me with both their eagerness to learn and their aptitude for it, and to their supportive parents, Phil and Judy Ikuta, who find the energy to support me as well! Uncle Frank, Aunt Janet, Uncle Steve and Aunt Marilyn, thanks for all your support over the years. To my sister, Brianne Daniels, thanks for living nearby and always being there for me. And thank you to my parents, John and Joanne Daniels for instilling in me a love of science and learning in general and for being steadfastly supportive through my 25 years in school!

## Curriculum Vitæ

Megan Hanako Daniels

### Education

| | |
|---|---|
| 2003 | California State University, Long Beach<br>B.S., Mechanical Engineering |
| 2005 | University of California, Berkeley<br>M.S., Civil and Environmental Engineering |
| 2010 | University of California, Berkeley<br>Ph.D., Civil and Environmental Engineering |

# Chapter 1

# Introduction

High-resolution simulations of atmospheric boundary layer flow can be particularly sensitive to surface boundary conditions including soil moisture and snow cover. The extent to which surface conditions affect the atmospheric boundary layer under certain meteorological forcings is only partially understood because much of the previous work in this area has focused on flat terrain. Weather prediction and environmental problems often arise in regions of complex terrain and surface heterogeneity. Both topography and surface heterogeneity can have a significant influence on the nature of a mesoscale flow. Mesoscale models are used for regional weather prediction as well as to investigate regional environmental problems such as pollutant transport and dispersion. To effectively tackle these problems, a better understanding of how surface conditions affect atmospheric boundary layer flow in complex terrain is needed, in addition to better methods of providing surface boundary conditions to mesoscale models. This dissertation focuses on two main scientific objectives: 1) to quantify the effects of conditions at the land-surface on simulations of atmospheric boundary layer flow in complex terrain 2) to investigate methods for providing more accurate surface conditions to mesoscale models.

## 1.1 Background

The earth's atmosphere can be divided into four layers defined by alternating decreases or increases in air temperature with height. These are: the troposphere, stratosphere, mesosphere, and thermosphere. The troposhere can be divided into two parts: the atmopheric boundary layer, and the free atmosphere. Flow in the atmospheric boundary layer (ABL) is driven partially by the synoptic (on the order of many hundreds of kilometers) scale flow of the free atmosphere above. We live and breathe inside the atmospheric (or planetary) boundary layer, the layer next to the earth's surface which is directly affected by surface frictional drag, solar heating, and evapotranspiration. The ABL contains many mesoscale flows ranging from mountain-valley wind circulations to land and sea breezes to thunderstorms. Mesoscale flows (flows with length scales on the order of one to several hundred km) often arise in regions of complex terrain because the topography constrains the flow scales. These flows aid in the transport of moisture from the surface up into the atmosphere,

as well as transport of pollutants emitted near the surface. Thus a good understanding of the dynamics of mesoscale flows and how they interact with the land-surface as well as an ability to numerically predict them are essential to understanding and solving environmental problems in the atmosphere.

Land-surface characteristics such as soil and vegetation types, as well as conditions such as soil moisture and snow cover tend to vary with topography. Soil moisture, for example will tend to follow surface run-off and groundwater flow patterns which are linked to the topography. Valleys are topographical features which tend to have higher soil moisture at their centers, where a stream or river flows. Air flowing over the land surface is heated or cooled based on the partitioning of energy into the sensible and latent heat fluxes, which which either heat air, or evaporate water, respectively. Thus land-surface-atmosphere coupling is important in understanding flow in the ABL.

The ABL is characterized by turbulent flow, that is, a wide range of length and time scales, unsteadiness, three dimensional flow structure, high levels of vorticity, mixing, and dissipative processes. The broad range of length and time scales present in turbulent flow make numerical simulation of such flows a challenge since all scales must be computed in order to fully describe the flow.

### 1.1.1 Modeling

#### Numerical modeling of turbulent flows

Numerical simulation of turbulent flows can be accomplished by several general methods: Reynolds-Averaged Navier-Stokes (RANS), Large-Eddy Simulation (LES), or Direct Numerical Simulation (DNS). In RANS models, the Navier-Stokes equations are averaged in time, and the resulting additional covariance term, or "Reynolds stress" is modeled using a turbulence closure such as an eddy viscosity model (in which it is assumed that the "eddy viscosity" for turbulent motions is analogous to molecular viscosity for molecular motions). RANS is a very simplified approach to modeling turbulent flows since it is only able to solve for average quantities. Direct Numerical Simulation (DNS) on the other hand involves specifying a grid which is fine enough to resolve all motions contained in the flow. Advances in computational power continue to allow DNS to be performed for ever more complex flows. Even so, it is not computationally feasible to perform DNS for ABL flow due to the prohibitively broad range of length and time scales involved. That is, the size of the computational grid required for DNS of the ABL would be too large given our current and forseeable computational resources. Large-Eddy Simulation (LES) is an approach that combines the accuracy of DNS (down to a specified grid spacing) with a turbulence closure approach similar to that used in RANS. This is accomplished by spatially filtering the Navier-Stokes equations such that all motions smaller than the filter width (often related to the grid spacing) are not resolved, and are instead modeled using a turbulence closure. The resolution problem faced by DNS is thus circumvented by simulating only those motions which are larger than the filter width. Over the past decade LES has been increasingly used to model the ABL.

LES is a useful tool for modeling mesoscale flows in the ABL, but there are still limitations on the computational domain size. For example, the size of the computational domain required to perform LES for the whole planet would be prohibitively large. It is however possible to perform

LES as a limited area model such that the domain covers a small portion of the earth's surface. For example, running a simulation of ABL flow over a 24 hour period for a domain 50 km by 50 km in the horizontal, by 20 km in the vertical, with a computational grid of 144 points in both hortizontal directions (horizontal grid spacing of 350 m) and 60 points in the vertical takes about 24 hours to run on 64 processors. Thus a simulation only covering a small portion of Earth's surface already requires a significant amount of computational resources. General circulation models (GCMs) are used to simulate synoptic scale flows for the entire planet. Boundary conditions can be extracted from GCMs to force mesoscale simulations (LES or otherwise). Since the mesoscale itself covers scales ranging from a few to many hundreds of kilometers, it is also possible to have a mesoscale model covering for example the entire North American continent which provides interpolated lateral, surface, and even top boundary conditions to other mesoscale models that have finer resolution and smaller physical domains defined within the larger or "parent" domain. Such "grid nesting" of finer resolution models within coarse domains is commonly used to obtain initial and boundary conditions for fine grids.

**Coupled hydrologic modeling**

Field measurements of soil moisture are often sparse, and standard intialization datasets are most often at coarse resolution compared to complex terrain features that affect the soil moisture distribution. It is therefore useful to employ a coupled hydrologic model to obtain high-resolution surface boundary conditions for atmospheric models. Standard land-surface models used to provide surface conditions often do not include lateral flows because they were developed to be used on coarse grids with relatively flat topography. In steep terrain, lateral flows can be significant and can greatly influence patterns of soil moisture in the region.

When modeling lateral flows, grid resolution of the digital elevation model (DEM) greatly influences the outcome. It is often the case that hydrologic features such as rivers and streams, important in determining accurate soil moisture fields, are not resolved at the given grid resolution. Thus it becomes necessary to find ways in which to include these features at coarse resolution. A combination of methods (discussed in Chapter 4) are employed in this research, including direct modification of the DEM, as well as continuous flow routing by ensuring continuous slopes along a river flow path.

The coupled hydrologic model used in this dissertation work (discussed in Chapter 3) includes three main components which allow modeling of lateral flows: the land-surface, surface water, and groundwater. Each component must be modeled and provide feedbacks to the others. Thus fluxes at the land-surface are modeled and provided as boundary conditions to the groundwater model coupled to an overland flow solver. The groundwater model and overland flow solver then provide soil moisture values to the land-surface model. In this way, physically-based modeling of the land-surface-surface water-groundwater system is achieved through a multi-year spin-up procedure which is in some way and approximation of the processes which occur on a geologic time-scale.

## 1.2 Motivation

For high-resolution simulations of atmosperhic boundary layer flow, problems arise when interpolating coarse initial and boundary conditions down to fine grids. In particular, surface boundary conditions can be distorted or inappropriate for the higher resolution terrain on the fine grid. This can lead to prediction of incorrect surface fluxes and circulations.

Surface boundary conditions such as soil moisture can be grossly misrepresented if the coarse grid has a grid spacing that is larger than the topographical features of interest on the finer grid or grids. An example of this issue is illustrated in Figure 1.1 where soil moisture and snow cover from the 12 km North American Mesoscale Model (NAM) and 32 km North American Regional Reanalysis (NARR) are shown interpolated onto a high-resolution grid (horizontal grid spacing of 1 km) for a section of Owens Valley in California. The coarse grids of NAM and NARR are unable to resolve the valley, so that in both cases, snow cover and elevated soil moisture levels (corresponding to artificially elevated terrain on the coarse grid) spread across the valley floor on the fine grid. Values of parameters such as soil moisture, soil temperature, and snow depth may have little or no meaning on the fine grid if they come from a coarse grid that cannot resolve the hills or valleys that determine their distributions. *Chow et al.* [2006b] found that increasing spatial resolution for nested LES was only beneficial if more accurate surface data were incorporated. Though remote sensing techniques for soil moisture and other surface properties are currently being explored [*Krajewski et al.*, 2006], there are no reliable databases yet available. Thus in order to obtain accurate surface data, take soil moisture for example, it is necessary either to directly measure soil moisture in the field, or to run a land surface-groundwater or other hydrologic model for the region under consideration. The issue of providing more accurate surface boundary conditions to finer grids is addressed in the later chapters of this dissertation.

Another question that arises in complex terrain has to do with how strongly surface conditions affect flow in the ABL under different synoptic conditions. Much work has been done to investigate the effects of surface heterogeneity on ABL flow over flat terrain, e.g. [*Patton et al.*, 2005; *Kang and Davis*, 2008; *Huang and Margulis*, 2009] and many others. Flat terrain provides the simplest case under which to study the physical mechanisms at work in the ABL. It follows that many stardard parameterizations and modeling practices were developed in the context of flat terrain. As computational resources have expanded to include complex terrain, these parameterizations and practices continue to be applied, though their validity in complex terrain has not necessarily been established. One particular modeling "rule of thumb" is that surface conditions such as soil moisture only affect ABL flow under calm synoptic conditions, and not under strong synoptic forcing. This is generally true for flat terrain, but may not hold for complex terrain, as is discussed in Chapter 2.

### 1.2.1 Study site: Owens Valley, California

Owens Valley in California was selected to study flows over complex terrain under realistic conditions because there is a large set of atmospheric and land surface data with which to initialize and compare. Owens Valley is located in southeastern California, on the eastern side of the Sierra Nevada mountain range. It is a topographic feature large enough to be visible from satellite images like the one shown in Figure 1.2 taken from MODIS in Fall of 2004 just after a big storm.

Owens Valley is characterized by its long (approximately 120 km) and relatively straight valley

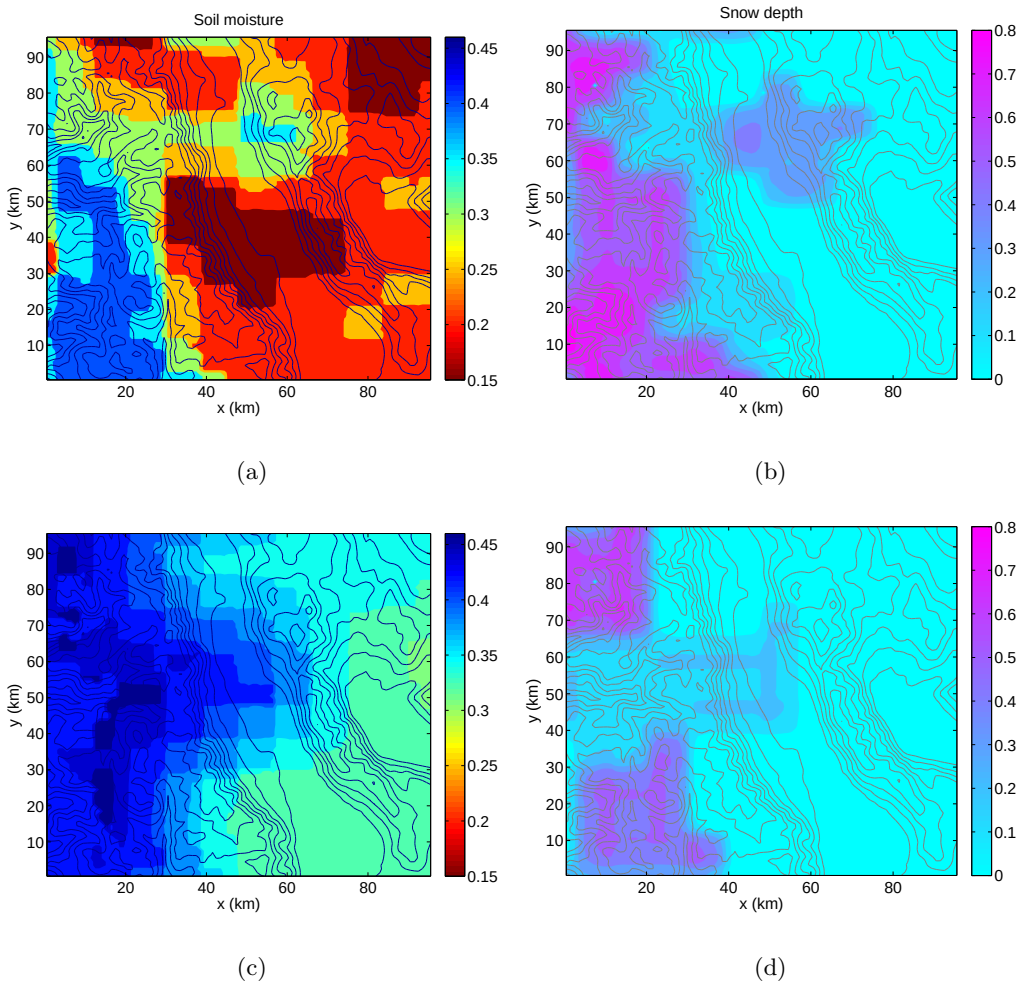


Figure 1.1. Interpolated soil moisture ($m^3/m^3$) and snow depth (m) from NAM (12 km, top row) and NARR (32 km, bottom row). Contours are terrain height (m) for a section of Owens Valley at 1 km resolution centered at Independence, California.


Figure 1.2. MODIS satellite image of California on October 31, 2004. Owens Valley (below center right) is free of snow, in contrast to the blanketed Sierra Nevada and Inyo-White mountains.

walls formed by the Sierra Nevada Mountains on the west and the White-Inyo Mountains to the east. The peaks of the Sierras reach higher than 4.3 km above sea level (ASL); in stark contrast, the valley floor lies at just 1.2 km ASL. A schematic of Owens Valley from *Danskin* [1998] is shown in Figure 1.3. The terrain of Owens Valley is both complex and unique, making it an interesting site for investigation of atmospheric boundary layer flow. In addition to having widely varying topographical features, Owens Valley possesses heterogeneous surface conditions including variations in soil moisture, soil type, vegetation, and land use, all of which can contribute to variations in surface fluxes.

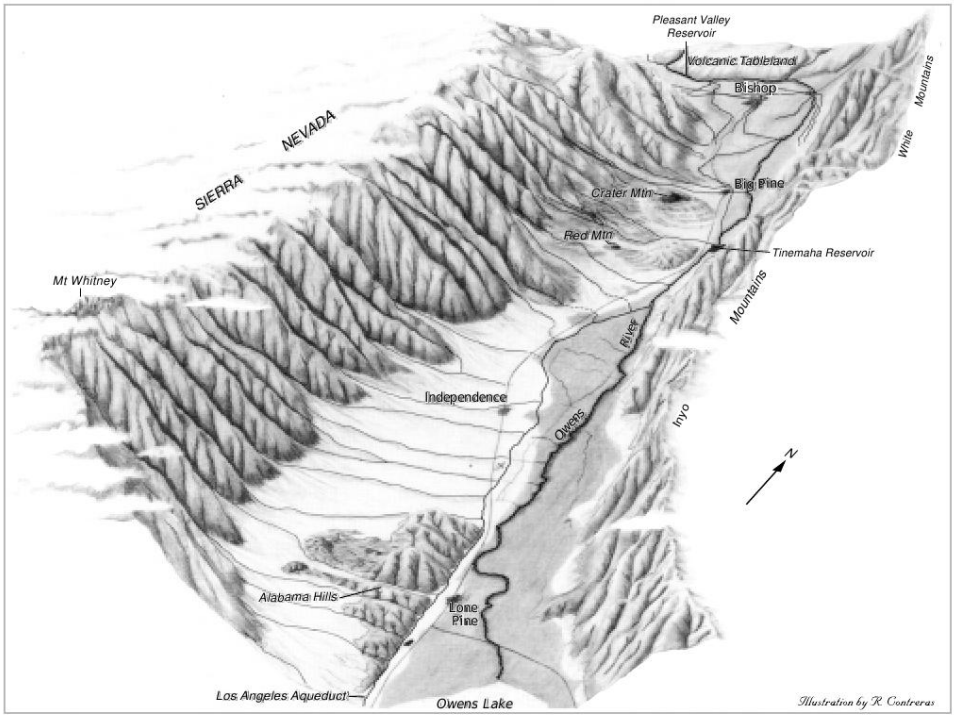


Figure 1.3. Drawing of Owens Valley from *Danskin* [1998], (Frontispiece, Credit: U. S. Geological Survey U. S. Geological Survey/drawing by R. Contreras).

Under calm synoptic conditions, valley wind structure is dominated by thermal forcing. In general, during the day heating of valley side walls induces upslope and up-valley winds, while cooling at night induces downslope and down-valley winds [*Whiteman*, 2000; *Rampanelli et al.*, 2004]. Incoming shortwave radiation from the sun heats the ground surface; air near the surface heats more quickly than air further away, creating a difference in buoyancy that drives valley circulation. Because this circulation depends on the partitioning of energy between sensible and latent heating, that is, heating of the air versus heat used to evaporate water from the soil surface, the amount of moisture present in the soil at the surface can have an important role in determining the nature and development of the valley circulation. A schematic of upslope flows in a valley cross-section is shown in Figure 1.4(a) and photographs in Figure 1.5 show the calm wind conditions during Enhanced Observation Period 2 (EOP2) of the Terrain-Induced Rotor Experiment (discussed in section 1.2.2).

Under strong synoptic conditions, the valley wind structure is mostly determined by the synoptic

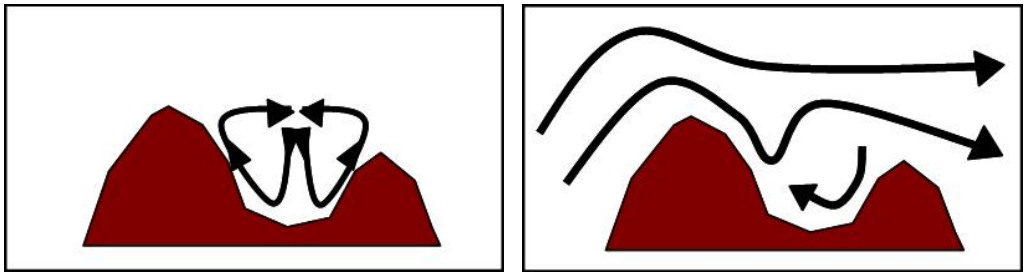

(a) (b)

Figure 1.4. (a) Schematic of valley circulations under calm synoptic conditions. (b) Schematic of rotor circulation under strong synoptic conditions.

(a) (b)

Figure 1.5. (a) Clear sky and calm winds (slack wind sock at lower left-of-center), looking north from the center of Owens Valley, California (Independence Airport) with the Sierra Nevada mountains left and Inyo mountains right. (b) Looking east, toward the Inyos. Both photographs were taken during EOP2 of T-REX (March 30, 2006).

scale flow. Dynamically-driven circulations can develop within the valley, allowing air parcels to circulate within and above the valley and come in contact with the land surface repeatedly. Such dynamically-driven events are referred to as atmospheric rotors, or heated pressure jumps. As the name implies, these types of flows are analogous to a hydraulic jump in water, but the role of surface heating is considered to be significant in the atmospheric case [*Kuettner*, 1959; *Jiang and Doyle*, 2008; *Smith and Skyllingstad*, 2009]. Thus for simulations of these types of dynamically-driven flows, the importance of surface conditions, and soil moisture initialization in particular, is unclear. A schematic and a photograph of rotor flow are shown in Figures 1.4(b) and 1.6 respectively, as well as in Figure 1.7.

(a) (b)

Figure 1.6. (a) Rotor cloud and dust plumes looking north from the center of Owens Valley (near Independence, California) with the Inyo mountains to the right. (b) Rotor cloud looking south over Mono Lake in California with the Sierra Nevada mountains to the right. Winds are from the west. Both photographs were taken during IOP6 of T-REX (March 24-25, 2006).

### 1.2.2 Terrain-Induced Rotor Experiment

Owens Valley was the site of the Terrain-Induced Rotor Experiment (T-REX) which took place in March and April, 2006 [*Grubišić and Kuettner*, 2004; *Grubisic et al.*, 2008]. The main scientific objectives of T-REX included investigating the dynamics of atmospheric rotors and lee waves in Owens Valley, with broader objectives including boundary layer development over complex terrain, and stratospheric-tropospheric exchange. In addition, T-REX is meant to provide extensive datasets to validate numerical models and improve the accuracy of mesoscale and microscale modeling so that better prediction of aviation hazards, downslope windstorms, as well as transport and dispersion of aerosols can be achieved.

During T-REX, an Enhanced Observational Period (EOP) lasted approximately 21 hours and focused on the complex terrain ABL under quiescent (calm) synoptic conditions. An Intensive Observational Period (IOP) lasted from 24 to 48 hours, depending on conditions, and focused on observations of mountain lee waves and rotor events under strong synoptic conditions (strong winds).

A variety of instruments were used during T-REX to gather information about the atmospheric

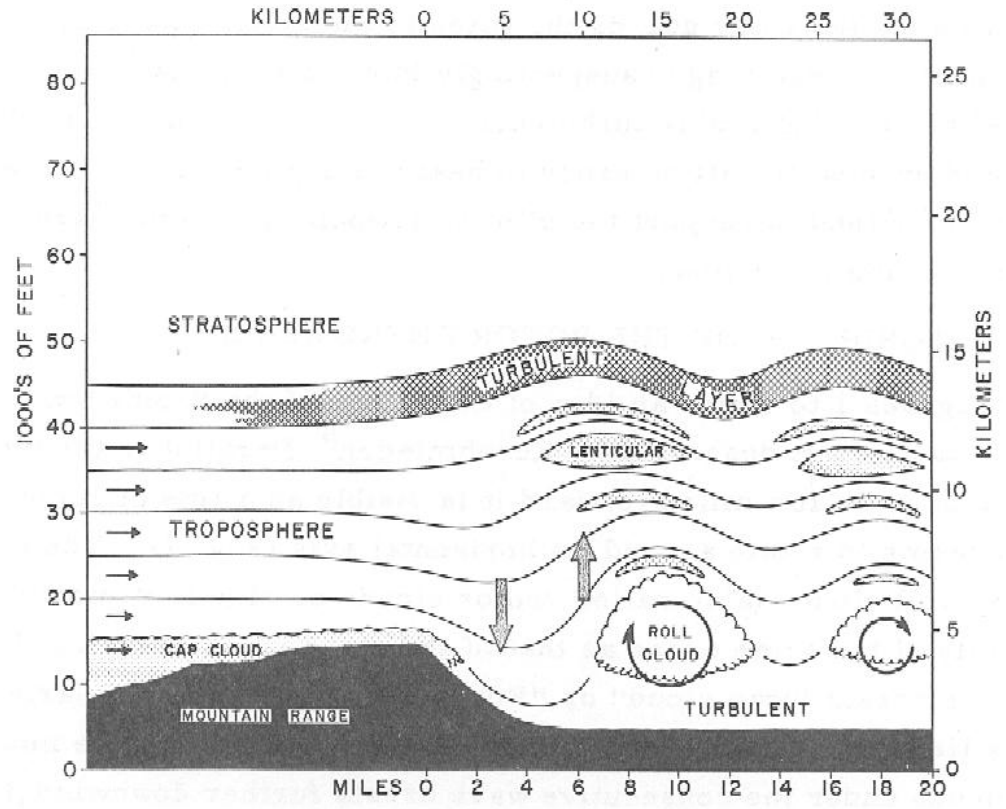


(a)

(b)

Figure 1.7. (a) Schematic of rotor flow from *Kuettner* [1959], (Figure 2). (b) Looking north from Independence Airport (center of Owens Valley) with view of rotor "roll" cloud beneath lenticular cloud at 7am PST on March 25, 2006 during IOP6 of T-REX. Winds are from the west.

conditions in Owens Valley. These included: rawinsondes, dropsondes, lidars, flux towers, and soil moisture and temperature sensors, aircraft measurements among others [*Grubišić et al.*, 2004; *Grubisic et al.*, 2008]. *Chow et al.* [2006b] found that valley wind transitions in the Riviera Valley in Switzerland were particularly sensitive to soil moisture initialization. This finding prompted the collection of soil moisture and temperature data at 23 sites in Owens Valley during T-REX discussed in Chapter 5.

## 1.3 Overview

To gain a better understanding of the extent to which surface soil moisture initialization can potentially affect atmospheric boundary layer flow in complex terrain, and in Owens Valley in particular, simulations were carried out using the Advanced Regional Prediction System (ARPS) [*Xue et al.*, 2000, 2001, 2003] for EOP2 (calm winds) and IOP6 (strong winds) of T-REX. ARPS is a fully three-dimensional, nonhydrostatic, compressible numerical weather prediction model with generalized terrain-following coordinates. Large-eddy simulation (LES) mode was used with a 1.5 TKE closure [*Deardorff*, 1980; *Moeng*, 1984].

Chapter 2 focuses on quntifying effects of surface soil moisture initialization by comparing results of simulations initialized with completely dry and fully saturated soil moisture values. These simulations are meant to bracket the realm of reality, showing the biggest soil moisture-induced differences possible. Simulations were carried out for EOP2 and IOP6. While it is generally accepted that surface conditions play a significant role in determining the valley flow structure under calm wind conditions, their role under strong wind conditions has not been thoroughly investigated and remains unclear. Results indicate that surface soil moisture initialization has as great an effect on atmospheric boundary layer flow in Owens Valley under strong wind conditions as under calm wind conditions.

Chapter 3, investigates methods for predicting more accurate soil moisture fields. This is accomplished through the use of a fully coupled land-surface-surface water-groundwater model. Chapter 4 addresses flow routing through stream networks, a component which is essential to accurate simulation of the surface-subsurface flows within Owens Valley. A novel algorithm is introduced, which employs stream location data for more realistic overland flows.

Chapter 6 draws directly from the results of Chapters 3, 4, and 5 to initialize soil moisture throughout the valley region for simulations of ABL flow using ARPS. In this chapter, the goal is to provide the most accurate soil moisture field possible, so that simulation results can be compared to observations of air temperature, humidity, and winds from T-REX. Results of simulations initialized with standard NAM and NARR soil moisture fields are compared to simulations using alternative initialization procedures based on results of hydrologic modeling and comparisons to observations of soil moisture in the valley during T-REX.

## 1.4 List of contributions

In summary, the main contributions of this research are listed below:

1. Simulated ABL flow in Owens Valley at 350 m resolution under strong and weak synoptic forcing; showed strong sensitivity to soil moisture initialization under both forcings through heat budget analysis.

2. Simulated coupled land-surface-surface water-groundwater system for a representative two-dimensional slice of Owens Valley with heterogeneous subsurface geology, surface soil types and vegetation; showed that observed patterns in soil moisture can be captured by this two-dimensional simulation.

3. Developed set-up for full three-dimensional coupled land-surface-surface water-groundwater modeling of Owens Valley with heterogeneous subsurface geology, surface soil types and vegetation; showed that soil moisture patterns generally follow topography for Owens Valley.

4. Developed novel algorithm for flow direction enforcement along stream paths using stream location data for more accurate simulation of surface flows even at relatively coarse resolution; demonstrated application of this algorithm for a section of Owens Valley under rain and recession conditions.

5. Collected field observations of soil moisture in Owens Valley, California, during the Terrain-Induced Rotor Experiment, and performed custom calibration; showed that soil moisture sensors were able to capture increases in soil moisture after rain events as well as during snowmelt.

6. Simulated ABL flow in Owens Valley using soil moisture initialization derived from coupled hydrologic modeling and field observations of soil moisture. Compared these simulations to observations of air temperature, humidity, and winds from T-REX; showed that in general, more accurate initial soil moisture led to better comparisons with observations.

# Chapter 2

# Sensitivity tests for soil moisture initialization under strong and weak meteorological forcing

## 2.1 Introduction

Presented here is a sensitivity study focused on determining the extent to which surface soil moisture initialization affects flow in the atmospheric boundary layer under both weak and strong meteorological forcings. Results of this investigation provide evidence for the need of more accurate high-resolution soil moisture data, which is the subject of Chapter 3.

## 2.2 Background

Complex terrain affects boundary layer flow by inducing thermally-driven flows along slopes as the land surface heats and cools with the diurnal cycle, as well as dynamically-driven flows under strong synoptic forcing. The heterogeneous land surface conditions that exist in complex terrain futher complicate boundary layer flow in regions of hilly or mountainous topography. Soil moisture in particular affects flow in the atmospheric boundary layer (ABL) because it changes the relative partitioning of energy into the sensible and latent heat fluxes. It is known that thermal effects tend to dominate flow under quiescent conditions in complex terrain such as mountain valleys, but under strong wind conditions the role of surface heating is unclear.

Under calm conditions in valleys, a general picture of the expected behavior of wind systems has emerged, classifying winds as up-slope and up-valley during the day, and down-slope and down-

valley at night, with the breakup of a nocturnal inversion layer during the day leading to a well-mixed valley atmosphere [*Whiteman*, 2000; *Rampanelli et al.*, 2004]. These flow transitions and the thermal structure of the valley atmosphere are often affected by irregularities in valley geometry [*Weigel et al.*, 2006], synoptic flow forcing [*Schmidli et al.*, 2009], or land-cover heterogeneities [*Chow et al.*, 2006b]. While strong winds can produce dynamically-driven flows such as rotor flow, such flows are also affected to a certain extent by surface heating. Thus rotor flow is sometimes referred to as a "heated pressure jump", [*Kuettner*, 1959] somewhat analogous to a hydraulic jump in water. Surface heating is present under strong synoptic forcing as well, and the question arises: does strong synoptic forcing dominate flow structure in complex terrain, or is thermal forcing of similar importance under such conditions?

To explore this question, we will use a mesoscale numerical model to look at how changing the partioning of energy at the surface into sensible (heating of the air near the surface) and latent (evaporation or condensation of water at the surface) heat fluxes affects ABL flow over complex terrain under calm and strong wind conditions. The amount of water present in soil at the ground surface affects evaporation and transpiration, and can even change the albedo of the soil.

One rule of thumb that has developed among modelers over the years is that under quiescent synoptic conditions, surface conditions such as soil moisture affect the ABL, while under strong synoptic forcing, they do not. This rule of thumb has been tested and is applicable to flat terrain, as evidenced by papers focusing on effects of surface heterogeneity on the convective boundary layer over flat terrain. *McCumber and Pielke* [1981] found that soil moisture was the most important soil characteristic in determining the strength of heat fluxes between the ground and atmosphere. A study by *Ookouchi et al.* [1984] showed that the intensity of thermally induced circulations over flat terrain with non-homogeneous soil moisture approaches that of sea-breeze circulations when there are large differences in soil water content. Even small amounts of water contained in a patch of soil adjacent to a dry patch induce significant mesoscale flows according to their study. Idealized surface heterogeneity in the form of wet and dry strips investigated by *Patton et al.* [2005] was shown to significantly change the surface fluxes and drive local circulations. Surface heterogeneity effects over flat terrain is still a topic of ongoing research, e.g *Kang and Davis* [2008]; *Huang and Margulis* [2009] and many others.

There have been some studies focusing on effects of surface soil moisture in sloping or complex terrain under quiescent conditions. *Banta and Gannon* [1995] showed that a wet slope produces weaker katabatic (downslope) flows than a dry slope due to the increased thermal conductivity of moist soil and an increased downward longwave radiation flux from the atmosphere as a result of higher humidity in the air near the surface. Previous work in the Riviera Valley in the Swiss Alps showed that soil moisture initialization was a very sensitive parameter for correct prediction of valley wind transitions [*Chow et al.*, 2006b]. The onset of up-valley winds in the Riviera was delayed by 3-4 hours in initial simulations compared to observations. Initializing with soil moisture fields from a hydrologic model (WaSiM-ETH) reduced the delay to 1-2 hours, illustrating the importance of land-surface characteristics and the need for accurate specification of these bottom boundary conditions [*Chow et al.*, 2006b]. Thus under weak synoptic forcing, flow over complex or flat terrain is sensitive to surface conditions.

Over flat terrain, the significant vertical motions of convective cells that form under weak forcing do not have time to form under strong synoptic forcing. Instead, air moves across the flat land surface and through the domain faster than the time needed for significant heat transfer to occur. In contrast, for strong synoptic forcing in complex terrain, dynamically-driven circulations can develop, which can increase the amount of time an air parcel stays within the domain, or within

a mountain valley, for example. This increased residence time in the valley allows air parcels to be in contact with the land surface for longer, on average, than they would be if they traveled straight across a domain of flat terrain. Hence, the rule of thumb is not necessarily applicable over complex terrain. This concept is illustrated in Figure 2.1.

Many studies of flows over complex terrain focus on the dynamics of the flow in an idealized framework, employing prescribed fluxes at the surface and neglecting surface heterogeneity, e.g. *Doyle and Durran* [2002, 2007]; *Jiang and Doyle* [2009]; *Smith and Skyllingstad* [2009]; *Reinecke and Durran* [2009] and others. *Doyle and Durran* [2002] investigated effects of surface heating on the lee side of a bell-shaped mountain for two-dimensional rotor flow and found that the strength of the reversed flow decreased by more than 50% and the depth of the circulation nearly doubled compared to the simulations with no heating, even with very weak surface heat flux (50 $W/m^2$). *Smith and Skyllingstad* [2009] found that surface heating and cooling significantly affected rotor flow over a two-dimensional bell-shaped ridge in a three-dimensional domain. *Jiang and Doyle* [2008] investigated the diurnal patterns in rotor flow over Owens Valley during the Sierra Rotors Project and found strong diurnal variation with diurnal changes in surface fluxes. Prescribed fluxes may be sufficient in some cases, but the heterogeneity often associated with complex topography can make their use undesirable when attempting to simulate realistic conditions and compare to field observations. Fluxes calculated by land surface models at coarse resolutions are sometimes interpolated onto finer grids and used as boundary conditions, but these can cause problems as well if important land-surface heterogeneities are not resolved on the coarse grid. Furthermore, values of surface conditions like soil moisture may be far off from observed values, e.g. North American Regional Reanalysis (NARR) has values of soil moisture in the Owens Valley region which are approximately three times the observed values. Given the wide range of values that may be used for standard initialization procedures, it is logical to study the conditions which are at the limits of those encountered in reality. This study is also motivated by previous work [*Chow et al.*, 2006b; *Daniels et al.*, 2006, 2008], which has demonstrated model sensitivity to surface soil moisture initialization in complex terrain.

In short, our hypothesis is that surface conditions can siginificantly affect flow in the atmospheric boundary layer in complex terrain under both weak and strong inflow conditions, while they are only important in flat terrain under weak inflow conditions.

To investigate effects of surface conditions on dynamically-forced flows as well as thermally-forced flows in a mountain valley, we have selected Owens Valley in California as our case study site. Owens Valley is a rift valley in southeastern California which lies between the eastern slopes of the Sierra Nevada mountain range and the western slopes of the White Mountains and the Inyo Mountains. The peaks of the Sierras reach above 4,300 m while the valley floor lies at about 1,200 m, making it one of the deepest valleys in the United States. The valley is about 120 km in length and runs approximately north-south. Owens Valley was the site of the Terrain-Induced Rotor Experiment which took place in March and April, 2006. The field campaign focused on the dynamics of atmospheric rotors and lee waves, which occur under strong atmospheric forcing conditions, with broader scientific objectives including boundary layer development under quiescent conditions [*Grubišić et al.*, 2004]. In this investigation, effects of soil moisture initialization in the complex terrain of Owens Valley under both strong and weak (quiescent) synoptic conditions will be explored and quantified through a heat budget analysis. Real atmospheric forcing is combined with idealized soil moisture conditions to evaluate the role of land-surface forcing. Simulations are performed using the Advanced Regional Prediction System (ARPS).

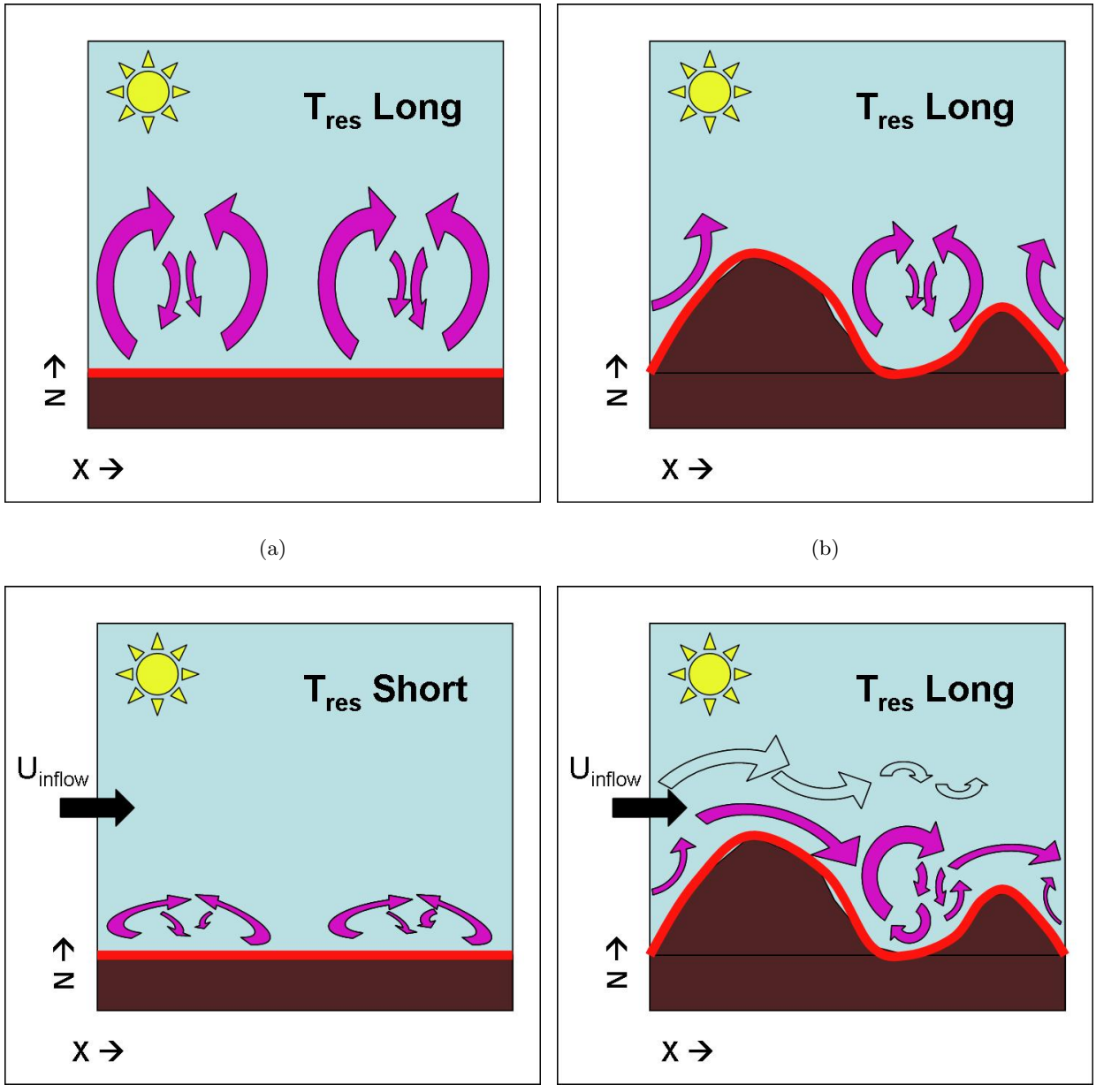


Figure 2.1. Weak forcing: (a) flat terrain and (b) mountain valley slice. Strong forcing: (c) flat terrain and (d) mountain valley slice. $U_{inflow} < 10m/s$ under weak forcing, ($U_{inflow} = 0m/s$ in the limit). $U_{inflow} > 25m/s$ under strong forcing.

Table 2.1. Simulation parameters for each grid level.

| (nx,ny,nz) | $\Delta h$ | $\Delta z_{min}$,$\Delta z_{avg}$ | $\Delta t$,$\Delta \tau$ |
|---|---|---|---|
| (103,103,53) | 3 km | 40 m, 500 m | 2 s, 4 s |
| (99,99,63) | 1 km | 40 m, 400 m | 1 s, 1 s |
| (147,147,63) | 350 m | 30 m, 350 m | 0.5 s, 0.1 s |

## 2.3 Model set-up

ARPS is a comprehensive regional to storm-scale modeling and prediction system [*Xue et al.*, 2000, 2001, 2003]. It is a fully three-dimensional, nonhydrostatic, compressible numerical weather prediction model in generalized terrain-following coordinates and includes a full postprocessing package. Computations were performed using 16 to 64 processors at the Scientific Computing Division of the National Center for Atmospheric Research (NCAR). ARPS is used here in large-eddy simulation (LES) mode with a 1.5 TKE turbulence closure [*Deardorff*, 1980; *Moeng*, 1984].

### 2.3.1 Grid nesting and topography

A one-way nested grid configuration was used with 3 km, 1 km, and 350 m horizontal grid resolutions (see Table 2.1 and Figure 2.3.1). Topography for all grid resolutions was obtained using the USGS 3 arcsecond topography dataset. The terrain is smoothed at the edges of each subdomain so that the elevations at the boundaries match those of the surrounding coarser grid.

Horizontal grid spacing ($\Delta h$) is uniform in both directions. In ARPS, the minimum vertical spacing ($\Delta z_{min}$) is near the ground in a terrain-following $\sigma$-coordinate system. This minimum spacing, as well as the average vertical spacing ($\Delta z_{avg}$) are shown in Table 2.1. The domain height ($\sim$ 25 km) extends beyond the tropopause. Large ($\Delta t$) and small ($\Delta \tau$) time steps must be specified in the mode-splitting scheme used in ARPS (see Table 2.1). These selections of grid spacing, time steps, and other parameters such as computational mixing coefficients, were made using experience gained through previous simulations over complex terrain [*Chow et al.*, 2006b; *Weigel et al.*, 2006].

### 2.3.2 Initialization and lateral boundary conditions

Initial and boundary conditions are set using data from the National Oceanic and Atmospheric Administration (NOAA) North American Mesoscale Model (NAM) dataset which is available at 12 km resolution with 39 vertical levels. Relaxation towards the lateral boundary conditions was applied in a 12 grid-cell zone around the edge of the 3 km domain. NAM forcing was available at 6-hour intervals; linear interpolation was used at intermediate times. A spin-up of 11 hours was used for each simulation. Output was saved at hourly intervals for the 3km grid, and half-hourly intervals for the 1km and 350m grids. This output data was then interpolated and used as initialization data for subsequent simulations at finer grid resolutions.

All surface conditions except soil moisture and snow cover were interpolated directly from NAM. Snow cover was taken from NAM, but then modified to better match the terrain on the ARPS grids. A snow level of 2500 m was imposed on all grids to remove snow on the valley floor, (which is present in NAM due to interpolating conditions from a comparatively coarse grid which

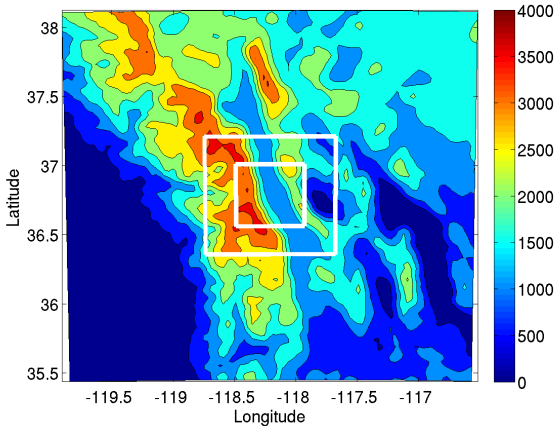


(a)

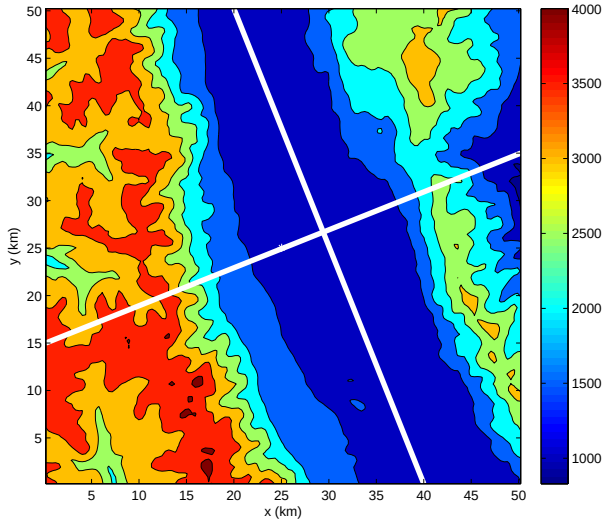


(b)

Figure 2.2. Color contours are terrain height in meters ASL. (a) 3 km resolution with boxes showing extent of 1 km and 350 m nests. (b) 350 m resolution with white lines showing across and along valley vertical cross-section locations.

does not resolve the valley topography). Soil moisture is set to zero on all grid levels for the DRY case, and set to fully saturated for each soil type for the WET case. Soil types are from STATSGO (1 km). Setting soil moisture to fully saturated means that all the open pore space is filled with water for each soil type. Since each soil type has a different porosity (percentage of open pore space), the amount of water in the soil will be different for each soil type. This means that soil moisture is homogeneous for the DRY case, and heterogeneous according to soil type for the WET case (see Figure 2.3). These are the two extremes for soil moisture in Owens Valley, the cases which should bracket what we observe in reality. All analysis presented herein has been performed on the 350 m grid.

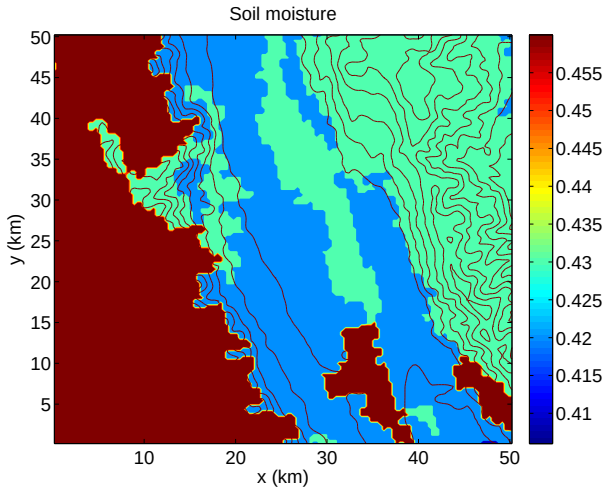


Figure 2.3. Initial soil moisture ($m^3/m^3$) on the 350 m grid for WET. Initial soil moisture for DRY is zero everywhere (not shown). Contours are terrain.

### 2.3.3 Simulation periods

Two observation periods during T-REX were selected for simulation with ARPS. The first is our weak forcing case and corresponds to Enhanced Observational Period 2 (EOP2) which exhibited relatively quiescent conditions under which thermally-forced flows could be observed. EOP2 began at 1500 Pacific Standard Time (PST) on March 29, 2006 and ended at 1500 PST the following day. Cross- and along-valley slices in Figures 2.4(a) and 2.4(b) from the ARPS model simulations show thermally-induced up-slope and up-valley circulations during EOP2. The second observation period is our strong forcing case and corresponds to Intensive Observational Period 6 or (IOP6) during which observed crest level winds increased to over 30 m/s so that rotor flow and mountain waves were observed. IOP6 began at 0900 PST on March 24, 2006 and ended at 2100 PST the following day. Cross- and along-valley slices in Figures 2.4(c) and 2.4(d) show an example of the flow structure during IOP6. It should be noted that there were some dynamically-forced flows observed during portions of EOP2, though these were much weaker and smaller in comparison to those of IOP6. Maximum vertical velocities from the simulations of EOP2 were between approximately positive and negative 3 m/s, and 10 m/s for IOP6. Maximum horizontal velocities occurred above 8 km asl and were approximately 35 m/s for EOP2 and 45 m/s for IOP6. Henceforth, EOP2 will be referred to as the "weak" case and IOP6 the "strong" case. Because the observation periods

were different lengths (about one day for the weak case and a day and a half for the strong case), we will be comparing plots that span different lengths of time.

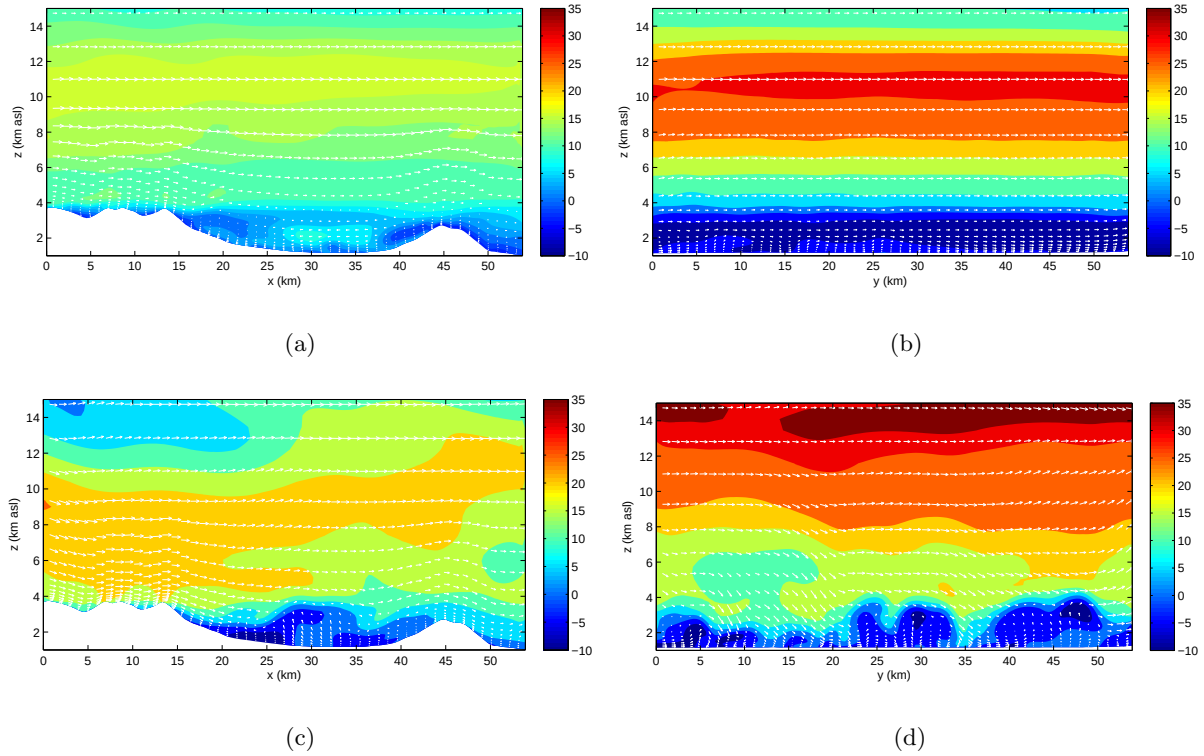


Figure 2.4. Weak case: (a) Across and (b) along valley slices for noon on March 30, 2006 (DRY). Strong case: (c) across and (d) along valley slices for noon on March 26, 2006 (DRY). Velocity into and out of the page shown as color contours (m/s), arrows are velocity vectors.

## 2.4 Comparative boundary layer evolution

In this section we compare the results from four simulations, using WET and DRY soil moisture conditions for both the weak and the strong cases.

### 2.4.1 Surface flux comparison

Since soil moisture affects flow in the ABL through the surface fluxes, first we compare the surface sensible heat fluxes at noon between cases as shown in Figure 2.5. For both the weak case and the strong case, the WET initialization results in less heating and in some areas cooling where the DRY case results in more heating (e.g. within the valley, 300 W/m$^2$ or more for DRY vs. 200 W/m$^2$ or less for WET). This indicates that soil moisture significantly affects surface heating throughout the domain in both cases.

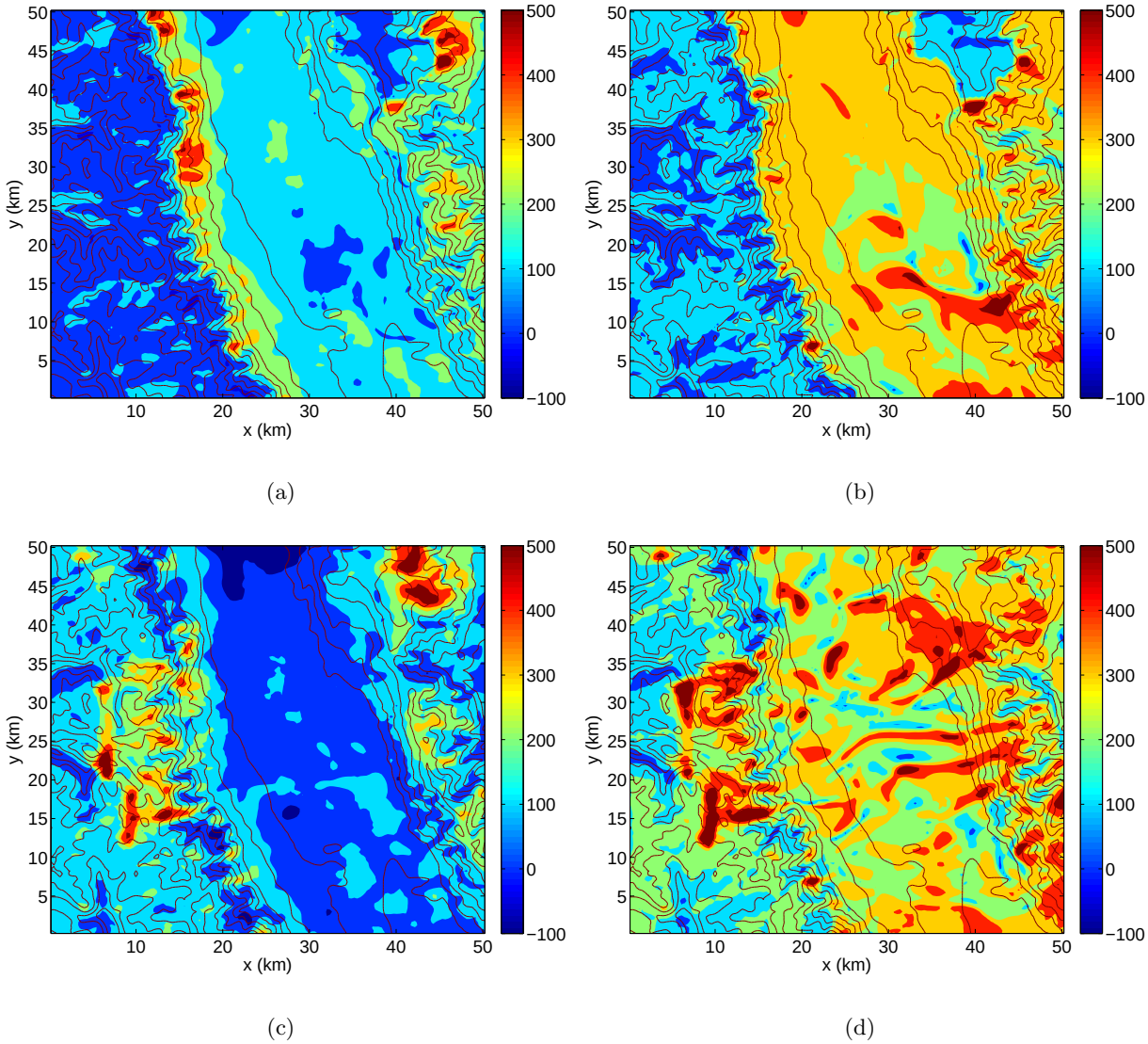


Figure 2.5. Surface sensible heat flux ($W/m^2$) on 350 m grid for (a) weak WET, (b) weak DRY, (c) strong WET, and (d) strong DRY. Contours are terrain.

Figures 2.4.1 and 2.6 show time series at the valley center of net solar radiation at the ground, sensible heat flux and latent heat flux for the WET initialization and the DRY initialization for the weak and strong cases respectively. Comparisons at other point locations were made (not shown) with similar conclusions. Net radiation is lower for the DRY case than the WET case because the albedo of dry soil is higher than that of wet soil and therefore more radiation is reflected for the DRY initialization than the WET initialization. Latent heat flux for the DRY case is essentially zero over the course of both the weak and strong simulations because there is virtually no water available for evaporation. For the DRY case therefore, virtually all energy at the surface goes into the sensible heat flux. For the WET intialization, in contrast, the latent heat flux is actually larger than the sensible heat flux throughout both the weak and strong forcing simulations. Thus, surface flux time series are similarly affected by soil moisture initialization under both weak and strong forcing.

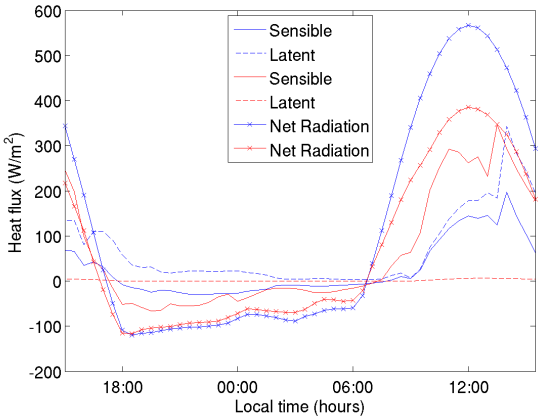


(a)

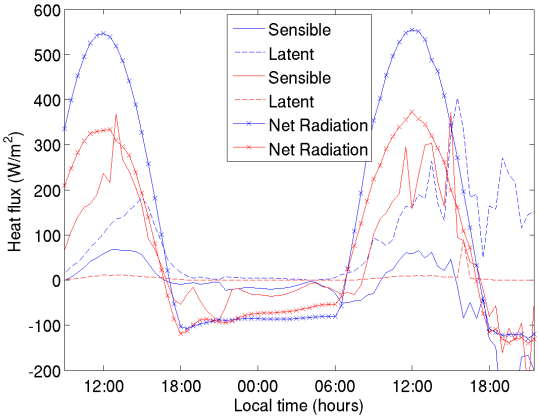


(b)

Figure 2.6. Surface flux series comparison for (a) strong and (b) weak cases.

### 2.4.2 Flow structure

The effects of initial surface soil moisture lead to major changes in the dynamics of the simulations. These differences in flow dynamics are most striking for the strong case, as shown in Figure 2.7, where vortices shed off the Sierra crest for the DRY, but not for WET at that time. Vortices do shed off the Sierra crest in the WET simulations, but this happens several hours earlier than in the dry case and vortices are much smaller (about half the size of those in the DRY simulations). Differences in flow dynamics manifest in the weak case as well, as shown in Figures 2.8 and 2.9 where DRY is warmer at 20:00 than the WET so that downslope flows on the eastern side of Owens Valley allow cool air to pour over the Inyo crest into the valley, producing more cooling of the valley volume by 22:00 in DRY than in WET. To understand the sources of differences in flow dynamics between the WET and DRY initializations, we perform a heat budget analysis.

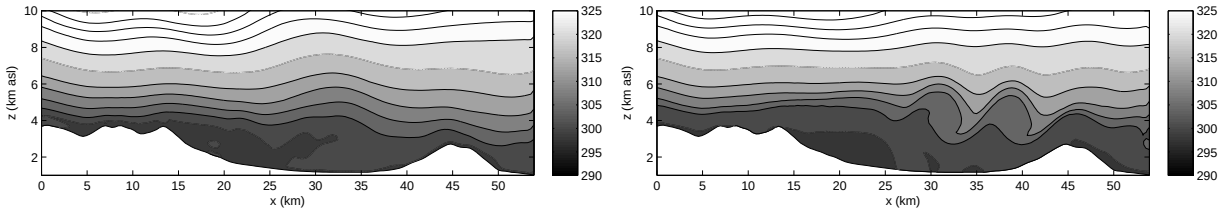


(a) (b)

Figure 2.7. Potential temperature contours with velocity vectors overlaid for strong case in the evening of March 26, 2006 (17:00 PST). Vortices shed off the Sierra crest in DRY, but not in WET. (a) WET (b) DRY.

### 2.4.3 Heat budget

In ARPS, the heat transport equation is written in terms of potential temperature $\theta$, so that each component of the equation contributes to the total heating rate, $\frac{\partial \theta}{\partial t}$ as shown in Equation 2.1.

$$\frac{\partial \theta}{\partial t} = -u\frac{\partial \theta}{\partial x} - v\frac{\partial \theta}{\partial y} - w\frac{\partial \theta}{\partial z} - M - R \tag{2.1}$$

Here the advection terms are the first three terms on the right-hand side, $M$ represents sub-filter scale turbulent mixing, and $R$ is the radiation component. Horizontal wind components $u$ and $v$ have been rotated from the original $x$ and $y$ directions on the ARPS grid, so that they are now directed across and along the valley axis, respectively, as shown in Figure 2.3.1. The $w$ velocity component, is directed in the vertical direction.

#### Surface heating by radiation

We will first consider the time evolution of just the radation component, $R$ in a horizontally averaged plane 7 km by 7 km wide, at the center of the domain, at the level of the first grid point above the surface. This horizontal extent was chosen because it fits between the valley side

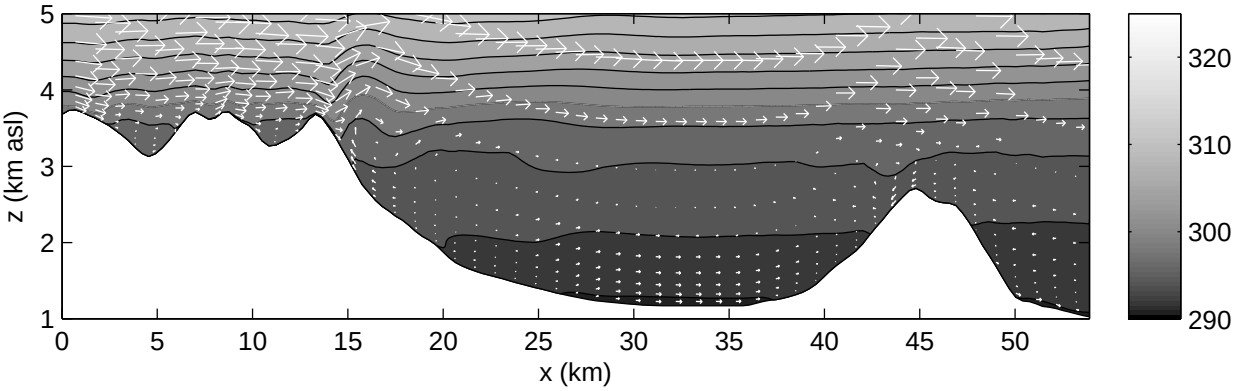


(a)

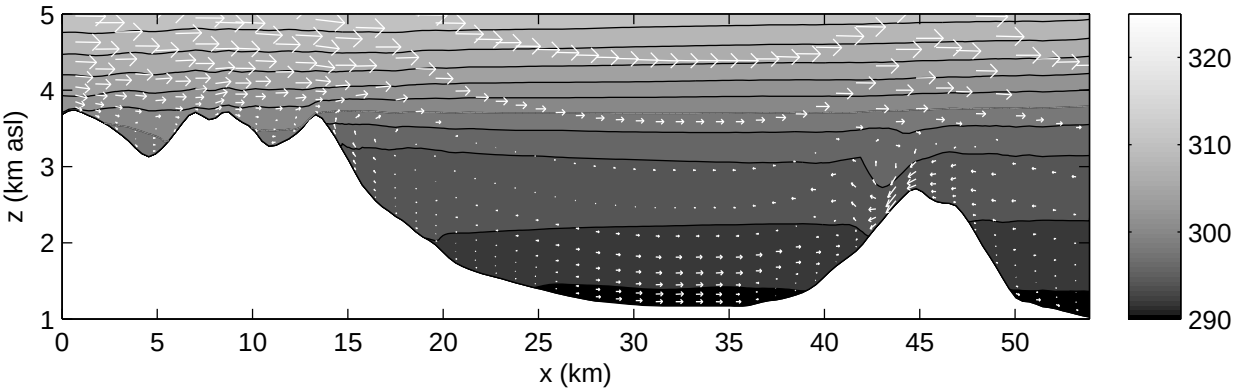


(b)

Figure 2.8. WET: Potential temperature contours with velocity vectors overlaid for weak case in the evening of March 29, 2006. Cool air pours over the Inyos from the east, into Owens Valley at (a) 20:00 PST, and (b) 22:00 PST. Figure 2.9 shows the same times for the DRY case.

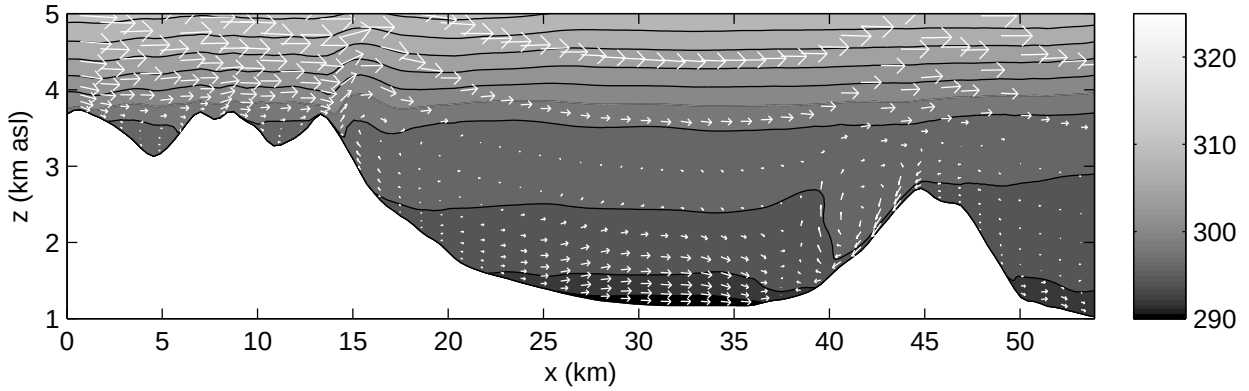


(a)

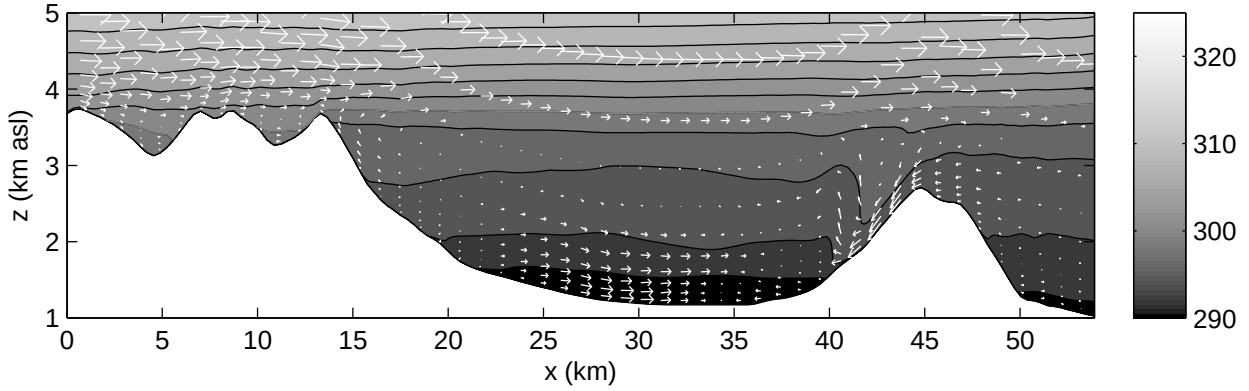


(b)

Figure 2.9. DRY: Potential temperature contours with velocity vectors overlaid for weak case in the evening of March 29, 2006. Cool air pours over the Inyos from the east, into Owens Valley at (a) 20:00 PST, and (b) 22:00 PST. Note that the cold "pool" that forms at the center of the valley is deeper by 22:00 in the DRY initialization (this figure) than the WET initialization (previous figure).

walls, over the valley floor. Figure 2.10(a) shows near surface heating due to radiation. Positive values indicate heating, negative values indicate cooling. The DRY initialization shows amplified heating and cooling compared to the WET initialization. This amplification occurs because more energy is available for heating the air in the DRY simulation whereas in the WET simulation a significant portion of the available energy is being used to evaporate water. Also cooling appears more intense in the DRY simulation because in the WET simulation, energy is released as water condenses at night, which means that the air stays warmer (experiences less cooling) than in the DRY simulation. Note that in Figures 2.4.1 and 2.6, net radiation heating the land surface was greater for the WET initialization than the DRY, due to a change in the albedo of the soil, (dry soil is more reflective than wet soil). At the same time, the land-surface is heated more and therefore the air near the surface is heated more in DRY than in WET, as seen in Figure 2.10. Also visible in Figure 2.10(a) is a lag in the morning and evening transitions. The DRY simulation begins to heat later than the WET simulation at sunrise and sunset. Similar observations can be made from Figure 2.10(b), where there are shifts in the transitions, though there is no clear pattern for the strong case as there is for the weak case.

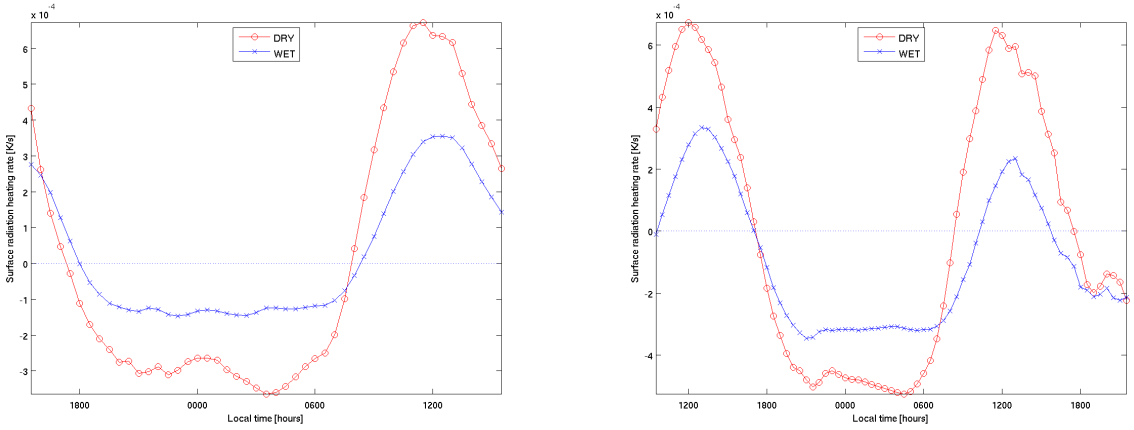


(a) (b)

Figure 2.10. Time series of heating of air near the surface due to radiation (K/s). (a) weak (b) strong

### Valley volume heating

We consider heating and cooling of the entire valley volume defined as all the cells within the valley which are located below 2.4 km. This threshold level was chosen because it is just below the lowest ridge crest (in the Inyo Mountains) surrounding the valley, thus insuring that air can only enter the valley volume from the north, south, or from above. Potential temperature, specific humidity, as well as components of the heat budget were extracted from the simulations and averaged over the valley volume. The valley volume heat budget shows the contribution of each component to overall heating (or cooling) of the air within the valley.

Valley volume averaged plots of specific humidity (not shown) show that the valley volume

for WET has higher humidity than DRY over the course of both the weak in strong simulations. Figures 2.11(a) and 2.11(b) show valley volume averaged potential temperature for the weak and strong cases respectively. Immediately recognizable is the correlation between Figure 2.11 and Figure 2.10, showing that the diurnal cycle of heating by radiation at the surface translates almost directly to heating of the entire valley volume. There is a lag in heating of the entire valley volume (the peaks of Figure 2.11 are shifted compared to those of Figure 2.11) which is probably attributable to the time it takes for heat to be transferred and mixed up from the surface and throughout the valley. In general the valley volume heats during the day and cools at night, except in the evening on the second day of the strong case when there is some significant heating by advection which acts counter to the surface cooling taking place at that time. To illustrate which components are most affected by surface forcing, the following section discusses the components of the valley volume heat budget and how these contribute to overall heating and cooling of the air within the valley.

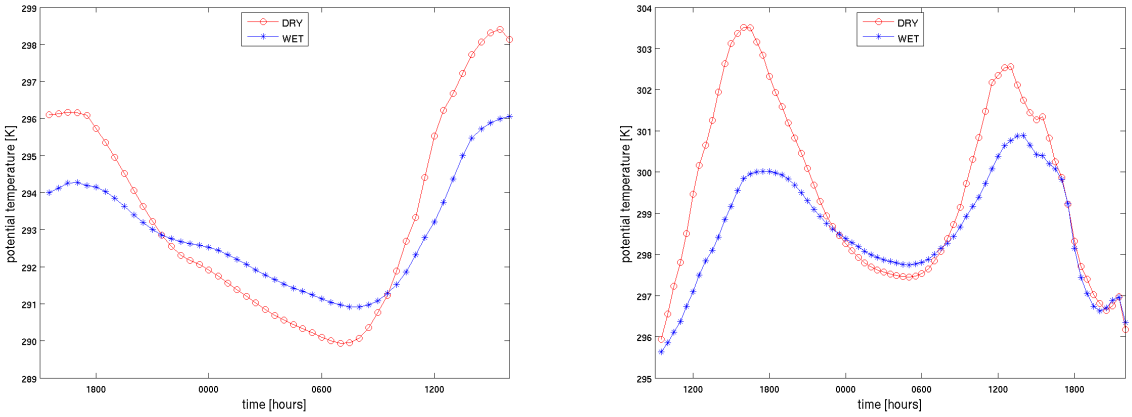


(a) (b)

Figure 2.11. Time series of valley volume averaged potential temperature (K). (a) weak (b) strong

Figures 2.12 and 2.13 show the valley volume heat budget for the weak and strong cases respectively. The subgrid-scale mixing term follows the radiation term during daylight hours, growing larger (contributing more heating) as surface heating increases to a peak around midday and then decreasing and having a cooling effect after the evening transition. In contrast, the advection term contributes a small amount to heating overnight, then contributes a significant amount of cooling during daylight hours. The advection and mixing terms mirror each other somewhat, due to similarities in their numerical representation. Total heating is the sum of all three components and in general shows heating of the valley volume during the day and cooling at night.

Immediately recognizable when comparing the DRY initialization to the WET initialization is the difference in amplitude between the two. Also of note for the weak case is the difference in the total advection term at night, which shows slight heating in the early morning hours (from about 0300 to 0800) for the DRY simulation and cooling in the WET simulation (see Figure 2.12). The strong case shows significant differences in the advection term as well. Of note is the change in sign of the advection term of the WET initialization, from negative (cooling) to positive (heating) and back again in the afternoon (between 1300 and 1800) of the second day of simulation (see Figure

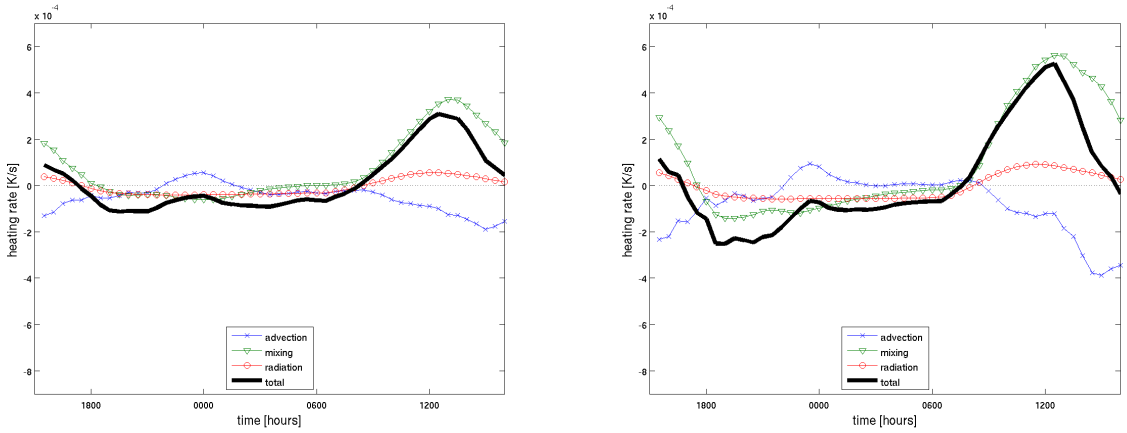


(a) (b)

Figure 2.12. Average valley volume heat budget for weak case (a) WET, (b) DRY.

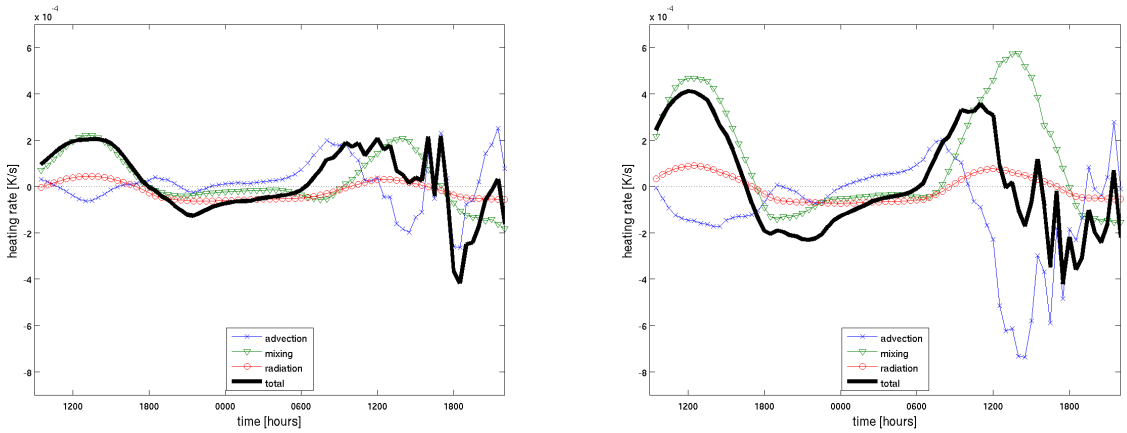


(a) (b)

Figure 2.13. Average valley volume heat budget for strong case (a) WET, (b) DRY.

2.13). Such a feature does not appear in the DRY initialization simulation; rather, the advection term remains negative through that period.

To further analyze the contribution from the advection term, the individual components (x,y,z) of the advection term are shown in Figures 2.14 and 2.15 for the weak and strong cases respectively.

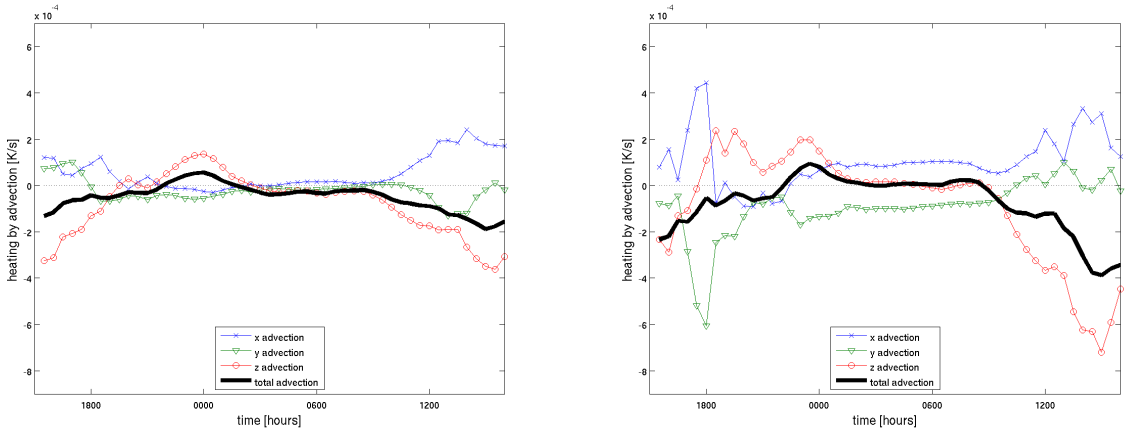


(a) (b)

Figure 2.14. Average valley volume budget for advection of heat, weak case (a) WET, (b) DRY.

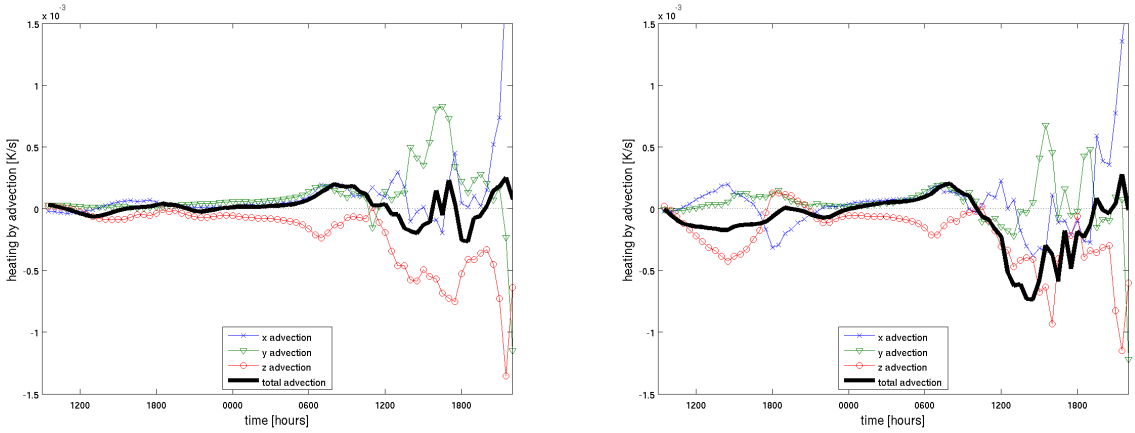


(a) (b)

Figure 2.15. Average valley volume budget for advection of heat, strong case (a) WET, (b) DRY.

Heating by advection in the horizontal x-direction (cross-valley) during the day for the weak case is due to dynamically-driven flow, though this effect is significantly weaker than during the strong case. Cooling by advection in the vertical (z-direction) is due to a positive (upward) valley volume averaged, or net vertical velocity, while warming is due to a negative (downward) net vertical velocity (subsidence warming). This can been seen in Figure 2.16(a) as well as in the cross-section wind components shown in Figures 2.4(a) and 2.4(b).

In general, stable stratification leads to cooling with a positive (upward) net vertical velocity and

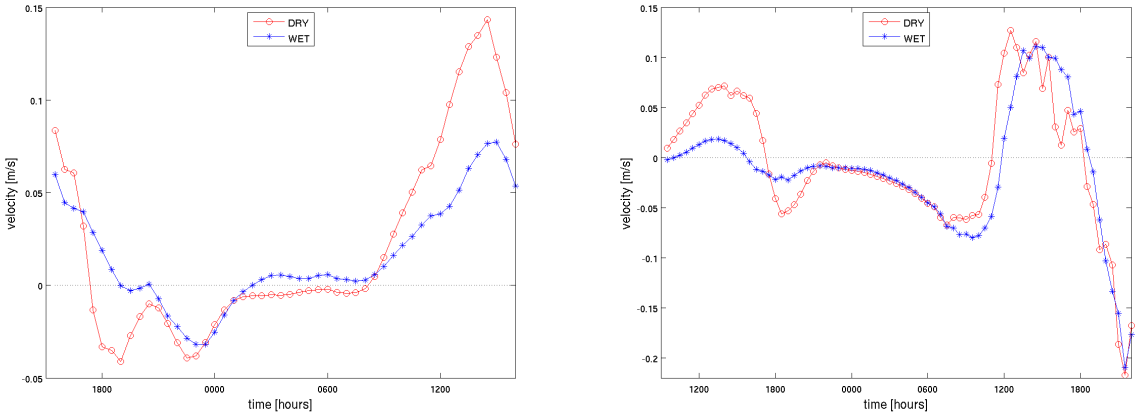


(a) (b)

Figure 2.16. Average valley volume vertical velocity, $w$ (a) weak (b) strong.

heat if there is a negative (downward) net vertical velocity. With unstable stratification however, under mountain wave breaking or rotor conditions, for example, it is less clear whether there will be net heating or cooling according to the net vertical velocity. For the strong case, it is possible that overturning of isotherms around 2.4 km (the lid of our valley volume) permits a net negative (downward) vertical velocity (see Figure 2.16(b)) to produce a cooling effect overnight in both the WET and DRY cases. Overturning contours are shown in Figure 2.17. During the day, however, a net positive vertical velocity leads to cooling by vertical advection, while a net negative vertical velocity leads to heating by advection, as was observed in the weak case. This is true under both the relatively stable conditions on the first day of the strong case as well as the second day when there is vigorous mixing and turbulent flow within the valley.

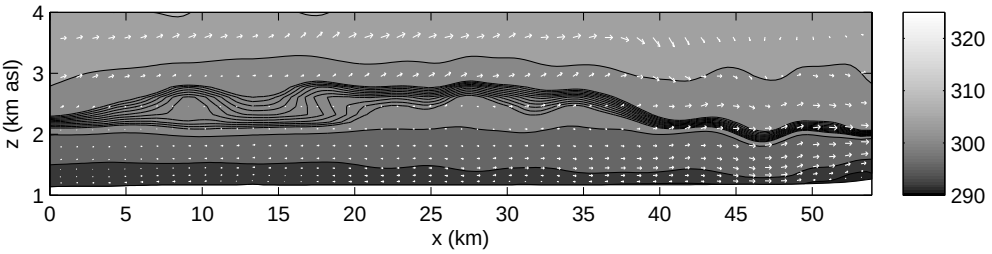


Figure 2.17. Shaded contours are potential temperature (K) in along valley cross-section for WET, strong case (0700 March 26, 2006). Fine contours are at 0.1 K from 300.6 to 301.6 K. Vertical axis is shown with factor of 4 stretching compared to horizontal. Plot for DRY is very similar (not shown).

**Profile comparisons**

Having established that soil moisture affects the partitioning of energy surface sensible and latent heat fluxes in Owens Valley, and that heating (and cooling) of the valley volume is in turn affected by changes in the surface fluxes, we now consider how soil moisture intialization affects air above the ridge tops. Vertical soundings of the heat budget components are extracted by horizontally averaging profiles over a 7 km by 7 km square in x and y. To make a more direct comparison between the weak case and the strong case for the WET and DRY initializations, the absolute difference in total heating rate between WET and DRY is calculated, then averaged over the duration of each simulation (see Figure 2.18(a).) The large bulge in the profile representing the difference between WET and DRY for the strong case is probably due to shear instabilities associated with having high wind speeds over the mountain crests (around 4 km ASL). Large differences in wave phase and amplitude between the WET and DRY initializations manifest as large differences in total heating rate. A smaller bulge in the profile representing the weak case also appears in a region of persistently unstable air around 8 km. Noteworthy on this plot are the significantly larger absolute differences in total heating rate for the strong case versus the weak case. This is in direct contradiction to the "rule of thumb" regarding the lesser importantance of soil moisture under strong forcing. In the complex terrain of Owens Valley, the observation period with high winds is actually more sensitive to soil moisture initialization than the observation period with relatively quiescent conditions.

The same analysis has been performed for sub-filter scale turbulent kinetic energy (TKE) and is shown in Figure 2.18(b). A similar conclusion can be drawn from this figure, where the largest differences between WET and DRY initializations are again seen in the strong forcing case up to about 5 km (about 1 km above ridge crest height). For the weak forcing case, an unstable layer between 7 and 10 km manifests in a bump in TKE differences at that height (at the same level as the bump in total heating rate differences). Otherwise, TKE is zero in the upper atmosphere and increases to a maximum near the land surface. The maximum difference in TKE for the weak case is only about half the maximum difference for the strong case.

Similarly for potential temperature and specific humidity, as shown in Figures 2.18(c) and 2.18(d), we see that the largest absolute differences in both variables occur at the surface. The average absolute differences in potential temperature are generally larger for the strong case than for the weak case, though this difference is relatively small (0.25 K) in the upper atmosphere, compared to below ridge crest height. Differences in specific humidity are larger in the strong case than the weak case at the surface and above ridge crest height.

For the weak case, effects of soil moisture appear to be greatest within the valley, below ridge crest height (4 km), while for the strong case, these effects are not confined within the valley walls, but rather extend two or more kilometers above ridge crest height (6 to 8 km) due to the strong vertical velocities associated with mountain waves and rotor flow.

### 2.4.4 Alternative initialization procedure

To test the sensitivity of the soil moisture initialization on different grid levels, a set of additional simulations was performed where interpolated NAM soil mositure was used to initialize the 3 km grid and soil moisture was set to DRY conditions on only the 1 km and 350 m grids, (instead of all three grid levels, as was done previously). We will refer to this case as DRY_1km. Results of

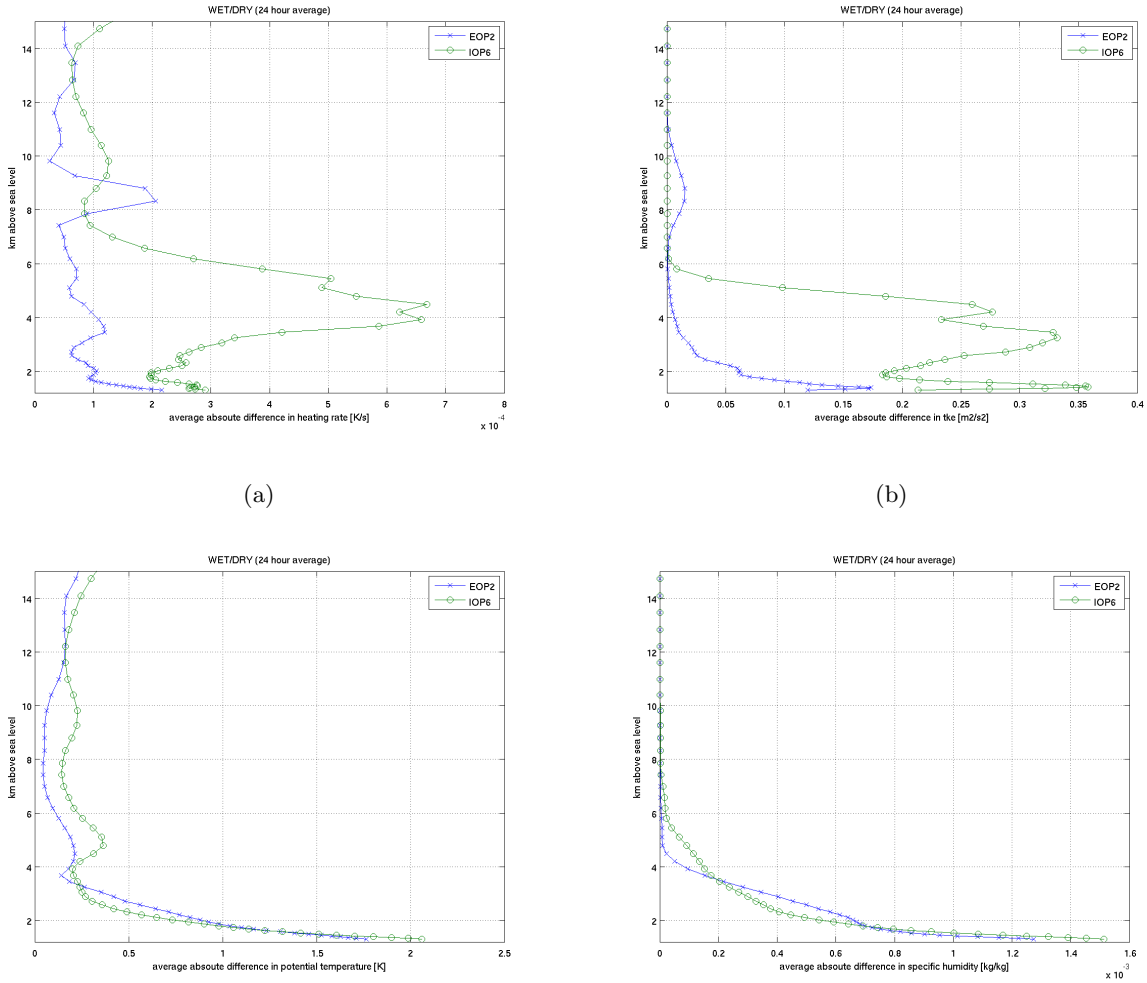


(a) (b)

(c) (d)

Figure 2.18. 24 hour average absolute difference between WET and DRY for weak (x) and strong (o) for (a) heating rate (K/s), (b) turbulent kinetic energy ($m^2/s^2$), (c) potential tempertaure (K), (d) specific humidity (kg/kg).

these simulations indicate that the 3 km grid soil moisture affects the finer grids to some extent through the advection and mixing terms of the heat budget. There is some additional cooling in the DRY_1km case due to advection, which causes a slightly lower peak heating rate during the day for both the quiescent and strong forcing cases. Still, the overall diurnal cycle of heating and cooling is very nearly the same between the DRY_1km (soil moisture set to zero only on the 1 km and 350 m grids) case and the DRY case (soil moisture set to zero on all grid levels).

The results of these simulations seem to indicate that local surface soil moisture dominates effects on flow so that surface conditions on the outer nest or nests may not be as important as those on the finer grids.

## 2.5 Conclusions and future work

We have shown that changing the soil moisture initialization for simulations of atmospheric flow over complex terrain can greatly influence the flow dynamics under both weak and strong synoptic forcing. We hypothesize that this is a result of thermally-induced circulations under weak synoptic forcing, and dynamically-induced circulations modified by thermal effects under strong synoptic forcing. Surface fluxes are shown to be similarly affected in space and time by fully saturated versus dry initial soil moisture under both weak and strong synoptic forcing. Heat budgets representing the valley volume as well as horizontally-averaged vertical profiles show that heating of the atmosphere is similarly affected by soil moisture initialization under weak and strong forcing. Given these results, it may be important to give special consideration to surface boundary conditions, and soil moisture in particular, when performing numerical simulations of atmospheric boundary layer flow over complex terrain under both weak and strong synoptic forcing.

# Chapter 3

# Coupled hydrologic modeling of the subsurface-land-atmosphere system

## 3.1 Introduction

This chapter focuses on coupled hydrologic modeling to predict surface soil moisture fields for initialization of simulations of atmospheric boundary layer flow. Results from simulations discussed here are validated using field measurements presented in Chapter 5 and used to initialize atmospheric simulations in Chapter 6 of this dissertation.

## 3.2 Background

The land surface is the interface between earth and atmosphere, where topography, vegetation, and soil interact with water and air. Sensible and latent heat fluxes at the land surface provide a bottom boundary condition to the atmosphere and thereby affect flow in the atmospheric boundary layer, while evaporation, transpiration, precipitation, infiltration, and run-off form an upper boundary condition for groundwater flows. An understanding of this complex system of interactions is integral to studying the hydrologic cycle. Furthermore, as climate change begins to affect previously observed balances in this cycle, calibrated models may no longer apply, and physically-based models will become invaluable in hydrologic prediction.

Though conditions at the land surface can determine the nature of flow in the atmospheric boundary layer, most atmospheric models use land-surface models referred to as leaky-bucket models. Such models do not account for lateral flow at the surface, let alone the subsurface. Thus neighboring cells are isolated from one another, and though run-off may be calculated for each cell, it is not passed to neighboring cells during subsequent time steps. The problem with this approach is that neglecting to properly close the mass balance of water at the land surface can

lead to inaccurate prediction of quantities such as soil moisture, which affects sensible and latent heat fluxes. Water table depth, which is usually neglected (or rarely parameterized in land-surface models), can also strongly affect soil moisture at the land-surface.

Soil moisture can change significantly over the course of a day due to precipitation events and evapotranspiration, and can vary over longer timescales with changes in vegetation growth or groundwater flow. Soil type and local topography can make soil moisture change over varying length scales as well. This kind of small-scale variability is difficult to capture in soil moisture datasets provided by continental- or global-scale models. Even higher resolution models may not accurately capture soil moisture variability because typical land-surface models do not allow for lateral transport of moisture, and hence cannot represent spatial variability due to topography. Finally, field measurements of soil moisture are typically too sparse to provide a complete representation of the soil moisture field in a given region. For these reasons, accurate, high resolution soil moisture data is not often available to initialize mesoscale atmospheric simulations. Coupled hydrologic modeling is one approach which includes both surface and subsurface lateral flows as well as land-surface processes, so that more accurate surface conditions such as soil moisture can be provided to an atmospheric model.

The focus of this chapter is to use a coupled hydrologic model to determine a more accurate representation of the soil moisture distribution in a region of complex topography, Owens Valley in California. To the author's knowledge, coupled hydrologic modeling in terrain as complex as that of Owens Valley has not previously been undertaken. Results from the land-surface groundwater model are compared to observations from the Terrain-Induced Rotor Experiment which took place in Owens Valley in March and April, 2006. In Chapter 6, results from this coupled model will be used to initialize soil moisture for high-resolution simulations of atmospheric flow over the region.

### 3.2.1 Motivation

High-resolution surface boundary conditions for mesoscale atmospheric models are usually interpolated from coarser grids. In regions of heterogeneous surface conditions this interpolation procedure can lead to misrepresentation of the surface characteristics. For example, even a large valley such as Owens Valley in California, approximately 12 km in width, is not properly resolved at coarse resolutions such as the 12 km grid used in the North American Mesoscale Model (NAM), or the 32 km grid used in the North American Regional Reanalysis (NARR). Since the valley is surrounded by high mountains, both the 12 km NAM and 32 km NARR grids represent a portion of the valley region as one wide mountain, including snow at the summit. When the snow field is interpolated down to grids fine enough to resolve the valley (e.g. at least 3 km horizontal resolution), we find at least part of the valley floor to be (unrealistically) covered in snow. Figures 3.1(b) and 3.1(d) show examples of this problem, which translates into elevated soil moisture values shown in Figures 3.1(a) and 3.1(c). Interpolated surface boundary conditions are especially problematic for surface variables that can change drastically in a short period of time, such as soil moisture, soil temperature, and snow cover.

Current land-surface models such as the ISBA model (Interactions Soil Biosphere Atmosphere), coupled to meso-scale atmospheric models like the Advanced Regional Prediction System (ARPS) used in Chapters 2 and 6, are often only two-layer models. Multi-layer models exist [e.g. the unified Noah land surface model used in WRF *Chen et al.*, 2004; *Tewari et al.*, 2004; *Liu et al.*, 2004], but no current soil model allows for lateral transport of soil moisture. Thus rain accumulated on

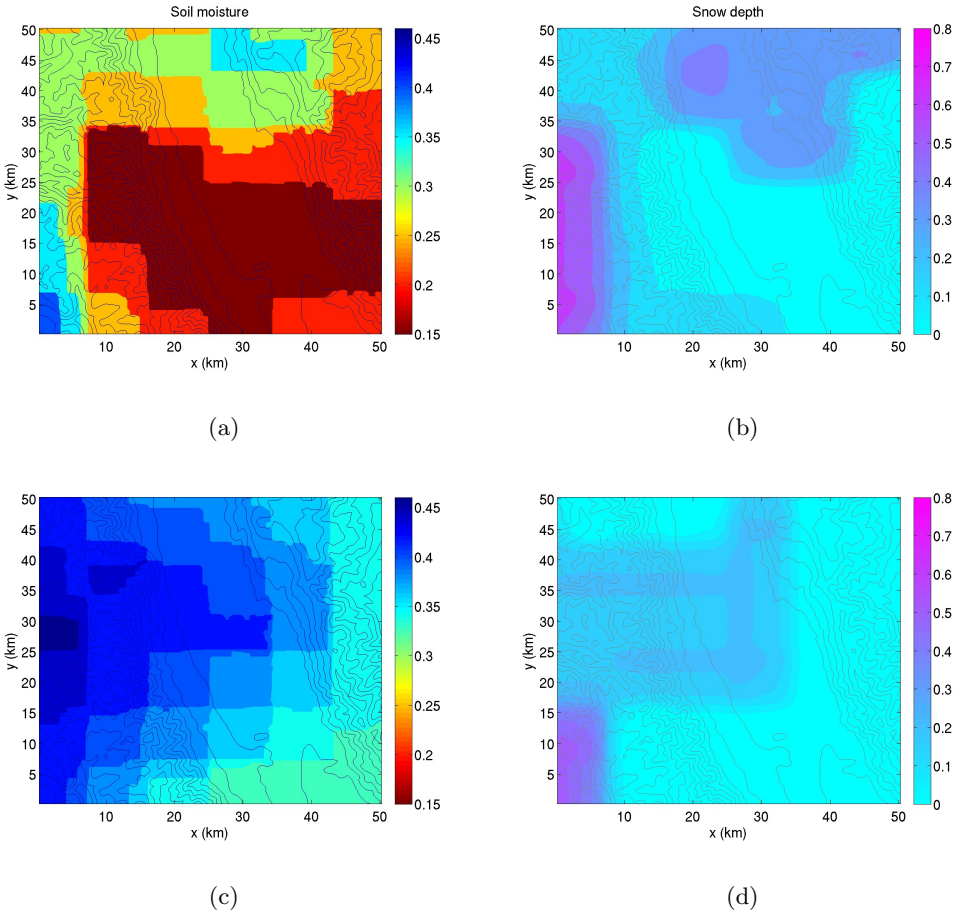


Figure 3.1. Interpolated soil moisture ($m^3/m^3$) and snow depth (m) from NAM (12 km, top row) and NARR (32 km, bottom row). Contours are terrain height (m) for a section of Owens Valley at 350 m resolution centered at Independence, California.

the steep Sierra slopes will not flow to the valley floor because each grid cell is isolated from its neighbors.

One way to achieve more accurate surface conditions is to run a separate hydrologic model and use the results to initialize the atmospheric model. Previous work in the Riviera Valley in the Swiss Alps showed that soil moisture initialization was a very sensitive parameter for correct prediction of valley wind transitions [*Chow et al.*, 2006b]. Running a hydrologic model (WaSiM-ETH) to provide initial soil moisture conditions reduced the 3-4 hour delay in the onset of up-valley winds in the Riviera to just 1-2 hours. Improvement of surface initialization can be achieved through the use of hydrologic models; however, many hydrologic models are incapable of simulating lateral flow of water from one cell to the next. Depending on how the model is set up, this can result in a pile-up of water in certain cells, or a net loss of water from the model.

Groundwater models can simulate lateral flow of water in the subsurface. In particular, the watershed model ParFlow [*Ashby and Falgout*, 1996; *Jones and Woodward*, 2001; *Kollet and Maxwell*, 2006] includes fully integrated surface and subsurface lateral flow. *Maxwell et al.* [2007] coupled ParFlow to ARPS, providing updated high-resolution soil moisture to the ARPS land-surface model at every time step. An off-line spin-up of ParFlow was used to generate a realistic initial soil moisture distribution in the domain. The fully coupled set-up was not necessary for this study because there was no precipitation during the time period chosen for the simulation. In previous work, *Maxwell and Miller* [2005] coupled a variably saturated groundwater model (ParFlow) to a land-surface model (Common Land Model, now the Community Land Model supported by the National Center for Atmospheric Research). Their results showed that including an explicit representation of the water table was important in accurately determining the shallow soil moisture distribution. A slightly different coupling approach was taken by *Kollet and Maxwell* [2008], though the coupling still takes place through soil moisture, evapotranspiration and infiltration from precipitation.

### 3.2.2 Objectives

The coupled land-surface groundwater model of *Kollet and Maxwell* [2008] is used in the current study and will be referred to henceforth as PF.CLM. PF.CLM takes advantage of the more sophisticated land-surface processes calculated by CLM (such as snow processes). It is a physically-based model that does not require long historical records of precipitation data for calibration to the specific catchment, as many hydrologic models do. The objective here is to describe the spin-up procedure used to determine the initial soil moisture distribution in Owens Valley and show comparisons to observations from T-REX. Results of the atmospheric simulations using the initial soil moisture fields determined here will be presented in Chapter 6.

## 3.3 Owens Valley and T-REX

Owens Valley is a rift valley in southeastern California located between the eastern slopes of the Sierra Nevada mountain range and the western slopes of the White and Inyo Mountains. The peaks of the Sierras reach above 4,300 m (14,000 ft) while the valley floor lies at about 1,200 m (4,000 ft), making it one of the deepest valleys in the United States. The valley is approximately 120 km in length (∼75 mi) and runs approximately north-south. Dominant vegetation types on

the valley floor include shrubs and grasses [*Steinwand et al.*, 2006]. Soils range from coarse sand and gravel to fine sand, clay and silt [*Danskin*, 1998].

The Terrain-Induced Rotor Experiment (T-REX) took place in March and April, 2006. The main goal of the T-REX field campaign was to investigate the dynamics of atmospheric rotors and lee waves in Owens Valley, with broader goals including complex terrain boundary layer development and stratospheric-tropospheric exchange. Additional scientific objectives include using the extensive T-REX datasets to validate numerical models. A more detailed description of T-REX can be found in the Introduction of this dissertation.

As part of the T-REX field campaign, soil moisture and temperature mesurements were taken at 23 sites around Owens Valley. These are shown in Fig. 3.2. A more complete description of how these measurements were made can be found in Chapter 5 as well as *Daniels et al.* [2006]. The soil moisture measurements collected at these sites will be used for comparisons to the soil moisture results generated by the off-line spin-up of the coupled land-surface groundwater model, PF.CLM.

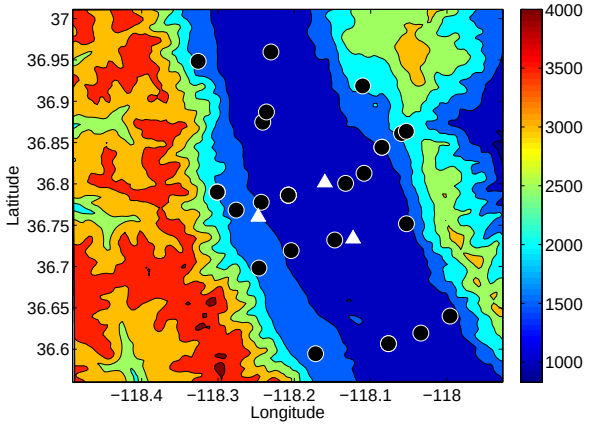


Figure 3.2. Elevation contours (m) of Owens Valley centered around Independence, CA from the 350 m resolution simulation domain. Circles indicate locations of soil moisture measurement sites and triangles show the three ISFF flux towers. An additional soil sensor was placed north of Independence, near Bishop (not shown).

## 3.4 Coupled model setup

### 3.4.1 PF.CLM model overview

PF.CLM will be used to obtain a spun-up soil moisture field to initialize ARPS with a more realistic representation that includes topographic variations in soil moisture. PF.CLM is a groundwater model, ParFlow (PF), coupled to a land-surface model, the Common Land Model (CLM). CLM represents the land surface with a single vegetation canopy layer, up to 5 snow layers, and 10 unevenly spaced soil layers [*Kollet and Maxwell*, 2008; *Maxwell and Miller*, 2005; *Dai et al.*, 2003]. The version of ParFlow used for this research incorporates a two-dimensional overland flow simu-

lator into a parallel three-dimensional variably saturated subsurface flow code [*Ashby and Falgout*, 1996; *Kollet and Maxwell*, 2006]. The coupling occurs at the surface and in the first 10 layers of soil, where the domains of ParFlow and CLM overlap. All subsurface and surface flows are calculated by ParFlow and soil moisture values are provided to CLM. CLM in turn provides ParFlow with infiltration, evaporation, and root uptake fluxes [*Maxwell and Miller*, 2005].

The coupled PF.CLM model is three-dimensional and can be run efficiently in parallel. To take full advantage of the lateral flow capabilities of PF.CLM, the model should be run in 3D. First, a 2D version of PF.CLM is employed to obtain a simple representation of Owens Valley soil moisture before moving to three dimensions. A 3D set-up is described here along with the 2D set-up. The Owens Valley region has a varied climatology, such that the weather conditions in one part of the simulation domain are very different from those elsewhere in the domain. Thus, it may rain in the mountains, but remain dry on the valley floor, and it is likely that the temperature on the mountain tops is significantly cooler than that on the valley floor. Thus it is more realistic to provide the model with conditions that vary in space as well as time. The version of PF.CLM used in this investigation implements uniform meteorological forcing and had not yet been extended to distributed forcing. The ability to use distributed forcing, that is, meteorological conditions that vary in both space and time, was added to the PF.CLM framework for running on a single processor. This distributed forcing may be extended to accommodate three dimensions and parallel processing in future work. It was necessary to employ the parallel version of the code (which does not include distributed forcing) in order to complete a full spin-up in 2D as well as run the 3D simulations. A full year of meteorological forcing data is required including pressure, temperature, winds, humidity, radiation and precipitation and these variables are taken from the North American Regional Reanalysis (NARR). Results from three simulations are presented in this investigation. These are: a simple geology 2D simulation with distributed forcing, and complex geology 2D and 3D simulations with uniform forcing. The 2D simulation with complex geology is a cross-valley slice through the center of the 3D domain and uses the same uniform meteorological forcing.

### 3.4.2 Grid and subsurface initialization

The goal of the coupled hydrologic modeling performed here is to obtain a more accurate representation of surface soil moisture to be provided as a surface boundary condition to the mesoscale atmospheric model, ARPS (discussed in the Introduction, as well as Chapters 2 and 6. It follows that the horizontal extent of the 3D simulation was chosen to match that of the finest ARPS grid (350 m horizontal grid resolution). While it may have been desireable for many reasons to simulate the entire Owens Valley watershed, the complex terrain of the region would have made the domain too large, or the horizontal resolution too coarse for our purposes. For the 2D simulations, a slice of the valley was chosen corresponding to the general location of the main transect of soil moisture measurement sites from T-REX, which is roughly around 36.8 degrees latitude (see Fig. 3.2) and passes through the town of Independence. Thus the PF.CLM Cartesian grid for the 3D simulation has dx = dy = 350 m with nx = ny = 144 points, while the 2D simulations have just dx = 350 m and nx = 144 points. Vertical discretization is dz = 1 m, with a total of nz = 3250 points for both the 2D and 3D simulations. Finer vertical discretization is usually preferred, but dz is limited to 1 m here due to the large number of points required for inclusion of the mountain peaks. At this resolution, simulations must be run on many hundreds of processors.

ParFlow maintains a full Cartesian box grid, and relies on the assignment of "active" and

Table 3.1. Surface/subsurface geology simulation parameters.

| | Geology type | Porosity (-) | Permeability (m/hr) |
|---|---|---|---|
| Soil type (from ARPS): | | | |
| | sand | 0.417 | 0.003852 |
| | loamy sand | 0.421 | 0.05076 |
| | sandy loam | 0.434 | 0.018828 |
| | silt loam | 0.486 | 0.010116 |
| | loam/clay loam | 0.439 | 0.012168 |
| | silty clay/clay | 0.468 | 0.0035064 |
| Subsurface geology (based on *Danskin* [1998]): | | | |
| | low perm | 0.001 | 0.00001 |
| | medium perm | 0.01 | 0.0004167 |
| | high perm | 0.4 | 0.41667 |
| | very high perm | 0.5 | 1.04167 |

"inactive" cells to determine which parts of the Cartesian grid are in the simulation domain. For this study, only the cells in the first 500 m below the ground surface were part of the "active" domain as illustrated in Figure 3.3

As a rift valley, Owens Valley is formed by two main parallel faults running lengthwise along the valley axis and separating the alluvial fill of the valley floor from the bedrock of the mountains forming the valley walls. Two subsurface geology configurations are presented here. The first is a very simple representation with bedrock below the mountain peaks and soil below the valley floor (see Figure 3.3(a)). Constant porosity of 0.1, and hydraulic conductivity of 0.1 were used for the alluvial fill, and 0.0001 for both porosity and hydraulic conductivity of the rock beneath the peaks. The second configuration employs a more detailed representation of the subsurface geology, relying on USGS transects for geology types (see Figure 3.3(b)). The 2D indicator field for the complex geology set-up is a slice taken directly from the 3D indicator field (near latitude 36.8, aligned with the main soil moisture sensor transect). Several slices from the 3D indicator field are shown in Figure 3.4.

Corresponding values of subsurface porosity and hydraulic conductivity used here are based on those used by *Danskin* [1998]. Surface soil types, porosity and permeability values are the same as those used in ARPS. These are listed in Table 3.1.

For the 2D simulations, assigned y-slopes were used such that any grid point with a non-zero x-slope was given zero y-slope, while cells with zero x-slope were assigned a y-slope of 0.1 in the simple geology 2D simulations and 0.01 in the complex geology simulations. The assigning of y-slopes was necessary so as to allow water to flow down-slope along the 2D slice, then out of the domain in the river flood plain. Without assigning a non-zero y-slope in the flat area at the center of the valley, water would be unrealistically retained with the domain. The value of the y-slopes was changed because the simple geology simulations with slopes of 0.1 seem to have been draining too much water from the domain. For the 3D simulations, slopes were calculated from the DEM in x and y.

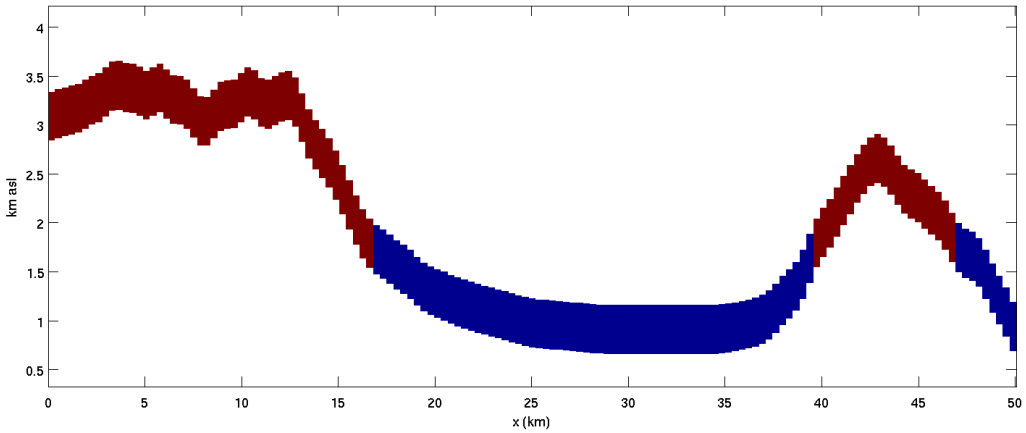


(a) aluvial fill (blue) and bedrock (red)

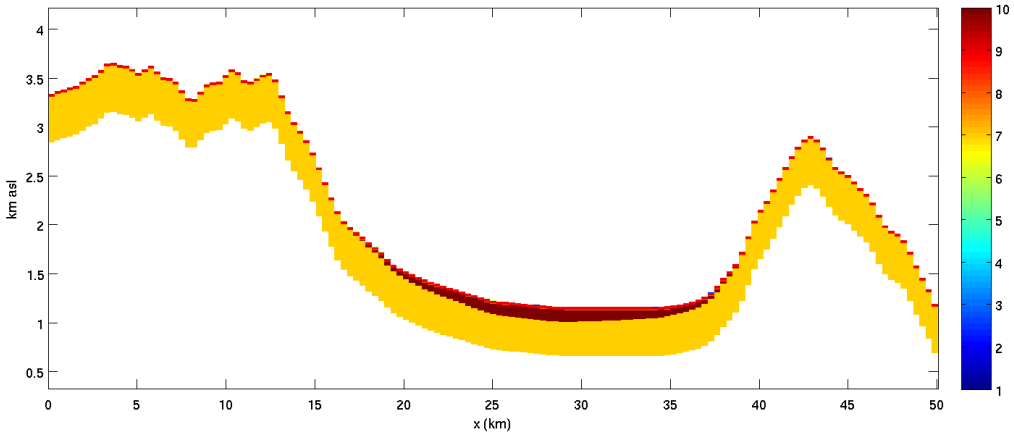


(b) Colorbar is surface soil types (1-6) and subsurface geology (7-10): 1) sand, 2)loamy sand, 3) sandy loam, 4) silt loam, 5) loam/clay loam, 6) silty clay/clay, 7) low permeability 8) medium permeability 9) high permeability 10) very high permeability (alluvial fill)

Figure 3.3. Cross-section of indicator fields representing subsurface geology in PF.CLM across Owens Valley near latitude 36.8 (center of the domain). Sierra Nevada mountains to the left, Inyo-White mountains to the right. (a) simple geology (b) layered subsurface geology and surface soil types from ARPS

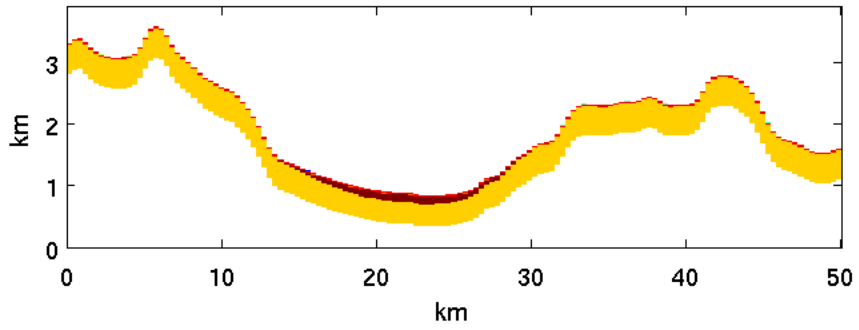


(a)

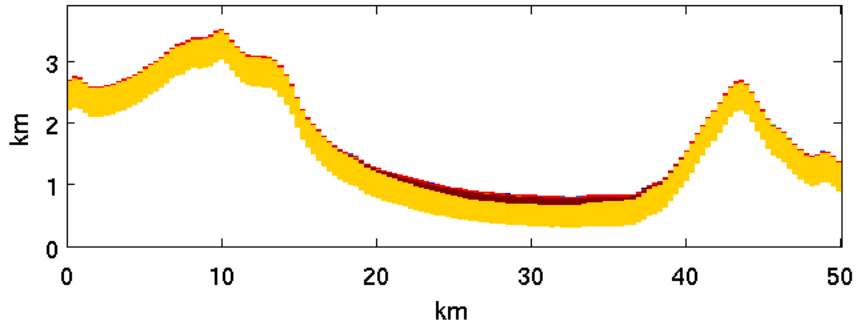


(b)

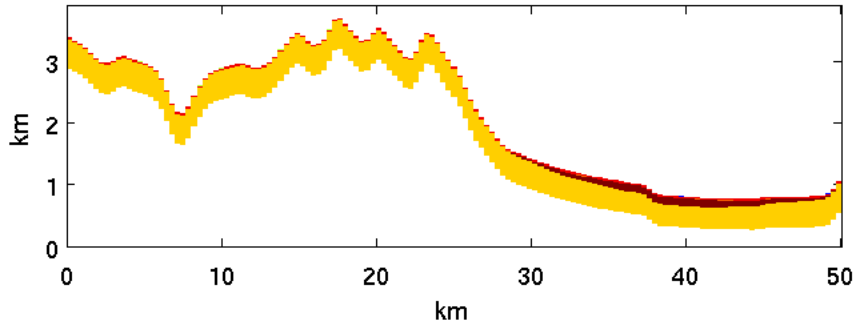


(c)

Figure 3.4. Cross-sections of the 3D indicator field representing subsurface geology in PF.CLM across Owens Valley at: (a) j=144 (northernmost slice) (b) j=72 (c) j=1 (southernmost slice) Colors are same as in colorbar for Figure 3.3

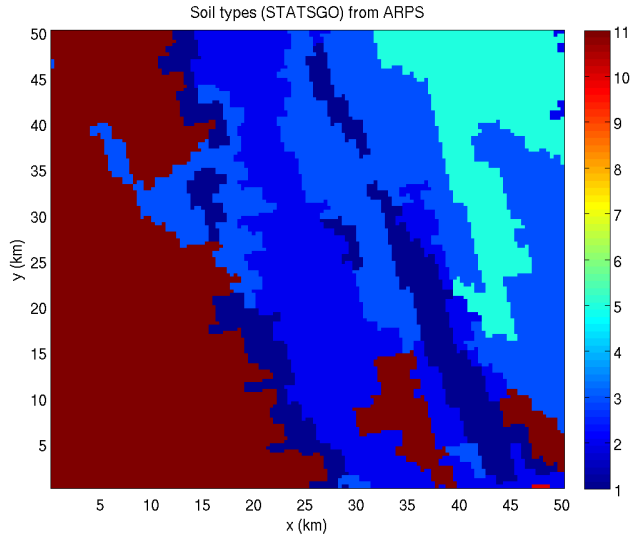


(a) Colobar: 01) Sand 02) Loamy sand 03) Sandy loam 04) Silt loam 05) Loam 06) Sandy clay loam 07) Silty clay loam 08) Clay loam 09) Sandy clay 10) Silty clay 11) Clay

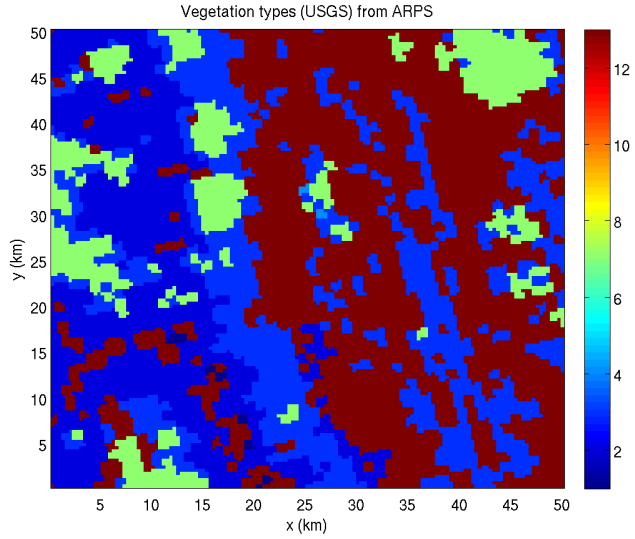


(b) Colorbar: 01) Desert 02) Tundra 03) Grassland 04) Grassland with shrub cover 05) Grassland with tree cover 06) Deciduous forest 07) Evergreen forest 08) Rain forest 09) Ice 10) Cultivation 11) Bog or marsh 12) Dwarf shrub 13) Semidesert

Figure 3.5. (a) Surface soil (STATSGO) and (b) vegetation types (USGS) at 1 km resoultion, taken from ARPS and used in PF.CLM. Note that soil types 5-8 are represented as one soil type in PF.CLM, "loam/clay loam". Types 10 and 11 are represented as type, "silty clay/clay" and type 9 does not appear within the domain, so is not represented in PF.CLM.

### 3.4.3 Initial and boundary conditions

For all simulations, the initial subsurface pressure head [m] was set to hydrostatic conditions with the water table located 30 m below the ground surface. Initial saturation follows directly from the pressure field, with the subsurface fully saturated below 30 m. (See Fig. 3.6.)

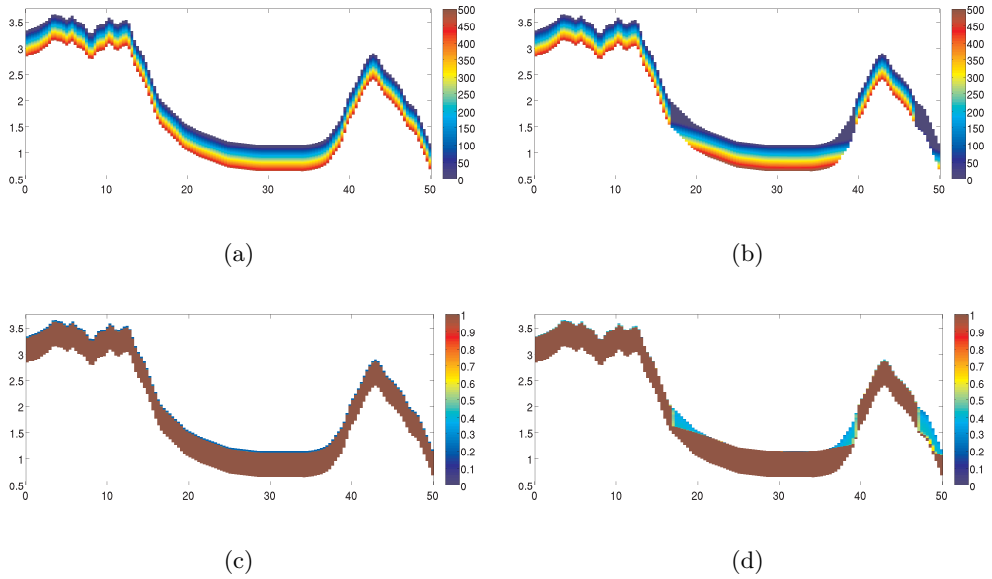

Figure 3.6. (a) PF.CLM initial pressure head [m] (same for all 2D and 3D simulations), (b) pressure [m] after 2 years for simple geology 2D spin-up, (c) initial saturation [-] (same for all 2D and 3D simulations), (d) saturation [-] after 2 years for simple geology 2D spin-up.

CLM requires eight meteorological forcing variables as input: atmospheric pressure, precipitation rate, downward shortwave radiation flux, downward longwave radiation flux, temperature (at 2m above the ground surface), winds (U and V at 10m), and specific humidity (2m). For the 2D simulation with distributed forcing, spatially interpolated meteorological forcing from NARR is provided to CLM at every cell on the ground surface at every time step (3 hrs for the 2D simulations, 1 hr for the 3D simulations). This distributed forcing allows meteoroligical conditions to vary over the PF.CLM domain during the year-long spin-up procedure. For the 2D and 3D simulations with uniform forcing, a single point at the center of the domain was used, representing conditions interpolated between the closest NARR grid points within the horizontal extent of the 3D domain. NARR forcing data was read and extracted through modification of an ARPS pre-processing program.

For future work, it is recommended that if possible, observational data should be used for meteorological forcing. This presents new challenges, as observations without gaps over a period as long as a year may be difficult to find. Also finding observations at locations which realistically represent the weather patterns over certain regions of the domain may not exist, or may be difficult to implement in the model, depending on topography and what is known about weather in those regions.

### 3.4.4 Spin-up procedure

An off-line spin-up procedure is used here to allow the model to reach hydrologic equilibrium. PF.CLM is run for a full water year using meteorological forcing from NARR. The coupled model is run repeatedly for the same water year (2006) of forcing data until the ratio of the change in storage to the total precipitation is less than 1%. The results presented here for the simple subsurface geology 2D set-up with distributed forcing are results from the second year of the spin-up, when this condition had not yet been met. This simulation was run in serial and only completed a portion of the spin-up for testing purposes. Regardless, the soil moisture values in the simple geology 2D domain are in the same range as those measured during the T-REX field campaign. Fig. 3.6 shows how the pressure and saturation fields have evolved from the initial conditions after two years. Subsurface flow is much slower in the regions below the peaks since values of porosity and hyraulic conductivity in those regions are much lower than those assigned to the alluvium of the valley in the model. Changes in saturation and pressure are therefore more evident in the valley region and eastern slope of the Inyo mountains.

The complex geology 2D simulation with uniform forcing was run in parallel for 9 years of spin-up. In the 9th year, the change in storage compared to total precipitation is less than the threshold value of 1%. Plots of surface pressure (depth of water over each cell), surface saturation and soil moisture, as well as water table depth are shown in Figure 3.11 for selected years. The simulation has reached equilibrium, as evidenced by the similarities between years 6 and 9 compared to the significant differences between years 1 and 2.

### 3.4.5 Computational considerations

The number of grid points necessary to resolve the mountainous terrain of Owens Valley necessitates the use of parallel computing. Parallel computing refers to splitting up a problem into smaller parts and carrying out concurrent calculations for each of the sub-parts using multiple CPUs. In our case, the domain is split into smaller sub-domains and all calculations for each sub-domain are carried out on a serparate processor. There must be a balance between the number of processors used and the domain size; if the number of grid points in a sub-domain is too small, then more time will be spent communicating with the processors of neighboring sub-domains than in actual calculation of results. The number of processors for a given problem must be optimized so that communication time between processors is minimized and time spent computing is split evenly among as many processors as possible. Achieving an even split, such that each processor carries roughly the same computational load, is desirable.

PF.CLM is capable of splitting the domain in any of the three Cartesian directions. For our problem, however, we are restricted to splitting horizontally only due to the distribution of active cells throughout the domain. There are the same number of active cells in any given vertical column within the domain, but these 500 active cells are at varying vertical levels depending on the terrain height at a given horizontal position. Thus, if the domain were to be split vertically, the load on each processor would vary between very light (very few active cells, or even none at all) and very heavy (many or all active cells). A series of test simulations were run to determine which split configuration would be most efficient with our grid. This set of tests also revealed a bug in the code at the message-passing interfaces of the split sub-domains. Figure 3.7 shows results from 12x12, 16x16, and 24x24 processor splits (144, 256, and 576 processors, respectively). The hatched patterns visible in these plots of water table depth are also visible in plots of saturation, pressure, and soil

moisture. This problem was corrected by fixing the Message Passing Interface (MPI) routines in ParFlow, working in conjunction with scientists and Lawrence Livermore National Laboratory.

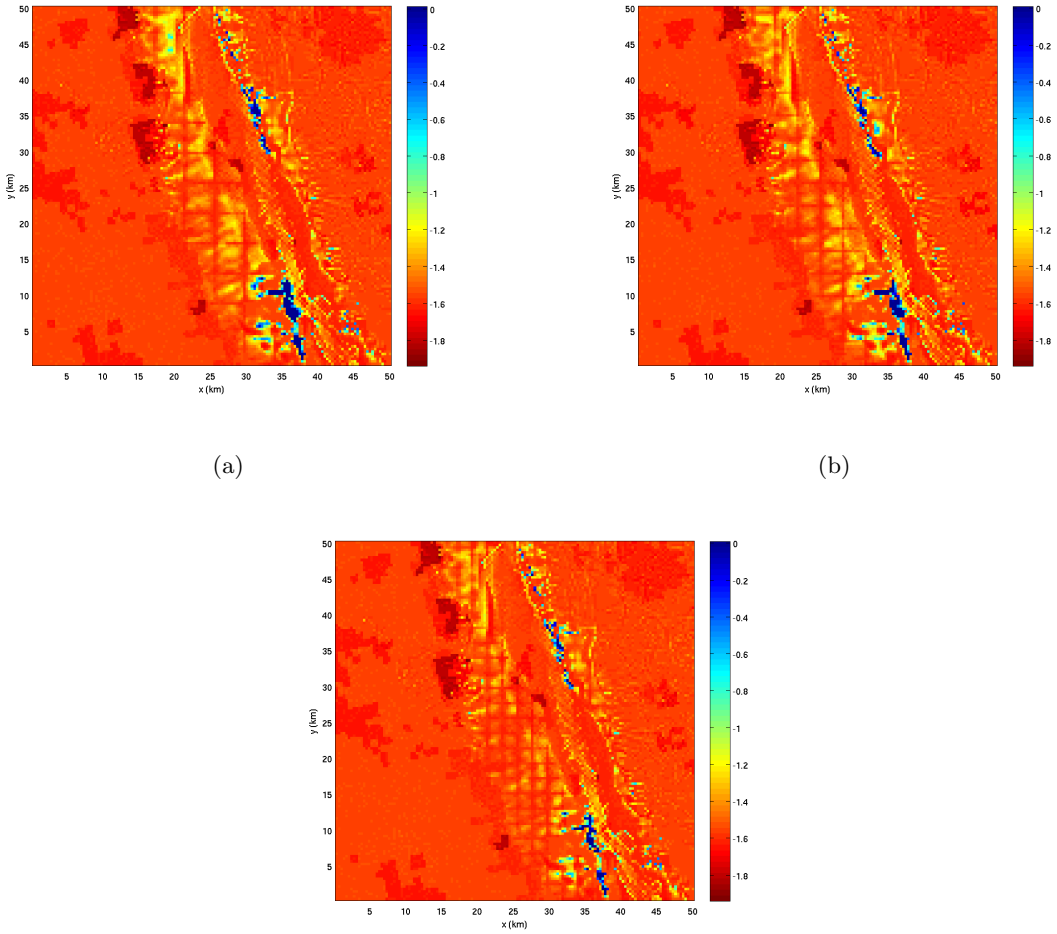


(a) (b)

(c)

Figure 3.7. Pressure (meters of water over each grid cell) from PF.CLM with message-passing problem for (a) 12x12, (b) 16x16, and (c) 24x24 splits for a section of Owens Valley at 350 m resolution centered at Independence, California after 5 days of spin-up.

Parallel simulations in 3D still required significant amounts of time during spin-up. With 576, 256, and 144 processors, these large simulations required more than 6, 10, and 15 hours of real time to complete 5 days of spin-up respectively. These times are approximate and sometimes were much longer, depending on the conditions (how much water was moving within the domain). Queues on the supercomputers made wait time between simulations several days or more. With debugging issues related to parallelization as well as the exceedingly dry conditions of Owens Valley, which had not been encountered before by other users of PF.CLM, the 3D spin-up simulations could not be completed within the timeframe of this dissertation project. Work is still in progress to correct an unphysical flux boundary condition set by CLM and passed to the ParFlow solver which results when there are long periods without any precipitation, as is the case in Owens Valley. Preliminary

results are presented, however and the full methodology is described. In contrast, for the 2D spin-up, using 8 processors was sufficient to allow one year of spin-up per one day of real time such that a full spin-up cycle was possible with the 2D set-up.

## 3.5 Results

In this section, results from the 2D spin-ups will be presented, as well as some partial spin-up results from the 3D simulations.

Volumetric soil moisture is given by saturation multiplied by porosity. Thus, saturation is extracted from the surface cells at the date for which the initialization is needed (in this case, March 29, 2006). Soil moisture from the 2D PF.CLM spin-ups is shown in Figure 3.8, along with observed values from the main transect shown in 3.2, and interpolated values from NAM and NARR at the same location as the PF.CLM slices, for comparison. Soil moisture values from the simple geology PF.CLM compare quite well with measured values, despite the simplifications in the representation of the subsurface and the limitations of a 2D simulation. The complex geology 2D simulation shows a more pronounced increase in soil moisture around the Owens River flood plain, which is closer to the expected soil moisture pattern based on observations, however, overall soil moisture values from the complex geology simulations are significantly higher than observed values. These increased values may be attributable in part to the uniform forcing used in the complex geology simulations, (in contrast to the distributed forcing used in the simple geology simulations), but also certainly to the major difference in surface and subsurface geology patterns, which possess different hydraulic properties. Some of the values representing these properties should probably be adjusted based on the results of the spin-up, but care should be taken not to used these hydraulic properties as tuning parameters, since the main purpose of this physically-based model is to ensure as true a representation of the physics as possible. The more pronounced river signature in the complex geology simulation is most likely present due of the way y-slopes were assigned. Slopes in the y-direction (into and out of the page for the 2D simulations) along the river flood plain were an order of magnitude larger in the simple geology simulations than in the complex geology simulations, such that too much water was leaving the domain at those locations. These values were adjusted for the complex geology spin-up.

Though values from the model are about a factor of 3 higher than the observed values, the complex geology spin-up accurately captures the observed soil moisture pattern along the valley transect.

The full 3D simulation was launched for the first time with a 24x24 split and ran for about 2 months of spin-up before the solver became mired in an unphysical set of conditions. The problem was with the flat slopes on the valley floor, where the Owens River would flow in reality. Grid resolution of 350 m is not sufficient to resolve a river that is typically less than 100 m wide, so the river bed and flood plain appear nearly flat on the model grid. ParFlow uses a kinematic wave formulation to route flow from one cell to the next based on the bed slope. Because of this, water collected in unphysical "water towers" along the edges of the flat flood plane, such that there were more than 5 meters of water over more than 60 cells on the valley floor. This is illustrated in Figure 3.9(a). This problem and its fix are described in detail in Chapter 4. Explained briefly, stream location data for the Owens River was integrated into the existing digital elevation model (DEM), so that the valley floor is no longer flat and the kinematic wave approximation approach

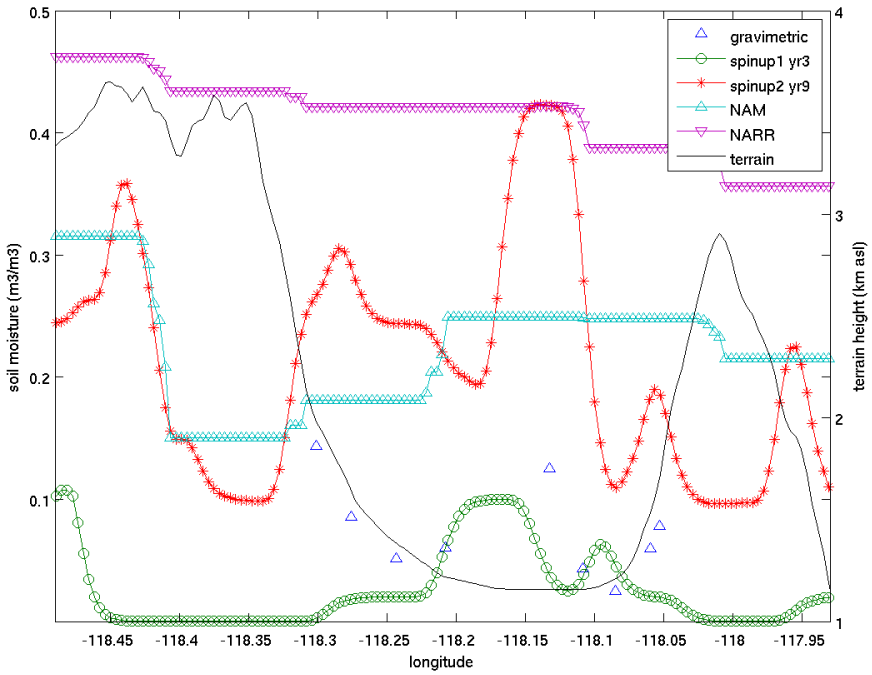


Figure 3.8. Transect of soil moisture ($m^3/m^3$) across Owens Valley near latitude 36.8 from observations, standard initialization datasets (NAM and NARR), and spin-ups 1 and 2 with PF.CLM.

used in ParFlow allows water to flow from the valley walls to the river and along it. The modified DEM with blue arrows showing the direction of flow along the river's path on the 350 m model grid are shown in Figure 3.9(b).

The final set-up was launched with a 16x16 split and the Owens River integrated into the DEM such that the valley floor no longer contained any zero or near zero slopes (as shown in Figure 3.9(b)). Results from 90 days into this spin-up are shown in Figure 3.10. The pressure field seems to be developing normally and producing realistic values of soil moisture. However, the solver ran into problems with unphysical flux values provided by CLM due to extreme dry conditions on portions of the valley side walls. PF.CLM has not previously been used in arid climates with complex, steep terrain like Owens Valley. ParFlow alone performs normally, it is the coupling in PF.CLM that prevents the simulations from advancing beyond 90 days. Overcoming this challenge will require further research.

To see how soil moisture varies with terrain and also how the distribution correlates with both vegetation and soil types, 3D surface representations of the data are given in Figures 3.14, 3.13, and 3.12. Though the model has not completed its spin-up, the influence of topography on the soil moisture field obtained after 90 days of simulation is nonetheless clearly visible in the model results. This can be taken as evidence that altitude-dependent soil moisture initialization of atmospheric simulations described in Chapter 6 is appropriate, based on the results of 2D PF.CLM spin-ups as well as observations of soil moisture from the Terrain-Induced Rotor Experiment (T-REX). The details of assigning altitude-dependent soil moisture in Owens Valley will be described in detail in Chapter 6.

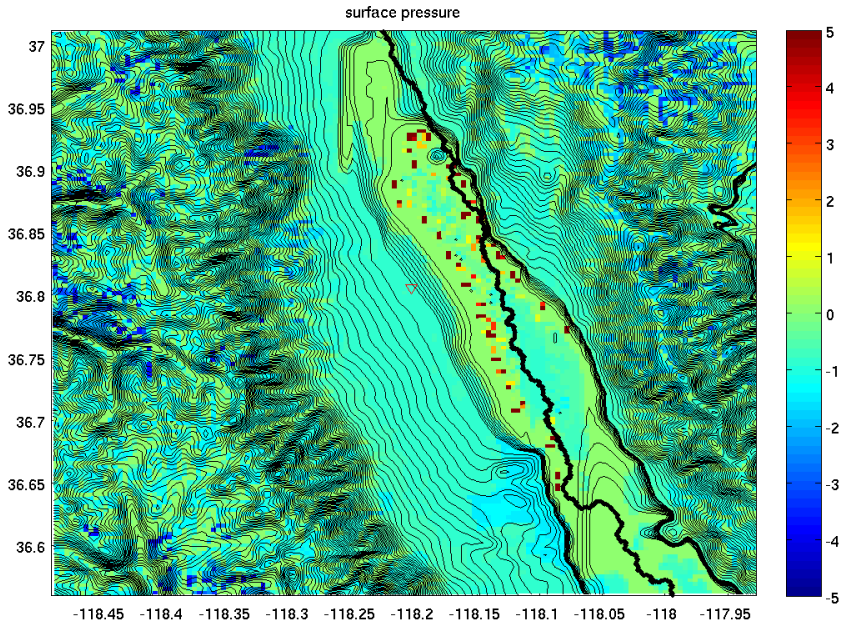


(a)

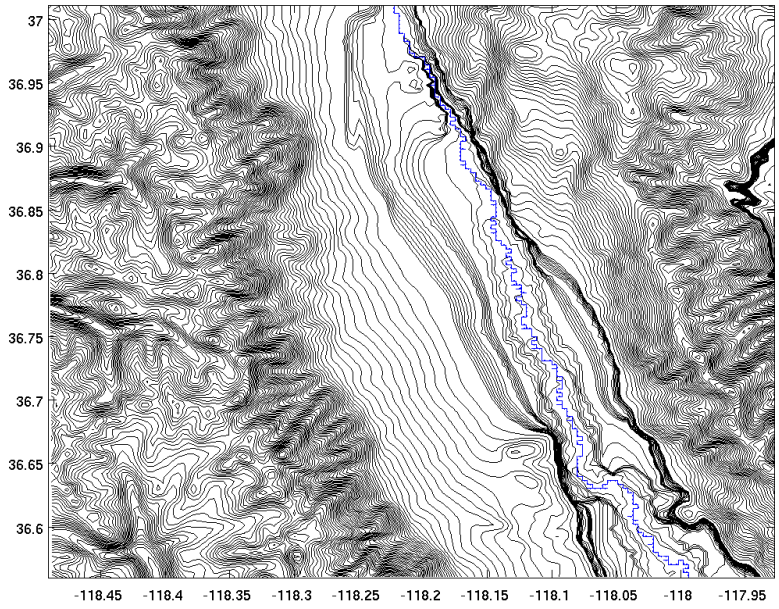


(b)

Figure 3.9. (a) Pressure (m) over each grid cell with original DEM terrain contours overlaid. (b) Terrain contours for modified DEM with Owens River represented on the 350 m grid as described in Chapter 4. Contours at 50 m intervals above 1200 m, and at 5m intervals below.

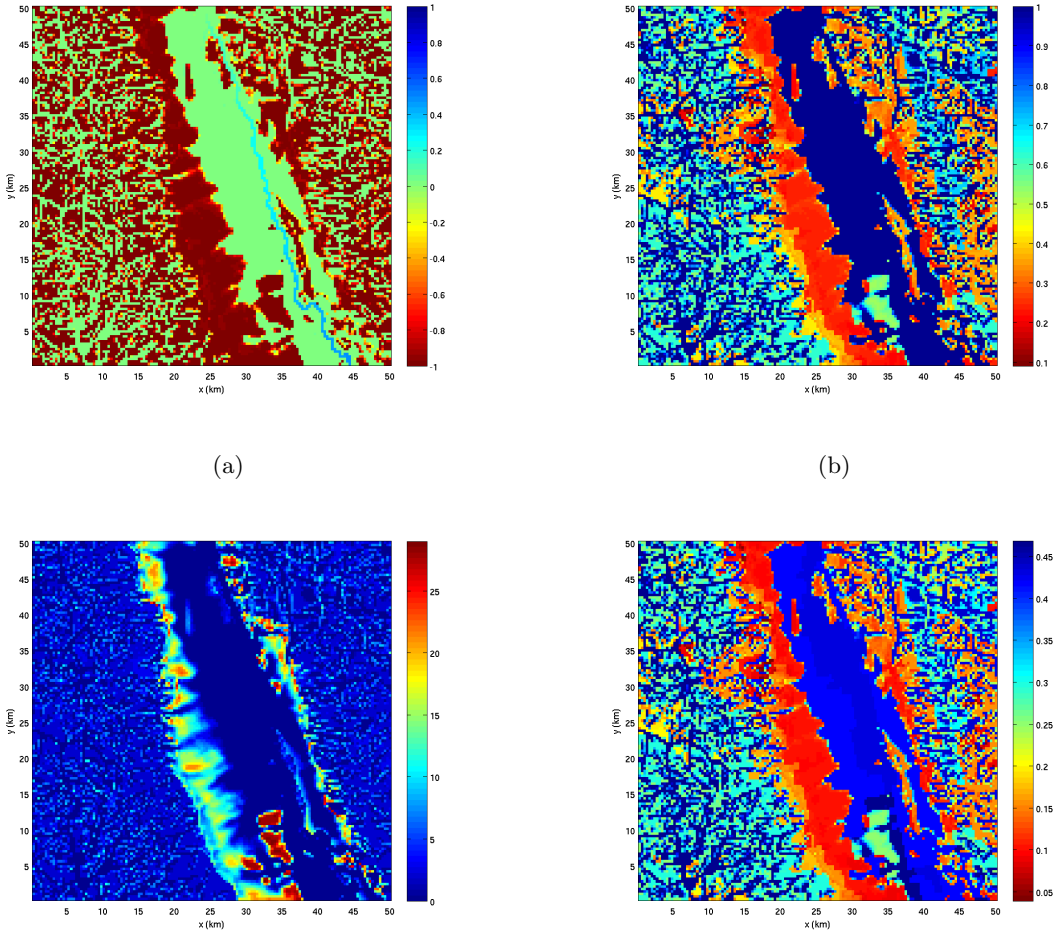


(a) (b)

(c) (d)

Figure 3.10. Results of the 3D simulation at 90 days into the spin-up (December 29, 2005). (a) Surface pressure (meters over a grid cell surface) (b) Surface saturation (% pore space that is filled with water) (c) Water table depth (m) (d) Surface soil moisture ($m^3/m^3$)

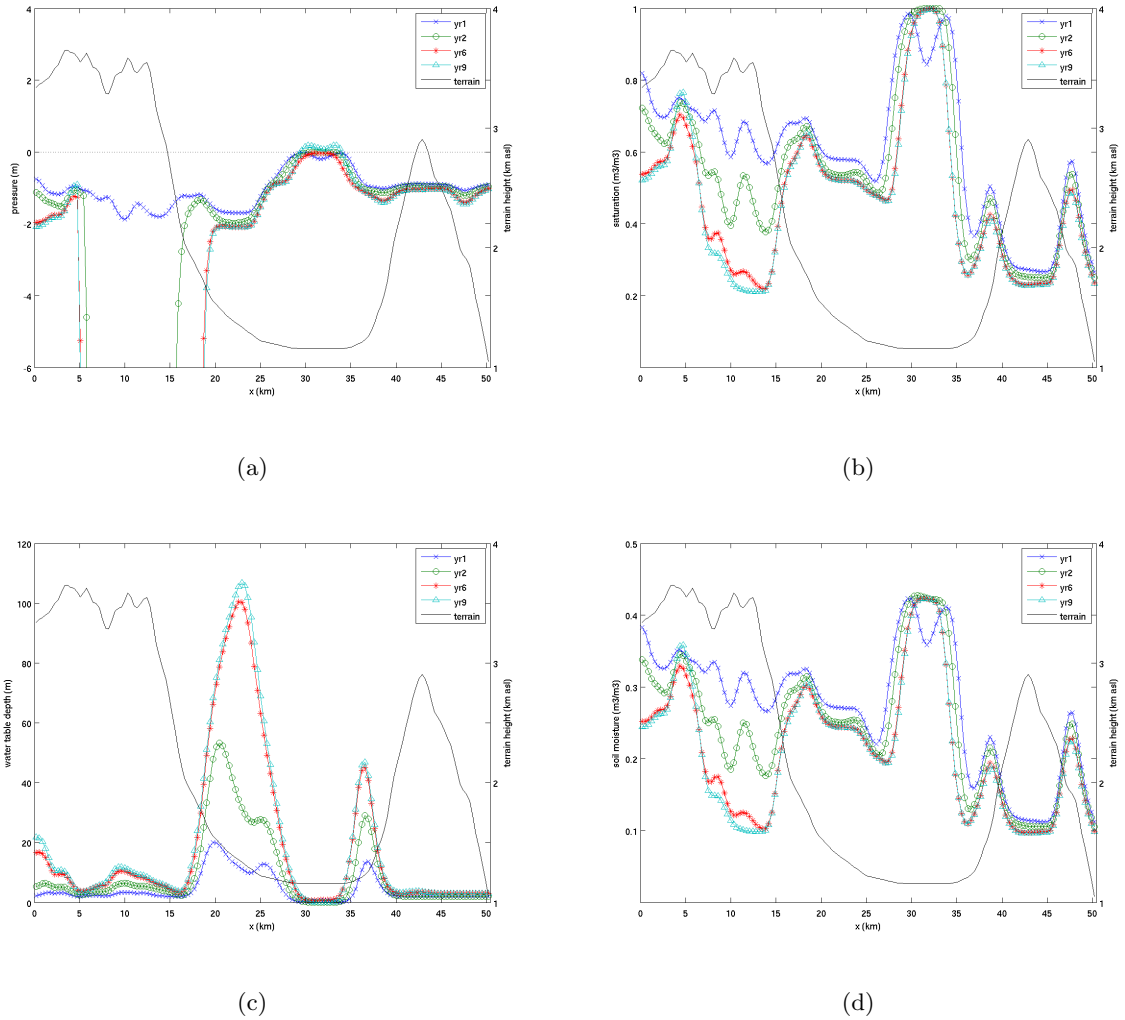


(a) (b)

(c) (d)

Figure 3.11. Transects across Owens Valley. (a) Surface pressure (meters over a grid cell surface) (b) Surface saturation (% pore space that is filled with water) (c) Water table depth (m) (d) Surface soil moisture ($m^3/m^3$)

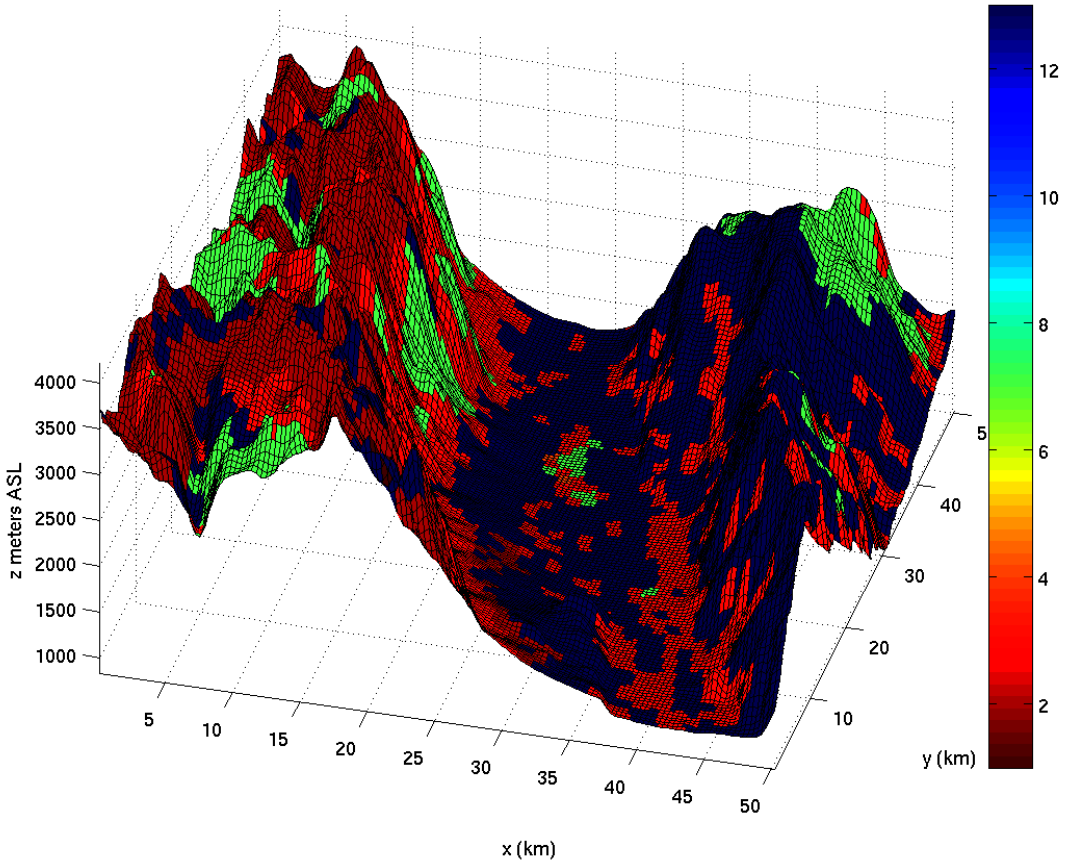


Figure 3.12. 3D representation of vegetation types on Owens Valley topography. Colorbar same as in Figure 3.5(b): 01) Desert 02) Tundra 03) Grassland 04) Grassland with shrub cover 05) Grassland with tree cover 06) Deciduous forest 07) Evergreen forest 08) Rain forest 09) Ice 10) Cultivation 11) Bog or marsh 12) Dwarf shrub 13) Semidesert

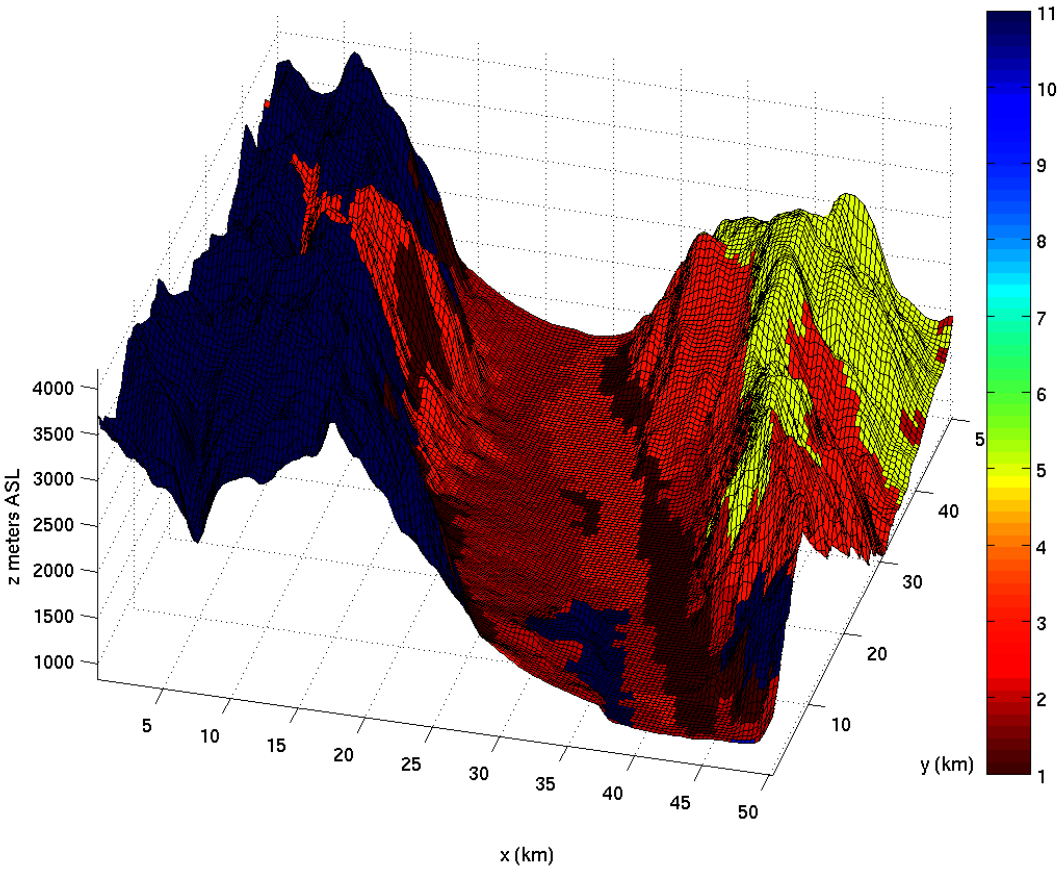


Figure 3.13. 3D representation of surface soil types on Owens Valley topography. Colorbar (same as in Figure 3.5(a)): 01) Sand 02) Loamy sand 03) Sandy loam 04) Silt loam 05) Loam 06) Sandy clay loam 07) Silty clay loam 08) Clay loam 09) Sandy clay 10) Silty clay 11) Clay

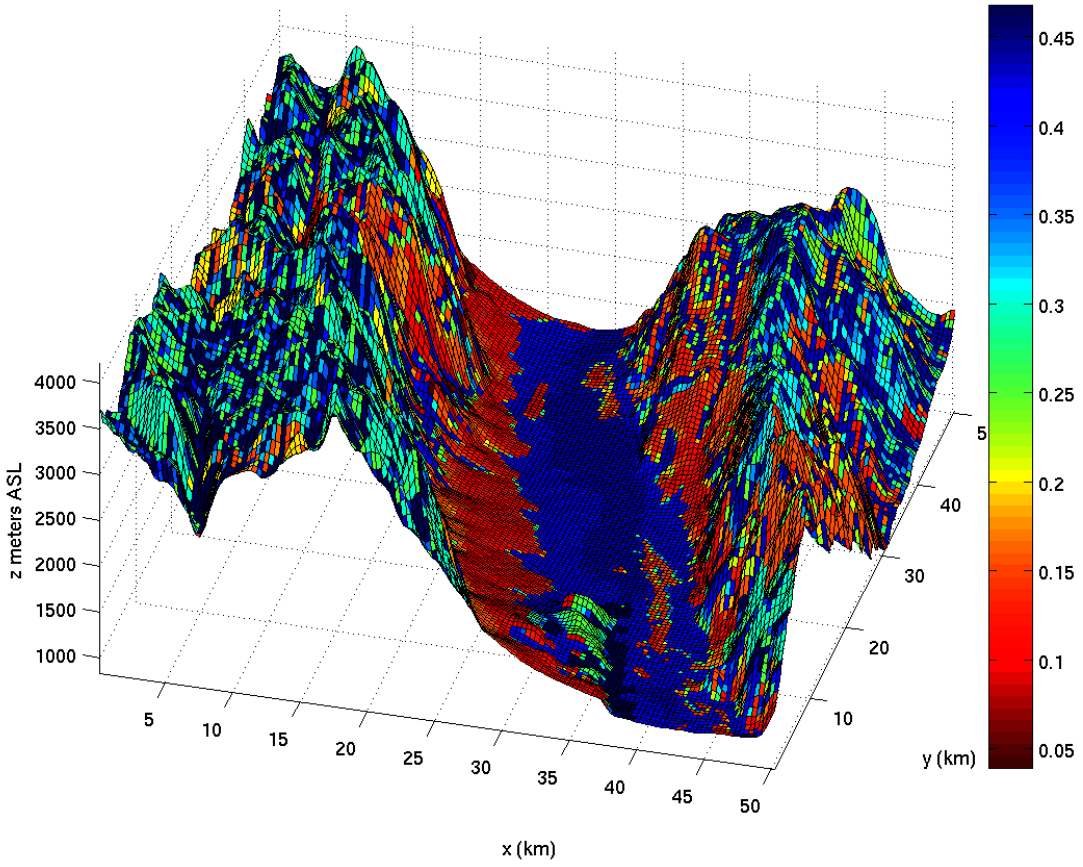


Figure 3.14. 3D representation of soil moisture ($m^3/m^3$) on Owens Valley topography from the 3D simulation after 90 days of spin-up (December 29, 2005).

# Chapter 4

# Flow direction enforcement using sub-grid scale stream data

## 4.1 Introduction

This chapter addresses flow routing through flat areas in a digital elevation model as is encountered at 350 m resolution at the center of Owens Valley and discussed in Chapter 3 on coupled hydrologic modeling. Such flat areas occur frequently because river flood plains tend to be relatively flat on grids which are too coarse to resolve the river channel itself. Presented here is an algorithm which maps stream location data to a model grid, then calculates a continuous flow path by setting slopes along the stream line to always point to a downstream neighboring cell.

## 4.2 Background

Computational constraints limit the scales of topography that can be resolved in hydrologic models. With insufficient grid resolution, areas with little terrain slope, such as river flood plains, can become nearly or completely flat on a model grid. Slopes and terrain elevations are often used to determine flow from one cell to the next, so grid cells with zero or very small slopes act as sinks and may unrealistically retain water. To address this problem, the approach outlined herein integrates sub-grid scale stream location data with the local Digital Elevation Model (DEM), then routes flow to and along the stream.

The approach presented here consists of two main steps: 1) retrieve and map flowline points from the National Hydrography Dataset (NHD) to the local DEM, 2) order these points so that each point is on the list next to its upstream and downstream neighbor, then assign flow directions accordingly. These steps are carried out in preprocessing and flow direction enforcement programs which are summarized in the flowcharts in Figures 4.1 and 4.2. A case study in Owens Valley, California

is presented which demonstrates the flow-direction enforcement capabilities of the algorithm when routing flow through a flat flood plain.

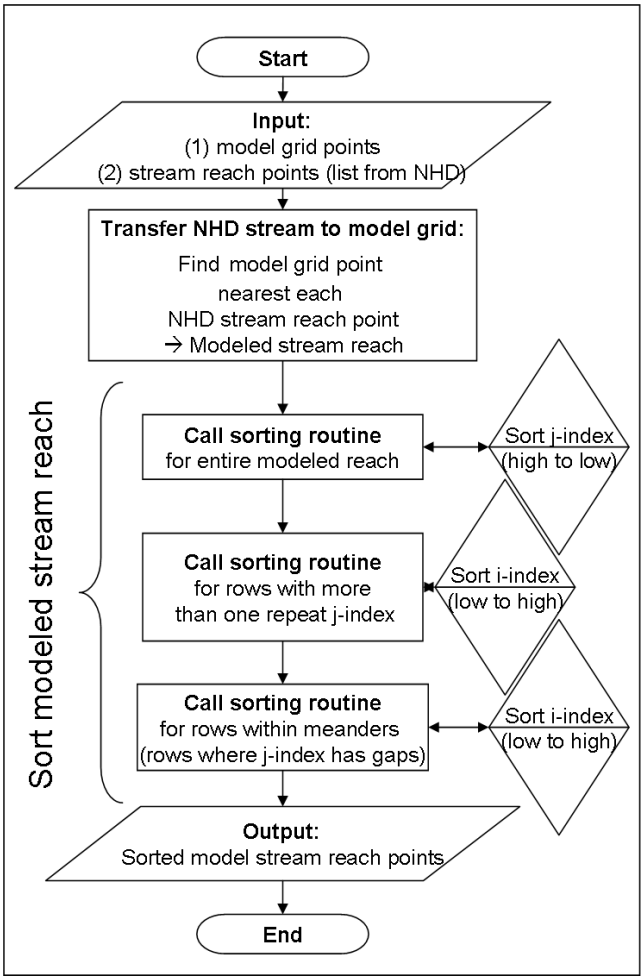


Figure 4.1. Flowchart outlining the preprocessing program.

Gravity ensures that water flows downhill, and so in hydrologic modeling, it is important to know which way is down. That is, at any given point on the land surface of the model domain, one must know the slope of the topography (at least approximately). So from the most sophisticated to the simplest, hydrologic models come in a wide variety of configurations, but they all must resolve topography on some level. In general, the higher the resolution, the more points there are to describe the topography and the flows over and through it, so the closer to reality the computed flow becomes. Of course, there are limits on the number of computational nodes that can be allotted to any given problem. Scientific computing continues to improve speed and efficiency of computers, but not fast enough to allow sufficiently high resolution of topography in many models, such that slopes calculated from the available Digital Elevation Model determine realistic flow paths.

Flow networks calculated from DEMs that do not adequately resolve the topography cannot be expected to consistently produce realistic flow paths. Much work has been done to define DEM-derived flow networks which at least preserve realistic flow patterns in a statistical sense. [*Fairfield*

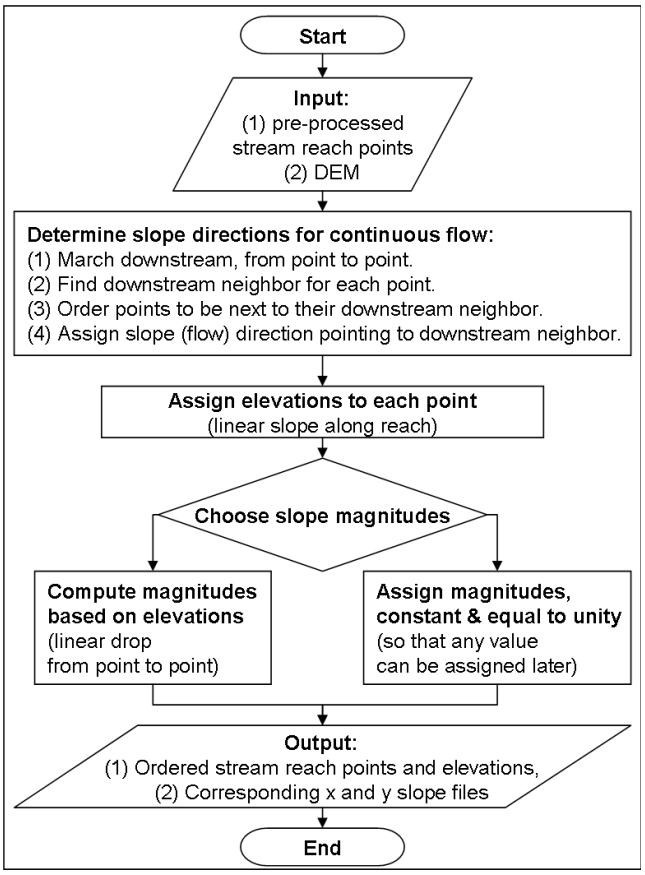


Figure 4.2. Flowchart outlining the flow direction enforcement algorithm.

*and Leymarie*, 1991; *Costa-Cabral and Burges*, 1994] This type of approach is valuable, especially when working at very low resolutions compared to much of the underlying stream network, and when an average flow distribution is the goal. The approach presented here is intended to be used for applications where the true locations of the main flow path or paths are important, and the DEM does not sufficiently resolve the topography to allow for continuous flow in a stream or stream network. One example application is in land-atmosphere coupling where the goal is to obtain a realistic soil moisture distribution from the hydrologic model. Sensible and latent heat fluxes at the surface, which affect flow in the atmospheric boundary layer, are particularly sensitive to soil moisture. At the same time, these surface fluxes are often used as boundary conditions for hydrologic models. Thus feedbacks at the land-atmosphere interface can be significant and there are implications for computational hydrology as well as numerical weather prediction. Other example applications might include groundwater-surface water coupling or vegetation studies, where again the details of the spatial variations in the land surface are important.

The approach outlined here incorporates available fine resolution stream location data from the National Hydrography Dataset (NHD) into the original coarse DEM using the preprocessing program, then uses a flow direction enforcement algorithm to assign flow directions for continuous flow along the stream reach in the context of a four-direction flow scheme.

Widely used flow network and routing schemes, such as those described in *Marks et al.* [1984]; *O'Callaghan and Mark* [1984]; *Tarboton* [1997]; *Orlandini et al.* [2003], and many others, are sometimes capable of routing flow through flat areas, but do so only based on information contained in the local DEM. Such schemes typically only allow flow in one, possibly two directions. The approach of *Kenny and Matthews* [2005] and *Kenny et al.* [2008] (using Arc/GIS) incorporates stream location data so that continuous stream flow is represented within the flow network, with eight possible flow directions and one assigned flow direction per grid cell. The method introduced here of stream integration and flow direction enforcement can be situated within the context of *Kenny et al.* [2008] Table 2 as a combination of portions of Methods 1, 6, and 8. Like the approach presented here, Method 1 (Australian National University DEM, or ANUDEM, [*Hutchinson*, 1989]) ensures a downslope gradient for all cells along the hydrology network, Method 6 (stream burning, [*Saunders and Maidment*, 1996; *Mizgalewicz and Maidment*, 1996]) requires lowering the elevations of cells along a stream with respect to the original DEM elevations, and Method 8 [*Kenny and Matthews*, 2005] imposes flow directions along the hydrology network. The method presented here is unique in combining the essential elements of these approaches in a non-commercial algorithm. Versatile due to its simplicity, this method allows implementation for a variety of applications.

Much work has been done in the context of single or two direction flow schemes, and the approach presented here can be applied as part of a flow "network" used by such schemes. Additionally, the method presented here is mass conserving, (which is not required of eight direction flow schemes,) and is designed for applications such as surface-subsurface and land-atmosphere coupling where the main flow path or paths are important, but not resolved on the local DEM. The approach is illustrated here with a fully coupled, surface-subsurface flow simulation using ParFlow, where Richards' equation and the kinematic wave equation are fully integrated, e.g. *Kollet and Maxwell* [2006], allowing flow to enter or exit any of four cell faces.

Consider a specific example of a situation where the approach presented here is applicable. A river 10 m wide running through a flood plain is not resolved on a grid with horizontal grid spacing greater than 5 m. The spatial extent of many catchments is on the order of tens of kilometers. This means that in most cases horizontal grid spacing on the order of hundreds of meters or more must be used if the computational domain is to remain within the realm of practicality. If the horizontal

grid spacing is 100 m or more, and the river is only 10 m in width, then the river is not resolved on the model grid. Likely, the flood plain will appear essentially flat on the model grid, giving the model no clues as to how to route water out of the region. As a result, unrealistic ponding may occur and predicted outflows will not reflect reality.

This is the case in Owens Valley, a rift valley that lies between the Sierra Nevada and White-Inyo mountains in California. Topography at 350 m resolution for a section of the Owens Valley region, centered around the town of Independence, California is shown in Figure 4.3(a). The Owens River is not well represented on a 350 m DEM. In fact, the flood plain through which the river flows is nearly flat at this resolution, as shown in Figure 4.3(b). An overland flow scheme solving the kinematic wave equation will begin to collect water on cells with such tiny slopes, as shown in Figure 4.3(c). These virtual "water towers" are scattered around the edges of the flat area, effectively collecting and holding the water that should have drained through the Owens River. Some models might use the diffusion wave approximation, and while this approach might mitigate some of the water accumulation on cells around the edges of the valley, it would still lack the sub-grid scale information necessary to route flow realistically with respect to the river. Other models use a two-scale approach, where a 1-D kinematic river is embedded into "river cells", however, such an approach does not allow any interaction with neighboring cells.

In the example illustrated in Figure 4.3(c), virtual "water towers" occurred despite the fact that the DEM provided to the hydrologic model did not contain any cells with zero slope. That is, all sinks had technically been filled. The problem arises from what we will refer to as "virtual sinks", or cells with slopes of magnitude *near* zero. While some flood plains and lakebeds are naturally occurring sinks or virtual sinks, there are many other cases where sinks arise because of insufficient grid resolution, or even as artifacts in the DEM itself (e.g. trees blocking the mouth of a valley). Sinks are dealt with mainly in two ways: filling, or allowing flow to drain "uphill" to next lowest cell. Filling sinks artifically raises the height of the terrain to be equal to or higher than the height of neighboring cells. On the other hand, choosing a sink neighbor, which by definition has a higher terrain height than the sink itself, to be the sink outlet seems illogical, but may be a good choice in some cases where sinks represent basins which have outlets that are not resolved on the given model DEM. Most algorithms for filling sinks will either do a step fill, that is, make the terrain height for a sink a specified amount higher (e.g. 1 meter), or, will do a local average of surrounding terrain heights plus a constant (which is somewhat arbitrary) to bring the sink higher than the level of its neighbors. Both methods are implemented in an iterative fashion so that sinks are gradually filled; the method is successful when the entire domain is sink free. Averaging tends to smooth out necessary terrain variations in hilly or mountainous regions, while step fill algorithms in particular can be problematic in regions with little terrain variation becuase they tend to make smooth areas bumpy, rather than giving a gentle slope.

For example, the DEM shown in Figure 4.4(a) contains numerous sinks. The flat area on the valley floor shown in 4.4(a) becomes bumpy when filled by a simple step fill. To avoid this problem, we use a sink-filling algorithm which employs a step fill in regions with highly variable terrain (mountains), and a local average in regions with little terrain variation (valley floor). In some sense the step fill can be thought of as acting on the smaller scales (a single grid cell), while the averaging incorporates more of the large scale terrain variations (surrounding grid cells). Incorporating the river into a relatively coarse DEM means transferring some of the sub-grid scale terrain variations to the grid scale. Use of the averaging method in the valley region near the river can be seen as blending the small and larger scale variations.

The capabilities of the preprocessing and flow routing algorithms are demonstrated in a case

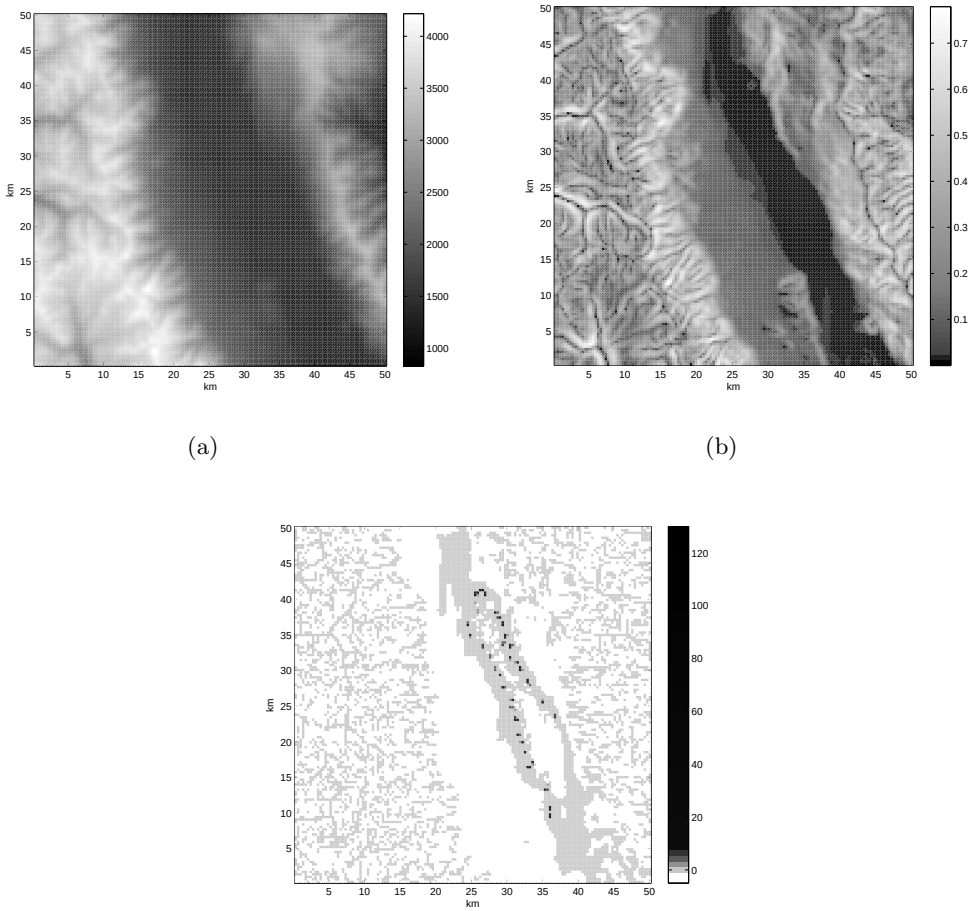


(a) (b)

(c)

Figure 4.3. (a) 350 m DEM for Owens Valley, centered at Independence, CA, (colorbar is altitude in meters above sea level) (b) Slope magnitudes [m/m] for the DEM shown in (a) , (c) water height over each grid cell in meters; red indicates "water towers" generated by kinematic wave overland flow scheme using the DEM and slopes shown in (a) and (b)

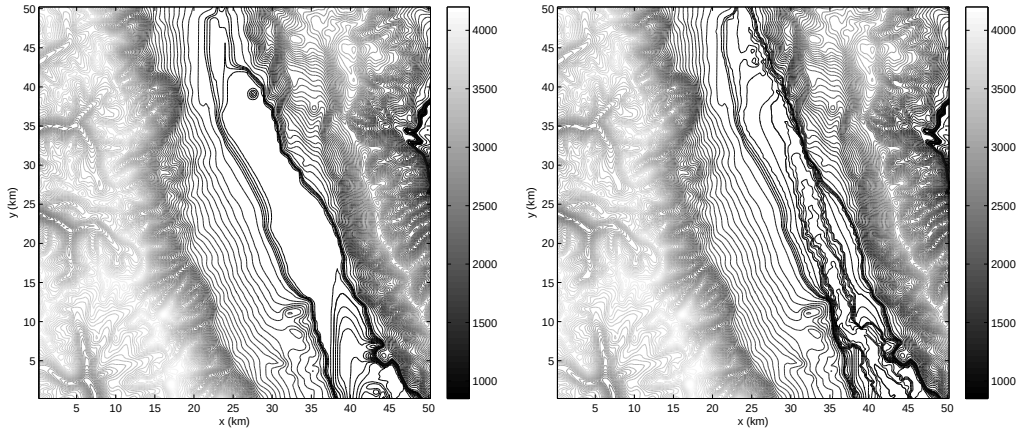


(a) (b)

Figure 4.4. Grayscale contours for Owens Valley terrain at 50 m intervals. Black contours at 5 m intervals between 1100 and 1180 m. (a) Original DEM, (b) DEM with river integrated.

study for Owens Valley, California, using an integrated surface water-groundwater model, ParFlow. This rain and recession case illustrates how flow is routed through the flat flood plain in Owens Valley (shown in Figure 4.3), by representing the Owens River on the model grid through modification of the original DEM as well as flow direction enforcement along the river.

## 4.3 Concept

To overcome the flat area problem, we have written a set of programs which are capable of integrating a river or stream reach into an existing DEM, such that slopes, (and therefore flow) along the reach will be continuous. Recall that the flat area problem arises from the fact that hydrologic models often use DEMs which are too coarse to resolve the hydrography of a flood plain, so that the plain becomes essentially flat. Many hydrologic models rely on slope magnitudes and directions to determine the quantity and direction of flow that should be routed through a given area; thus zero or constant slopes over a given area do not offer the model clues to realistically route flow. To allow some of the subgrid-scale slopes to be represented on the model grid, we integrate the river or stream reach into the existing DEM. Integrating the main river or stream reach into the DEM and guaranteeing continuous slopes means that water will flow to the river and along it, rather than ponding (unrealistically) in the flat area. The end result should look something like Figure 4.4(b), where the valley floor has a gentle slope down to the river. Keep in mind that the original DEM did not accurately represent the hydrologically relevant topography (e.g. river channel), so the modifications to this DEM do not make the DEM any *less* accurate for our purposes. The goal is to allow more realistic flow patterns, and this is achieved by incorporating the river, from NHD flowline data, into the relatively coarse model grid.

Stream network flowline data is available from the National Hydrography Dataset, NHD. Latitude and longitude points describing the flowpath of a river or stream branch can be extracted from the flowline files of the NHD. These points are then transferred onto the model grid using a

preprocessing program. In the main algorithm, the list of points representing the river or stream on the model grid are then ordered and given slope and direction such that flow will be continuous from one point to the next, starting from the point furthest upstream to that furthest downstream, according to a four-direction flow scheme. (The hydrologic model we used to test the algorithm employs a four-direction scheme, rather than an eight-direction scheme, in order to preserve mass conservation.) Flow is strictly from one point to another, with no provisions for branching, though stream branches could easily be routed by running the algorithm for the set of points representing each individual branch.

Separate slope files for the x and y directions are output, with corresponding i,j indices for each point, and these can be directly incorporated into the slope files for a hydrologic model (with no changes to the underlying DEM). Alternatively, terrain heights for points along the stream corresponding to the assigned slopes can be integrated into the DEM, and assigned stream slopes can still be used to ensure continuous stream flow. An overview of the preprocessing algorithm is shown in the flowchart in Figure 4.1. The main algorithm is summarized in Figure 4.2. Details of the algorithms are provided below.

## 4.4 Processing of stream location data for flow routing

### 4.4.1 Preprocessing: retrieval and sorting

The preprocessing program is used to: 1) retrieve latitude and longitude of the river or stream reach (NHD flowline data) and transfer the reach onto the model grid, and 2) sort these points by grid index so that the main algorithm can run most efficiently (see Figure 4.1).

The former is accomplished by direct comparison of latitude and longitude values (of model grid points to river flowline points) so that the model grid point (if any) that is closest to the location of the river flowline point is chosen. In the example case presented here, points along the Owens River were extracted to a model grid where a series of several hundred points now represent the more than 2000 points that originally described the river in the NHD, (see Figure 4.5). Output points are first sorted in decreasing j-order, then in increasing i-order using Quicksort [*Press et al.*, 1999]. This ordering system takes advantage of the fact that the river segment under consideration generally flows toward the southeast, to save computation time in the main algorithm.

Meanders are, for our purposes, defined as places where the river flows in a direction opposite the prevailing flow direction. For example, within Owens Valley, in general the Owens River flows southeast, except for two meanders, where it flows northeast briefly before turning back to the southeast. In terms of indices, the j-index needs to be ordered opposite the prevailing j order trend, in order to allow flow continuity without major reordering within the main algorithm.

A restriction of the approach used here is the assumption of a prevailing direction of river flow, so that large-scale meanders are taken to be the exception, not the rule. On the other hand, smaller scale meanders are implicitly included in the flow direction algorithm as long as the river is represented on the local model grid by at least two points in the cross-wise direction (the direction approximately perpendicular to the main flow direction). Thus, even within a large scale meander, there can be small scale meanders or bends (see Figure 4.5).

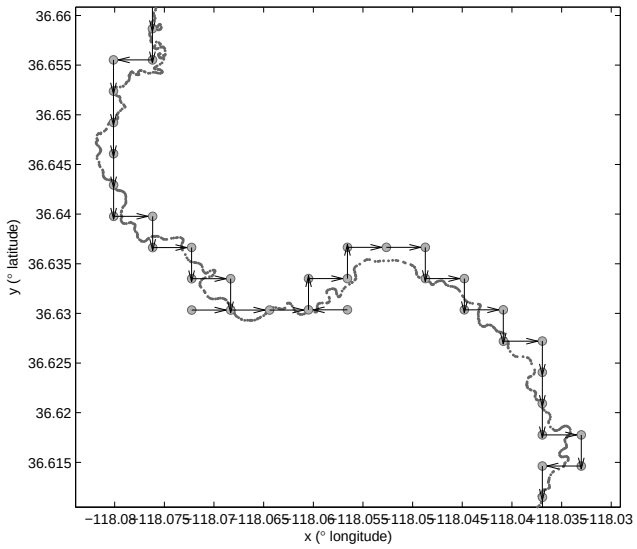


Figure 4.5. Model representation of river (large dots, 350m resolution), compared to NHD flowline data (small dots, fine resolution). Black flow direction arrows show continuous river flow on model grid through large meander.

### 4.4.2 Flow direction enforcement algorithm

The goal of the main program is to determine a continuous flow path by ordering the points (corresponding to grid cells) along the river so that each point is followed by a grid cell neighbor (see Figure 4.2). A grid cell neighbor is defined as any of the four grid cells that share a side in x or y. The four neighbors of point (i,j) are therefore: (i,j+1), (i,j-1), (i+1,j), and (i-1,j). Thus, the river will be represented by a list of points, each with an upstream and a downstream neighbor, and a slope with direction pointing toward its downstream neighbor, as shown in Figure 4.5.

To this end, the algorithm marches through the cells along the river, moving downstream according to the list provided by the preprocessing program, and determines if the next cell on the list is a neighbor of the current cell (i.e. in one of the four adjacent positions). If the next cell in the list is not a neighbor, then there are two options: 1) find a cell in the list which is a neighbor of the current cell, or 2) label the current cell a "dead end" and find a way to route flow past it.

Finding a neighbor cell, if it exists, may be quite easy, given the sorting work done in the preprocessing program. One common configuration simply requires switching the indices of the next two cells so that both the current cell and the next cell are guaranteed to have a downstream neighbor (see Figure 4.6).

Other cases are more complicated and must be dealt with individually. Some examples of these are shown in figures 4.7, 4.8, and 4.9. Figure 4.8 shows a case where no downstream neighbor existed for certain points, so flow is routed past them, effectively making them small tributaries to the main flow path. Though these may not represent real tributaries, this is the only way to represent the general placement of the river path on coarse-resolution model grids. The general flow direction of the river is still accurate, and flow is still continuous along the main path, which is the goal of this algorithm. Convergent flow shown in the meander at the center of Figure 4.5 (latitude 36.63) is another example of a special case.

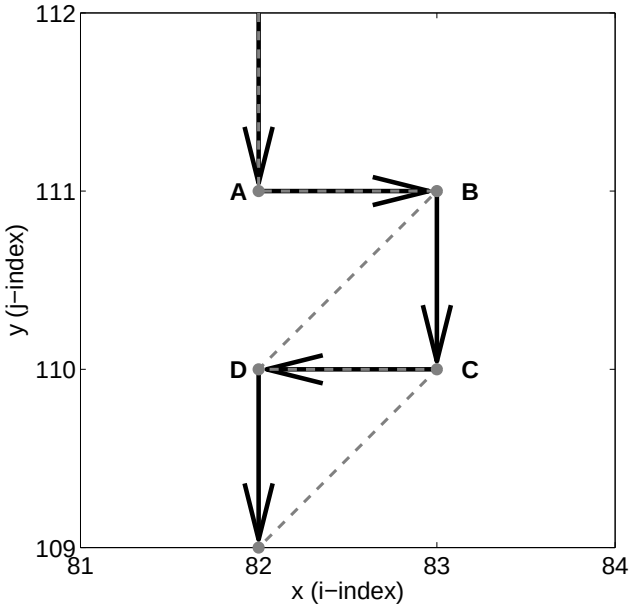


Figure 4.6. Dashed line shows discontinuity in sorted points from preprocessing program. Arrows show continuous flow after simple switch of points C and D in main algorithm.

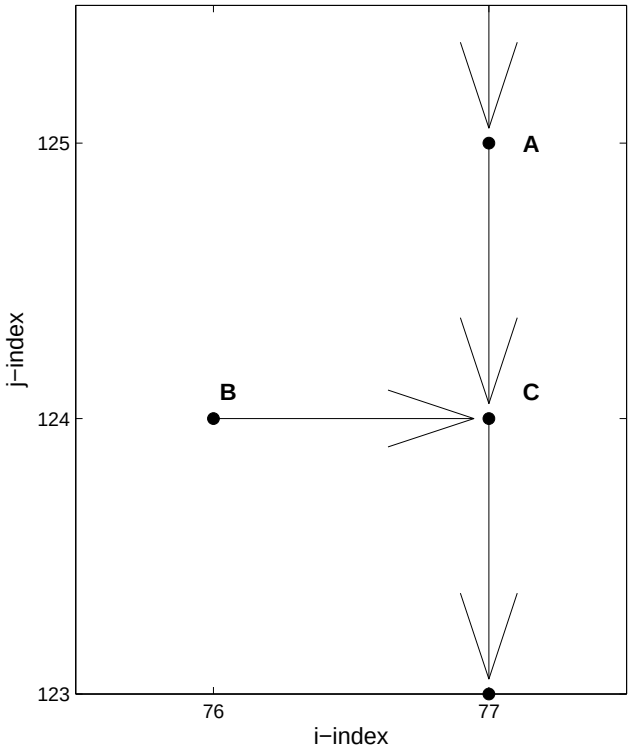


Figure 4.7. Flow is routed past a small "tributary". Order is still A, B, C, but now the flow direction for point A is calculated with respect to point C instead of point B. (Since point B was a dead end, a simple switch was not possible to preserve continuity.)

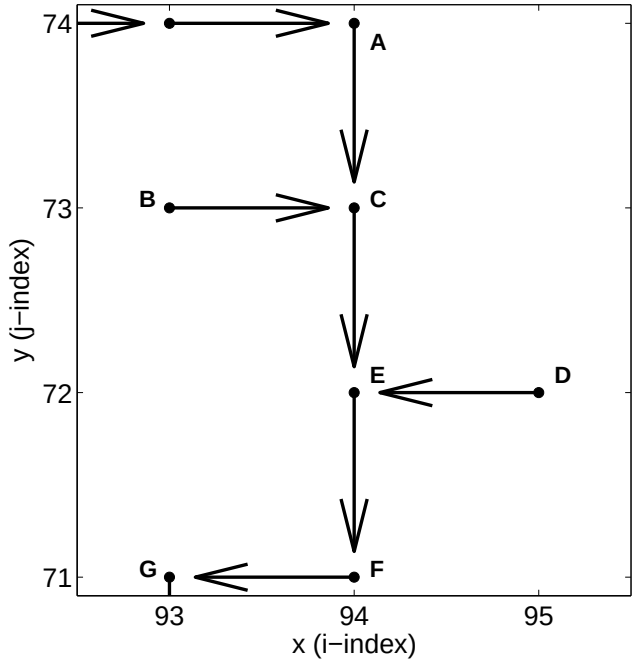


Figure 4.8. Flow is routed past multiple small "tributaries". Points D and E, and F and G have been switched (from initial i-increasing order), and flow directions have been calculated from A to C, C to E, and E to F.

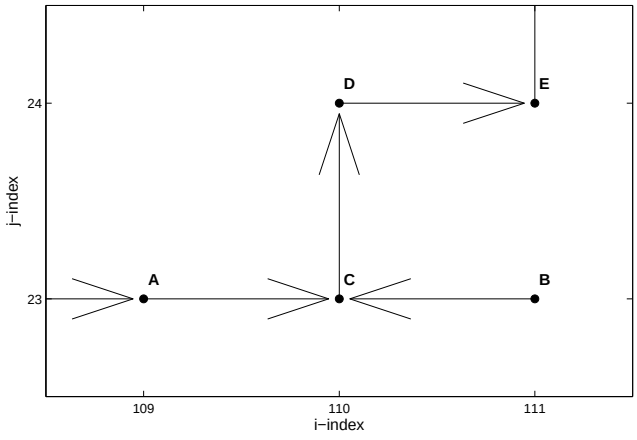


Figure 4.9. Convergent flow routed past a "tributary". Points B and C have been switched (from initial i-increasing order). Flow direction for point A is calculated with respect to point B, even though point C lies between them. This example is at the beginning of a meander, so point D has already been placed after point C by the preprocessing algorithm.

Slopes along the river can either be assigned or calculated, depending on the application. Calculated river slopes reflect the slope in the direction that water will flow, based on elevations assigned to each i,j location according to a steady linear drop in elevation from cell to cell all along the river path. Assigned slopes can be implemented by setting slope magnitudes to 1, and then multiplying the slope array (or sections of it) by the desired slope magnitude. Certain sub-grid scale channel geometries may be represented in this way.

Output from the main algorithm are x and y slopes, as well as corresponding i,j locations and elevations of the stream reach on the model grid. Using this output, the flow path may be integrated into an existing DEM, so that a flat plain such as that in Owens Valley shown in Figure 4.4(a) can, for example, be given a gentle slope down to the riverbed as shown in 4.4(b).

It is recommended that the i,j indices output from the preprocessing program be plotted and inspected to ensure continuity. If major gaps between points exist, there is a tolerance that can be adjusted so that more points on the model grid will be used to represent the river. In our case, there are a few places were the Owens River runs exactly diagonal to the model grid, so that even though the preprocessing program works properly under the specified tolerance, a four-direction flow scheme would not allow continous one-dimensional flow along the river, (though an eight-direction scheme would). In these cases, an additional point should be added so that river flow can be continuous within a four-direction flow scheme.

Direction of flow at the outlet, (the only point without a downstream neighbor), is assigned by inspection; in our case, knowing that the average flow direction is approximately to the southeast, flow is directed to the south at the outlet. Direction of flow at the inlet is determined by the second point in the list. Note however, that the exact configuration of points near the inlet may require a modified ordering of points at the inlet. That is, the first point in the list may not be the inlet; this should be verifed and manually corrected if necessary. Inlet and outlet conditions must be checked and corrected manually because the ordering logic used here requires both upstream and downstream information to ensure flow coninuity.

## 4.5 Rain-recession slope tests

### 4.5.1 Model set-up

The algorithm output was tested using the overland flow solver in ParFlow, a groundwater model with integrated surface flow. ParFlow solves the Richards equation in three dimensions using second order cell-centered finite differences in space and an implicit backward Euler scheme in time. The subsurface is coupled to the surface via an overland flow boundary condition consisting of the kinematic wave equation applied at the land surface [*Kollet and Maxwell*, 2006]. The kinematic wave equation formulation of the overland flow solver relies only on the slope of the cell and the friction slope (calculated by Manning's equation), to determine how much water to move to the downslope neighbor. Thus a cell with a very small or zero slope is virtually prevented from releasing water. A second order finite volume approach and an implicit backward Euler scheme are used for spatial and temporal discretization, respectively, of the kinematic wave equation. The coupled equations are solved simultaneously using a Newton-Krylov method with multigrid preconditioning of the linear system. For details, see: *Ashby and Falgout* [1996]; *Jones and Woodward* [2001]; *Kollet and Maxwell* [2006].

For these tests, the time spent in the groundwater solver is minimized by setting the hydraulic conductivity in the subsurface to a very small value, so that the focus is on the overland flow solution. Results of a simple steady rain and recession case are presented. Outlined here is the procedure for integrating the river into the original DEM, to produce a channel with continuous slopes on the floor of Owens Valley. as well.

At this point we could simply replace the original slopes along the river's path (based on the original DEM) with those calculated by the algorithm. However in the case of Owens Valley, this would not solve the problem of the flat flood plain, except on the narrow line of cells along the river channel. Since we have already assigned terrain heights along the river to correspond to the continuous slopes along the river, it makes sense to take advantage of this and fully integrate the river into the DEM so that the (originally flat) flood plain has a gentle slope down to the river. While this procedure does modify the original DEM significantly, it is still considered necessary in order to avoid sinks arising from a flat valley floor.

The river is integrated into the existing DEM (350 m resolution) first by lowering inlet and outlet terrain heights by a few meters and assigning a linear drop between them along the river. Gentle slopes are given to the flat areas near the river with similar results to those of *Hellweger* [1997], though we use additional averaging in areas that would fall outside of Hellweger's "buffer" zone, as shown in Figure 4.4(b).

Two idealized test cases are presented here that are specifically designed to stress the contiguous routing of this approach. These cases treat the subsurface as an impermeable media to ensure that overland flow routing occurs in every cell of the domain during a simple rain-recession simulation. While these cases ignore coupled subsurface processes, they are a rapid way to check the fidelity of the approach presented here. The first case uses slopes from the original DEM, derived from the USGS 3-arcsecond topography dataset. The second case uses a DEM with the river integrated, using the new algorithm, so that slopes are continuous along the river's path. The second case uses a modified version of the original DEM. (This modified version includes modifications for continuous slopes along the river, and gentle slopes down to the river.) These cases will be referred to hereafter as FLAT and RIV, respectively. FLAT is intended as an example of the problems that can arise in flat areas of a DEM, while RIV demonstrates how implementing the flow direction algorithm can successfully route flow along a river and out of an initially flat flood plain.

Horizontal grid spacing is 350 m with 144 points in both directions. Vertical grid spacing is 0.1 m with 10 points in z. A time step of 0.1 hr was used over a simulation period of 9 hours. A steady rain rate of 5 mm/h is imposed during the first hour only, so that the remaining 8 hours show drainage of the fallen precipitation.

### 4.5.2 Results

Figure 4.10 shows the pressure field (water depth over the land surface) at the end of the first hour, just after the rain ceases and at the end of the ninth hour as the domain continues to drain. While the maximum pressures exceed 2 m for the FLAT case at the end of the ninth hour, maximum pressures for the RIV case are less than 0.12 m at the same time. This order of magnitude difference in maximum values stems from the fact that the slopes for the FLAT case do not allow water to drain from the catchment. Rather, water drains down the slopes of the mountains to the edges of the flood plain, and pools there on certain cells. Cells showing elevated pressures corresponding to the depth of the water that has collected have very small slopes and thus act as virtual sinks. The

kinematic wave equation formulation of the overland flow solver relies only on the slope of the cell and the friction slope (calculated by Manning's equation), to determine how much water to move to the downslope neighbor. Thus a cell with a very small slope will only allow a very small amount of water to drain to its neighboring downslope cell. If this cell with a very small slope has an upslope neighbor cell with a much larger slope, then the cell with the very small slope will act as a virtual sink, collecting the relatively large amount of flow draining to it from its upslope neighbor.

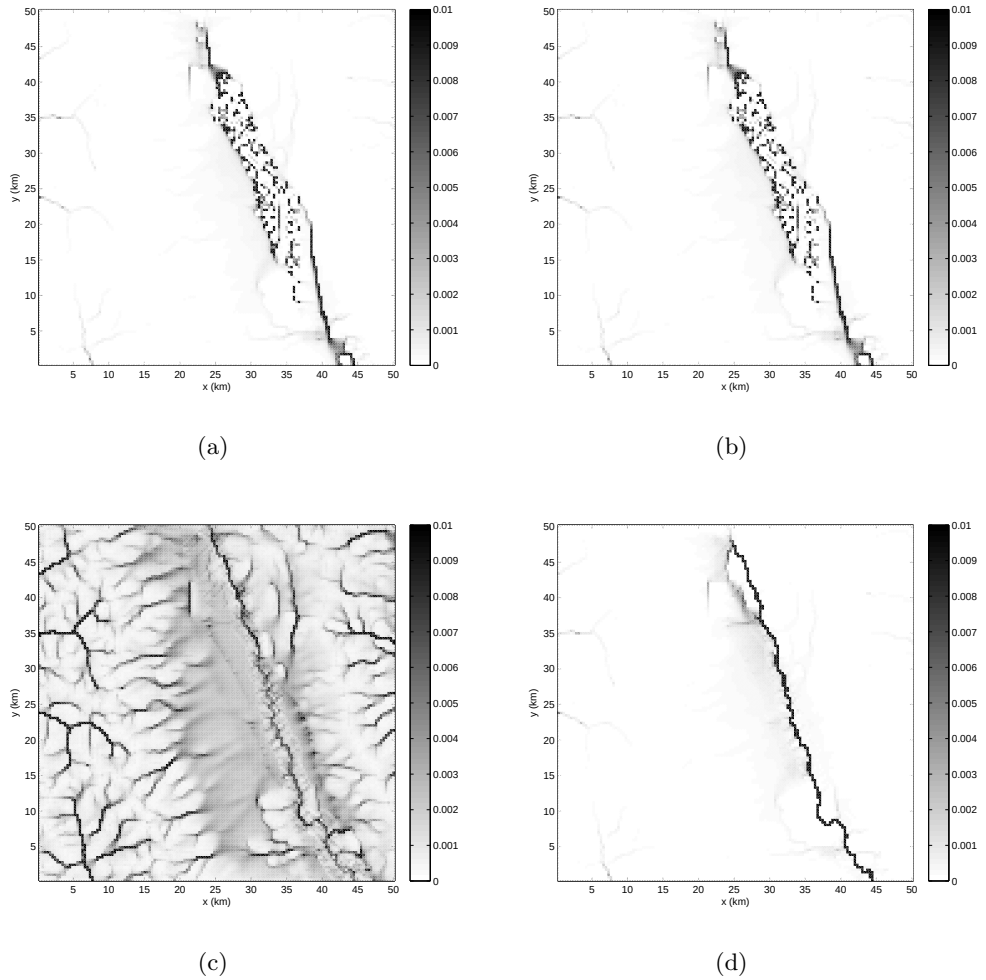


Figure 4.10. Pressure [m] over each grid cell for (a) FLAT at end of first hour (maximum pressure 0.1), (b) FLAT at end of ninth hour (maximum pressure 2), (c) RIV at end of first hour (maximum pressure 0.1), and (d) RIV at end of ninth hour (maximum pressure 0.12).

In contrast to the trapping of water in the flood plain of the FLAT case, the continuous slopes of the RIV case in the vicinity of and along the river allow flow down to and along the river's path, and finally out of the domain. Figure 4.11 shows the hydrographs for both the RIV and FLAT cases. Of course, only the RIV case has the river incorporated, so the hydrograph for the FLAT case is not a hydrograph in the traditional sense. It is simply a plot of the surface flow at the point corresponding to the Owens River outlet in the RIV case for the sake of comparison. Note that for the FLAT case, flow increases slightly after the rain ceases, then there is an inflection

point followed by recession during the remaining hours of the simulation. The RIV case, however, shows two distinct crests associated with the direct runoff from the valley, and the surrounding mountains, respectively.

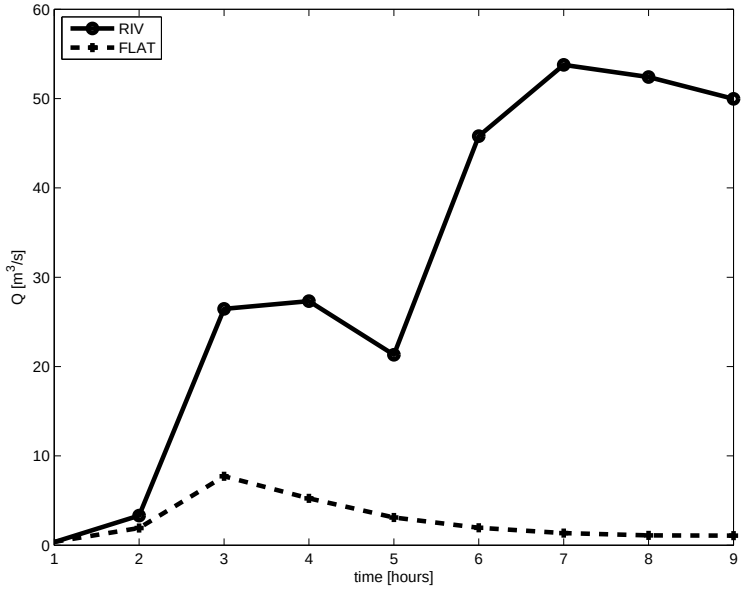


Figure 4.11. Comparison of hydrographs for RIV and FLAT cases, showing surface flow at the grid cell corresponding to the Owens River outlet. Note that the hydrograph for the FLAT case is not a hydrograph in the usual sense, since only the RIV case has the river incorporated.

The hydrograph for the RIV case shows two distinct crests associated with the direct runoff from the valley, and the surrounding mountains, respectively, which are lacking in the FLAT case, (see Figure 4.11).

Note that some models might use the diffusion wave approximation, and while this approach might mitigate some of the water accumulation on cells around the edges of the valley, it would still lack the sub-grid scale information necessary to route flow realistically with respect to the river. Other models use a two-scale approach, where a 1-D kinematic river is embedded into "river cells", however, this does not allow any interaction with neighboring cells or the subsurface.

The flow network from the rain-recession case is shown in Figure 4.12, superimposed on the terrain of the DEM from which the slope files were generated. This example illustrates how use of these new flowline mapping and flow direction enforcement algorithms can provide more realistic surface flow patterns in hydrologic modeling.

## 4.6 Concluding remarks

The preprocessing and flow direction enforcement algorithms presented here take NHD flowline data, map it to a model grid, then determine continuous flow directions according to an assigned elevation drop along a stream reach. Resulting stream slopes and elevations can be integrated into an existing DEM. While many other methods determine statistically valid flow networks directly from

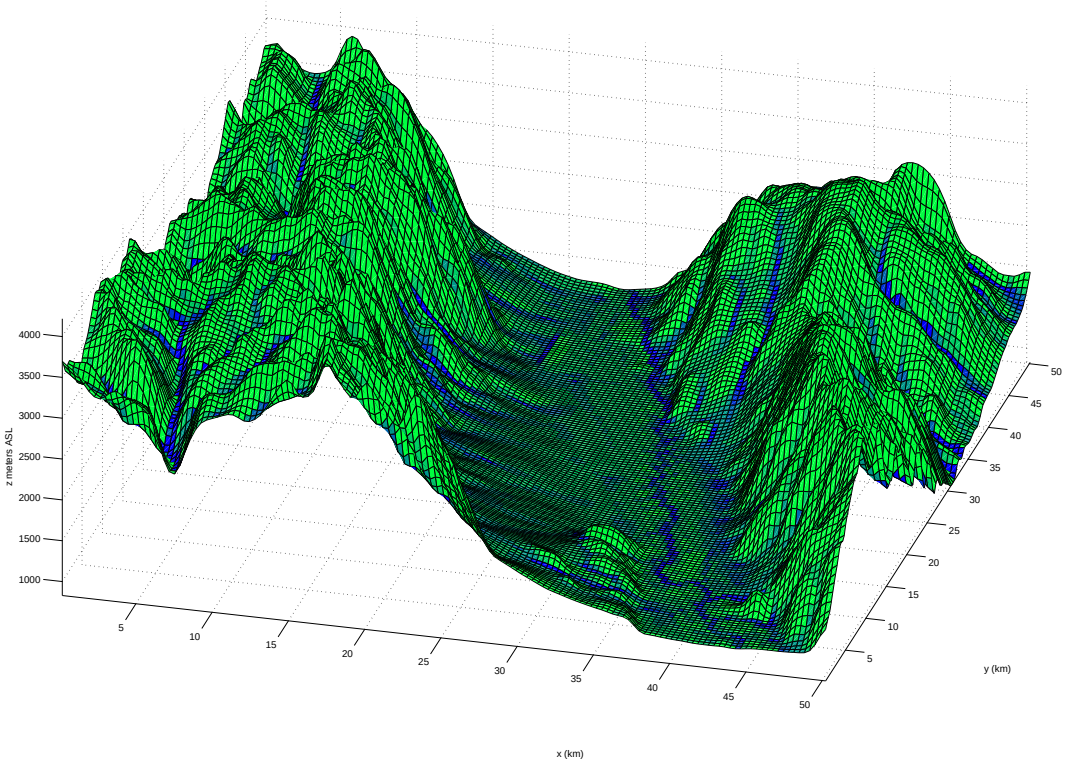


(a)

Figure 4.12. Stream network for a section of Owens Valley, as simulated using the flow routing algorithm along with ParFlow. Cells with water covering them are shown in blue. Green indicates dry cells.

a DEM, the algorithms presented here make use of high-resolution flowline data to deterministically represent the flow path of a stream reach on a relatively coarse DEM. This is done in the context of a scheme which allows flow into or out of any of the four grid cell faces according to conservation of mass, such that the surface flows can be fully coupled to the subsurface, as in ParFlow, the model we used to validate the results of the algorithm. NHD flowlines can be integrated into a DEM by some GIS software packages, however, such packages most often do not guarantee continuous slopes along flow paths, and so do not necessarily produce more realistic flow representations. We demonstrate the capabilities of the preprocessing and flow direction enforcement algorithms with a case study in Owens Valley, California using an integrated surface water-groundwater model, ParFlow. The original 350 m DEM does not resolve the Owens River, such that the river's flood plain appears essentially flat and causes spurious ponding. This problem is overcome by integrating the Owens River point data into the DEM, so that the originally flat flood plain is given a gentle slope down to the riverbed.

An idealized rain-recession case designed specifically to test flow connections at every cell demonstrates how more realistic surface flow patterns can be achieved through the use of the flowline mapping and flow direction enforcement algorithms. This unique approach is non-commercial, and relatively simple and easy to implement for a variety of applications. Future work might include extension of the current algorithms to branching networks, such that the processed domain can be used in full-scale coupled simulations.

# Chapter 5

# Field measurements of soil moisture and soil temperature during the Terrain-Induced Rotor Experiment (T-REX)

## 5.1 Introduction

This chapter presents field observations of soil moisture collected as part of the Terrain-Induced Rotor Experiment. These observations served as validation data for the hydrologic modeling presented in Chapter 3 as well as to inform simple adjustment of initial soil moisture fields used in the simulations of Chapter 6.

## 5.2 Background

Thirty soil moisture and temperature sensors were installed at 23 locations in Owens Valley, CA as part of the Terrain-Induced Rotor Experiment (T-REX) which took place in March and April, 2006. Site locations were chosen based on a number of considerations including accessibility, elevation, and representation of the surrounding area. Some sensors were co-located with other instruments including University of Utah HOBOs, University of Leeds flux towers, DRI towers, and Inyo County long-term soil moisture monitoring stations. Sites were chosen along several transects roughly perpendicular to the valley axis so that patterns in soil moisture could be identified (e.g.

higher or lower soil moisture on the valley side walls compared to the valley floor, or along-valley trends). T-REX observations were centered around Independence, so the main and central line of soil moisture sensors crossing the valley ran through Independence as well. All sensors were installed by the end of January, allowing at least a month for the sensors to settle into the soil before the start date of the T-REX field campaign on March 1, 2006.

Sites have been labeled S1 through S25 (S7 and S21 were never installed due to snow coverage.) Site locations in Owens Valley are shown in Fig. 5.1. Details such as latitude and longitude as well as site characteristics are given in the tables in Appendix A.

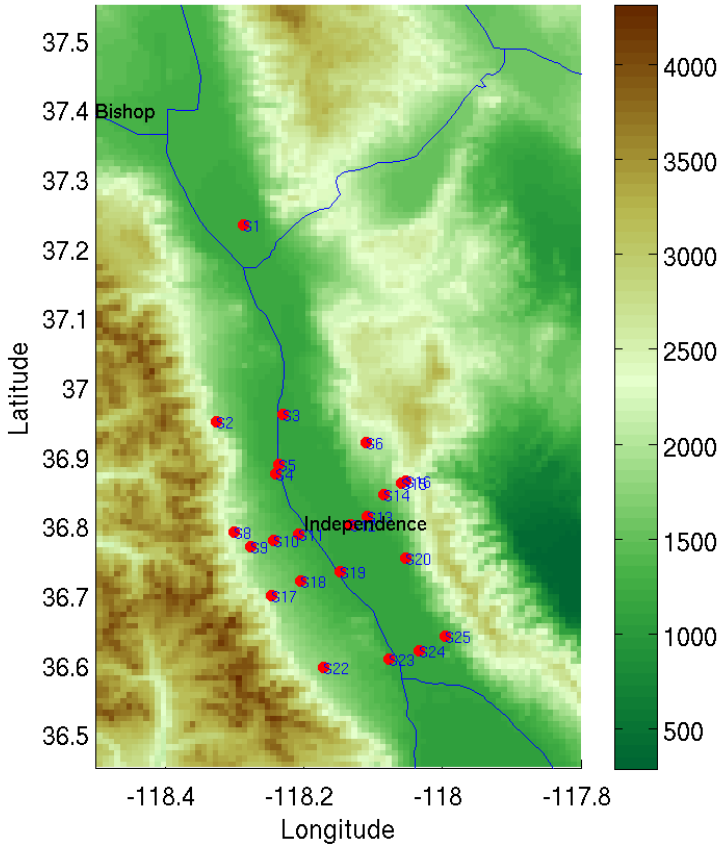


Figure 5.1. Soil moisture monitoring sites S1-S25 for T-REX in Owens Valley shown as red dots. Contour shading is terrain height in meters. Main roads are shown in black.

## 5.3 Data Files

There are two file formats available for download. Both formats contain the same four variables: date and time (mm/dd/yyyy 00:00:00), time in days (decimal days of 2006), soil moisture (VWC ($m^3/m^3$)), and soil temperature (°C). Two time variables are provided since each is convenient for

different applications (e.g. plotting may be easier using decimal days). The first format is a simple text file (with the extension: .txt). File names are constructed as follows, for example: if the site name is S2, and the logger number is 1332, then the file name is: "S2Logger1332.txt". There was one logger per sensor, so if multiple sensors were placed at a site, their data can be accessed based on their corresponding logger number. For example, at S8 there were three sensors whose data can be individually accessed in the files: S8Logger1334.txt, S8Logger1339.txt, S8Logger1440.txt. The second format is specifically for Matlab and has the extension: .mat. To load a "MAT-file" into Matlab, simply type, "load" followed by the file name (e.g. "S2Logger1332.mat"). The four variables will load into the Matlab workspace. The variable "dates" contains the dates, "timedays" contains time in days of 2006, "qsoilVWC" contains soil moisture in VWC, and "tsoilC" contains soil temperature in degrees Celsius.

## 5.4 Soil Moisture Sensors: Decagon ECH2O Capacitance Probes

To measure soil moisture, we used the ECH2O EC-20 soil moisture probes manufactured by Decagon Devices. The ECH2O probes are capacitance-type sensors that measure the dielectric constant or permittivity of the soil at the depth at which they are buried. Since we are mostly interested in the surface layer of soil as input for atmospheric models, sensors were buried just 5 cm below the surface at every site. At a few sites additional sensors were installed at 20-50 cm depth (see Appendix for details).

Raw data from the sensors were recorded on Decagon EM50 data loggers. This raw data then was calibrated to represent volumetric water content (VWC), a standard measure of soil moisture. Volumetric water content can be defined as:

$$VWC = \frac{\text{Volume of Water}}{\text{Total Sample Volume}} \tag{5.1}$$

For convenience, the above fraction is often multiplied by 100 to yield percent volumetric water content, or %VWC. We will use this convention throughout this readme file.

### 5.4.1 Soil Moisture and Temperature Probe Installation

A hole about twice as deep as the probe insertion depth (about 10 cm deep for the majority of probes) was dug at each site. The soil moisture probe was inserted into the wall of the hole approximately perpendicular to the temperature probe at the same depth in an effort to allow maximum contact of undisturbed soil along the length of the soil moisture probe. The hole was then filled in using the original soil, and allowing the wires from both probes to protrude from the ground to be plugged into the data logger. Photographs of installation can be seen in Appendix A.

## 5.5 Calibration of EC-20 Probes

### 5.5.1 Procedure and Calculation

Decagon Devices provides a standard mineral soil calibration curve to convert raw data from the EC-20 probes to VWC. This standard curve was found to be inadequate for many of our sites, probably due to high salinity of the soil in Owens Valley. The standard curve gave negative values of VWC for several sites; to eliminate this problem, we performed our own soil calibration for each site individually by taking gravimetric soil moisture measurements on two dates for each of the sites. Our calibration procedure and calculation is based on the procedure and calculation outlined in Decagon's Application Note entitled, "Calibrating ECH2O Soil Moisture Probes" available at www.decagon.com.

Gravimetric water content can be defined as:

$$GWC = \frac{\text{Mass of Water}}{\text{Mass of Dry Soil}} \tag{5.2}$$

To calculate the gravimetric water content of the soil, at least two sample cores of soil were taken from each site. To convert our gravimetric measurements to %VWC, it was necessary to calculate the bulk density. Bulk density can be defined as:

$$\rho_B = \frac{\text{Total Mass of Sample (Soil and Water)}}{\text{Total Volume of Sample (Soil and Water)}} \tag{5.3}$$

Our sample core volumes were known, and each total sample was weighed. (The sample core volume was extracted at an average depth of 5 cm.) Sub-samples were then weighed and placed in an oven to bake for at least 12 hours. The dry sub-samples were then removed from the oven and weighed again. The mass of water was deduced by:

$$\text{Mass of Water} = \text{Mass of Sub-sample before baking} - \text{Mass of Sub-sample after baking} \tag{5.4}$$

Knowing the GWC and bulk density, we calculated %VWC for each site by:

$$\%VWC = GWC\frac{\rho_B}{\rho_w} \times 100 \tag{5.5}$$

where $\rho_w$ is the density of water.

Thus we calculated GWC for each site on two dates, and then converted to %VWC using bulk density. For each site, at least two values of %VWC were calculated, (based on the two core samples taken), and combined to get an average %VWC for the site. We then extracted raw probe values for the dates and times corresponding to when the soil samples were taken. (So for example, the first set of soil samples for S2 were taken on March 31, 2006 at 8:30 AM and were found to have an average value of 15.2 %VWC with a raw probe reading of 703, giving us our first point on the graph relating raw probe values to %VWC. This was also done for the second set of soil samples, giving us our second point.) For each site, we then calculated a slope and intercept for the line between the two points which was considered to be the calibration "curve" for the site. (The raw data measured at the site is generally linearly proporational to VWC so this is a standard procedure.)

A few sites were lacking either a gravimetric measurement or a raw probe value at the time the soil sample was taken so that for these sites it was necessary to use a zero reading point to determine

the slope and intercept of a calibration curve (e.g. a raw probe reading of 600 was considered to correspond to 0 %VWC.)

In addition to taking soil samples for gravimetric measurements at each site, we also used a TDR (Time Domain Reflectometry) instrument to measure soil moisture. We used two different TDRs, the TRIME, provided by NCAR, and the Hydrosense, provided by Inyo County Water District. Due to time constraints, we were only able to use one of these instruments at each site. It is important to note that TDRs often need to be individually calibrated themselves. We found that the TDR usually provided an estimate of soil moisture that was different from what we found using the gravimetric measurement method. In some cases the calibration based on the TDR was very close to the gravimetric calibration, but in other cases the calibration was not successful. The TDR calibration did however, often fall within the range of calibrations provided by Decagon Devices.

### 5.5.2 Temperature Effects

Freezing of the soil surrounding the probes causes spurious readings (extremely low readings) because the water present in the soil freezes and the probes are unable to measure frozen water. So if the temperature probe indicated that the soil temperature was below zero degrees Celcius, the soil moisture probe readings were neglected.

Decagon Devices indicated that the EC-20 probes may be sensitive to extreme heat, or strong temperature fluctuations ($\sim 30°$) over the course of a day. This kind of temperature dependence has not been removed from the dataset in order to avoid averaging and perhaps distorting or smearing out other important patterns in the data. There is some natural fluctuation in soil moisture over the course of a day, so it is difficult to remove only the fluctuation due to the probe's sensitivity to temperature. (A temperature correction formula is provided by Decagon for standard ECH2O calibrations which are performed in a laboratory under controlled temperature conditions. Thus the temperature correction could not be used with our individual gravimetric calibrations based on field data.)

### 5.5.3 Error Estimates and Figures

Decagon estimates that the absolute error for the EC-20 using the standard mineral or sandy loam curve is + or - 4 %VWC. To get a rough estimate of the error in our gravimetric calibration, we looked at the differences between results for the two or more sub-samples weighed and baked for each site at two dates. Results for each of these sub-samples were then averaged over the number of sub-samples for each site. The difference between the %VWC calculated for each sub-sample at a given site varied from site to site from 0.06 %VWC for S1 to as much as 15.59 %VWC for S5 (which yielded an unsuccessful gravimetric calibration). Most of the sites fell in the range from 0.06 %VWC to about 5 %VWC difference between sub-sample results. Based on this observation, we place the error in our gravimetric calibration at approximately + or - 5 %VWC for the successful calibrations.

The following figures show results for four different calibration curves applied to data from the EC-20 soil moisture capacitace probe. Black markers indicate gravimetric measurements. Blue is the gravimetric calibration, green is the TDR (Time Domain Reflectometry) calibration, red is Decagon's standard mineral calibration (from the manual), and pink is Decagon's sandy loam

calibration. (For one site, S3 we used an organic soil calibration provided by Decagon, rather than the Decagon's sandy loam calibration. This is indicated on the figure for S3.) Soil types for each site were determined via a simple "touch test" following the procedure set forth by East Dakota Water Development District (available online at: www.bigsiouxwaterfestival.org/tp28.htm). Results are given in a table in Appendix A.

For most of the sites, the gravimetric calibration was used to calibrate the soil moisture data available from the T-REX data archive website (http://data.eol.ucar.edu/master_list/?project=T-REX). The calibration used for each sensor is indicated on the figures by a an asterisk in the legend. In two cases (S25 and S6), the gravimetric calibration yielded a slope opposite that of Decagon's standard mineral and sandy loam calibrations. This caused rain events to appear as periods of extreme drying instead of wetting, indicating that our gravimetric calibration was flawed for these sites. For S25, Decagon's sandy loam calibration was chosen because the mineral calibration produced negative soil moisture values (%VWC). For S6, Decagon's standard mineral calibration was chosen because it most closely approximated the range of the gravimetric measurements taken at the site. The soil at S6 was determined to be sandy clay by touch test, so it is debatable whether the sandy loam or standard mineral calibration is better for this site.

Note that days 30 through 125 represent the T-REX field campaign dates, though all days (if available) starting January 1, 2006 are shown in the plots. Temperature plots for each sensor are shown on the same page below each soil moisture plot.

This chapter includes figures showing transects for the week during which EOP2 and IOP6 of T-REX took place, as well as snapshots of interpolated data for a rain event (discussed in the following section). Appendix A includes plots of calibrated soil moisture data from selected sites and sensors. Shown along with the data in the Appendix A are photographs of select sites at installation and/or maintenance, depending on the site, in January of 2006. The photographs show the soil, vegetation and local topography at the site, as well as demonstrate our methods of installation.

## 5.6 Correlation to meteorological conditions

Figure 5.2 shows observations of cumulative precipitation, relative humidity, air temperature, wind direction and wind speed at a location near Bishop, on the floor of Owens Valley, for the 2005-2006 water year. Figure 5.3 shows the same meteorological data, but for only the days surrounding March and April, 2006. (Precipitation is shown in this figure, rather than cumulative precipitation.)

The rain event at the end of February produced about 5 mm of cumulative precipitation, and this is visible in the plots of most of the soil moisture sensors. Interpolated plots of soil moisture and soil temperature, representing data from all 23 sites in Owens Valley on February 27-28, 2006 are shown in Figures 5.4 and 5.5, respectively for midnight and noon. Though soil moisture at most sites increased significantly from the 27th to the 28th, soil temperature also increased. This could be due to clouds present on the 27th, as indicated by observations of precipitation and 100% relative humidity, but no precipitation on the 28th and lower relative humidity. The delay in soil moisture increase at the center of the valley especially may be due to delay in run-off accumulation (at S3 in particular), as well as effects of the crust that develops in arid regions and must be infiltrated before deeper infiltration can occur during and after a rain event.

Figures 5.6 and 5.7 show cross- and along-valley transects of soil moisture and soil temperature respectively for the last week of March, 2006 during which both observation periods discussed in this dissertation, IOP6 and EOP2, took place. S23 and S14 were left out of their respective transects due to lack of data during the time period shown. Noteworthy is the increase in soil moisture visible at higher elevations, on the western slopes of the valley (see Figures 5.6(a) and 5.7(a)), especially on March 29th, but also in the days following. This is probably due to an increase in air temperature on that day, and a corresponding increase in snowmelt. (The end of the week was significantly warmer than the beginning, see Figure 5.3.) Soil temperature, (shown in Figures 5.6(b) and 5.7(b)) at higher elevations on those days was lower than in the valley, probably due to enhanced evaporation effects under increased soil moisture conditions as well as lower air temperatures at elevation.

In general the observations of soil moisture and soil temperature seem to follow observed trends in the meteorological observations. The soil moisture observations presented here were used to validate results of coupled hydrologic modeling discussed in Chapter 3 as well as to inform the choice of surface soil moisture initialization for the simulations of atmospheric boundary layer flow using ARPS, discussed in Chapter 6.

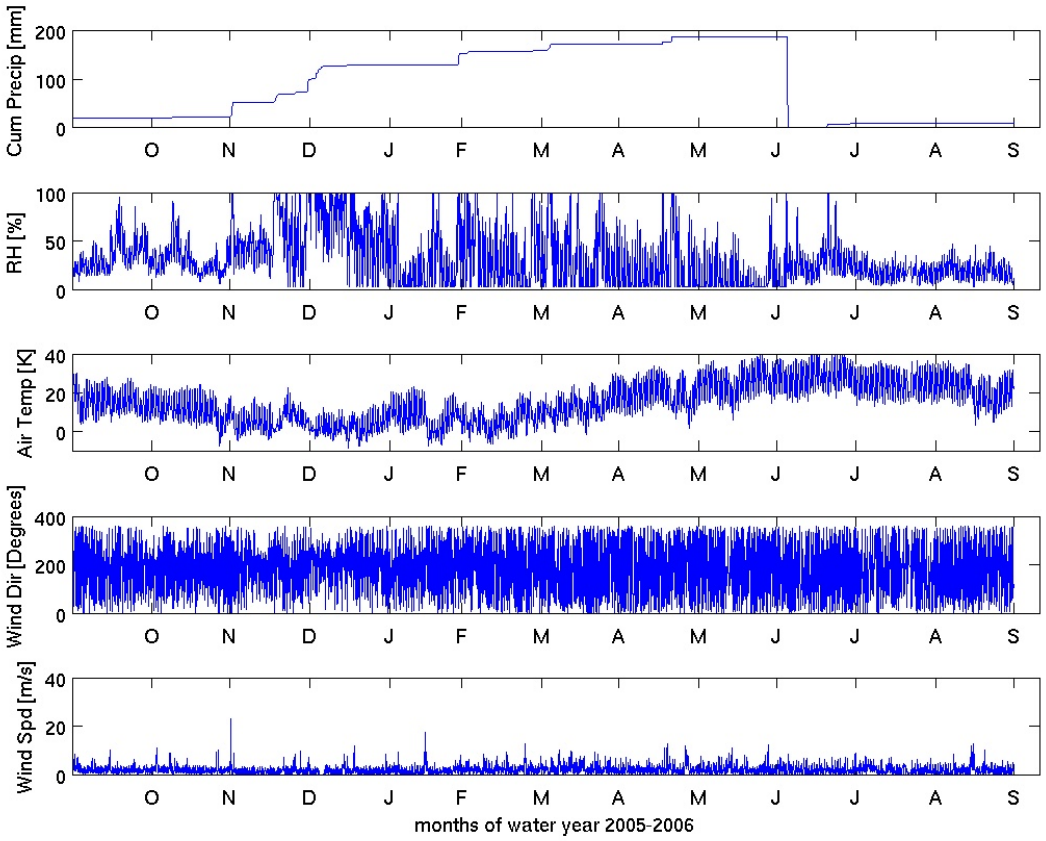


Figure 5.2. Observations of cumulative precipitation (mm), relative humidity (%), air temperature (C), wind direction (degrees) and wind speed (m/s) for the 2005-2006 water year at the center of Owens Valley near Bishop, (obtained through the California Data Exchange Center, CDEC).

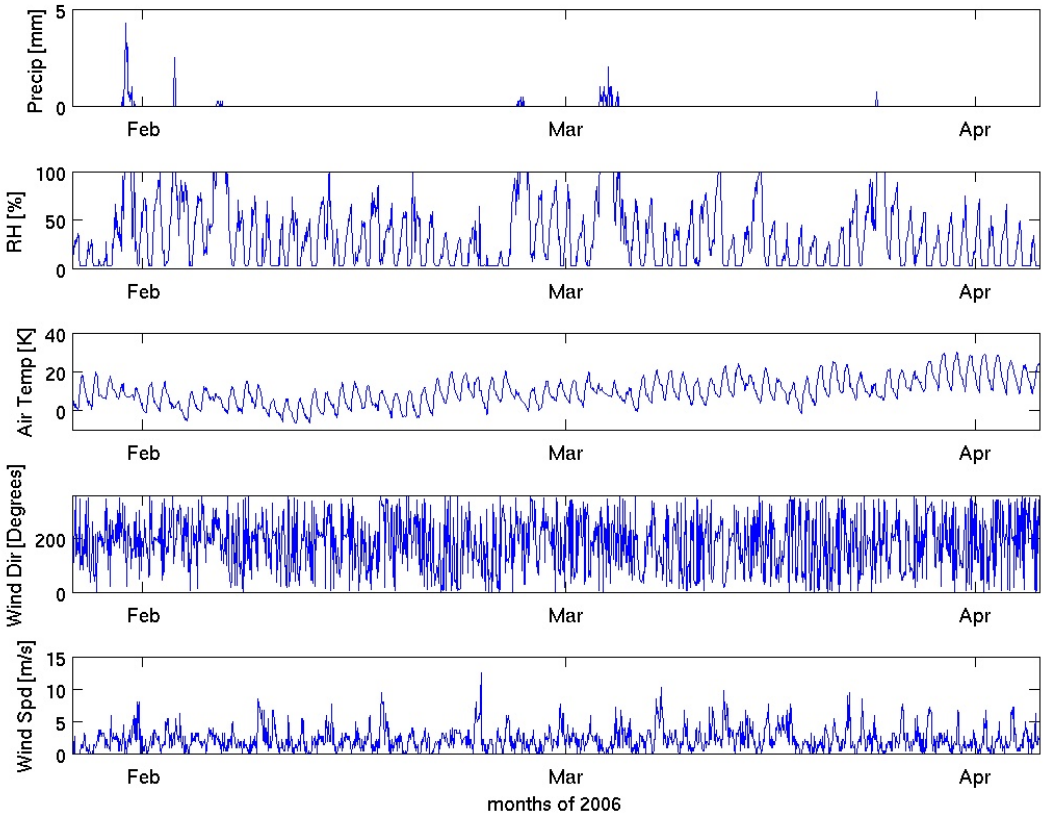


Figure 5.3. Observations of cumulative precipitation (mm), relative humidity (%), air temperature (C), wind direction (degrees) and wind speed (m/s) for March and April of 2006 at the center of Owens Valley near Bishop, (obtained through the California Data Exchange Center, CDEC). The rain event at the end of February is shown in 5.4 and 5.5.

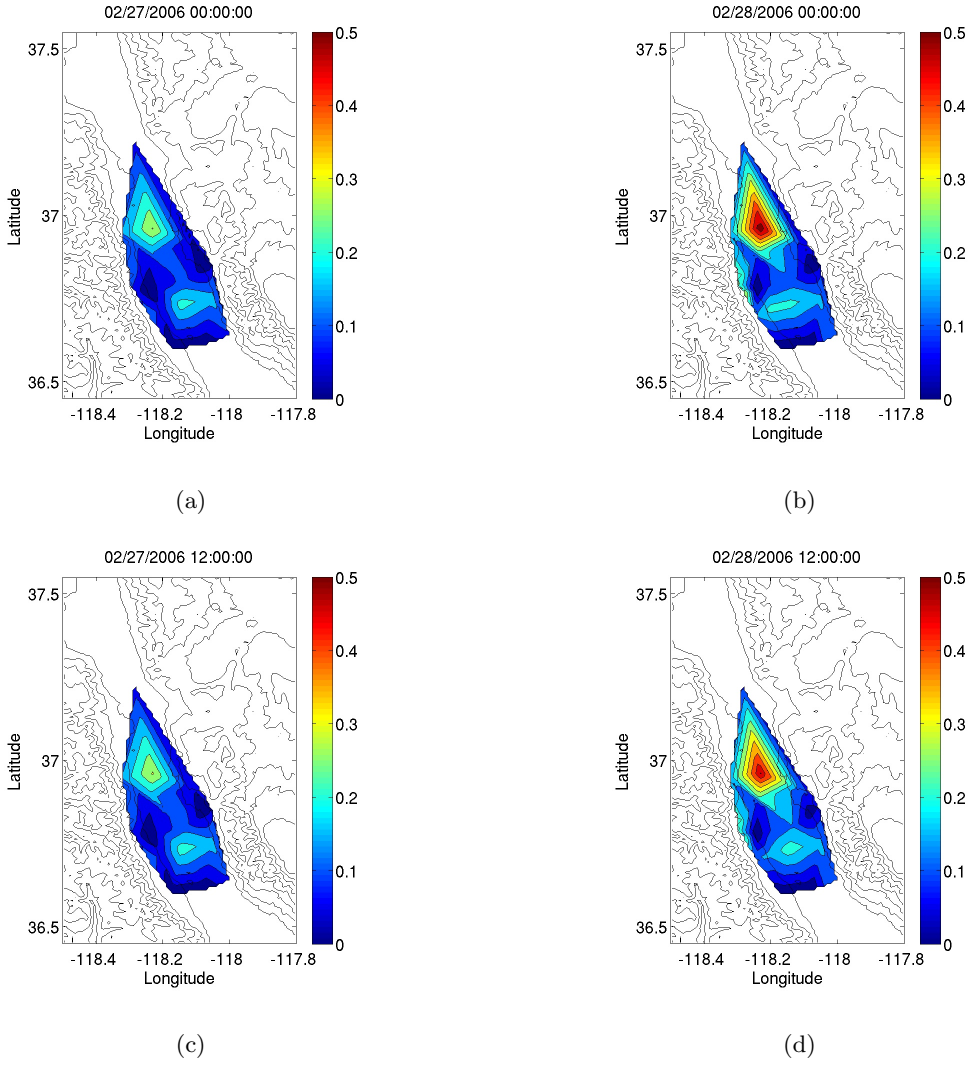


(a) (b)

(c) (d)

Figure 5.4. Soil moisture at midnight (a,b) and noon (c,d) of February 27-28, 2006, before and after a rain event.

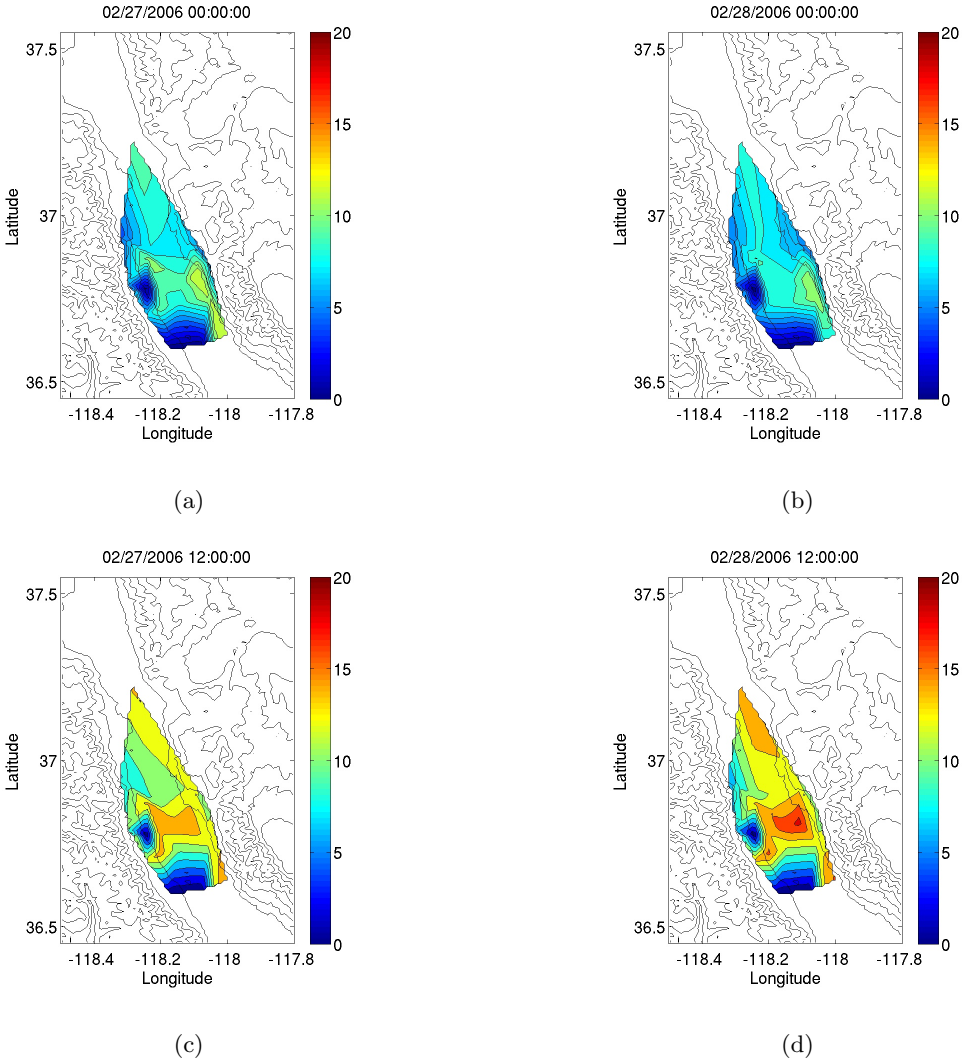


Figure 5.5. Soil temperature at midnight (a,b) and noon (c,d) of February 27-28, 2006, before and after a rain event.

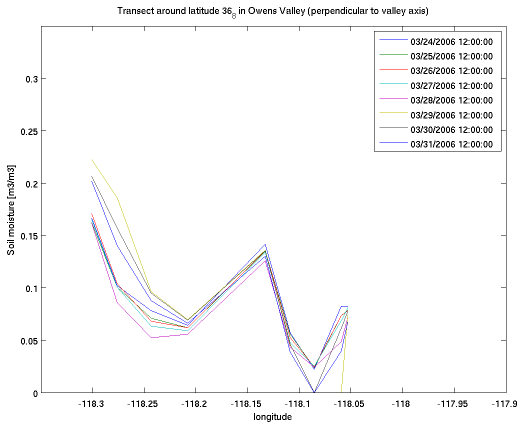


(a)

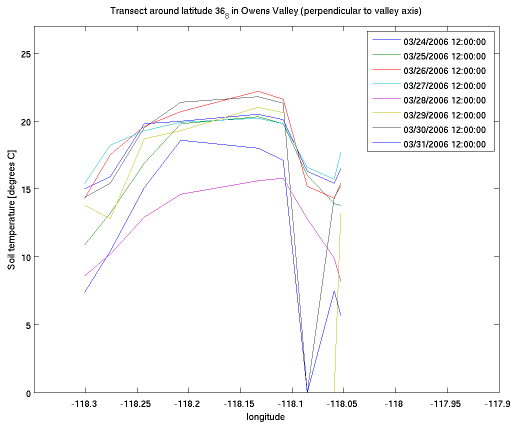


(b)

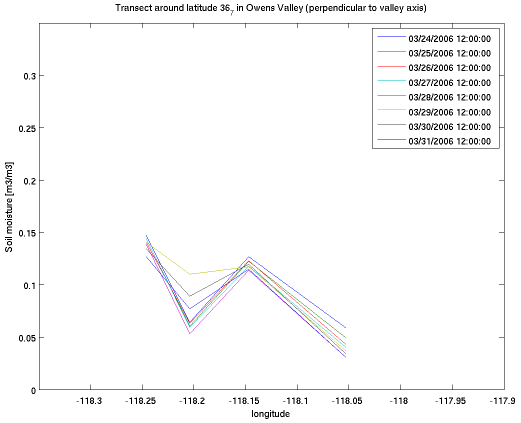


(c)

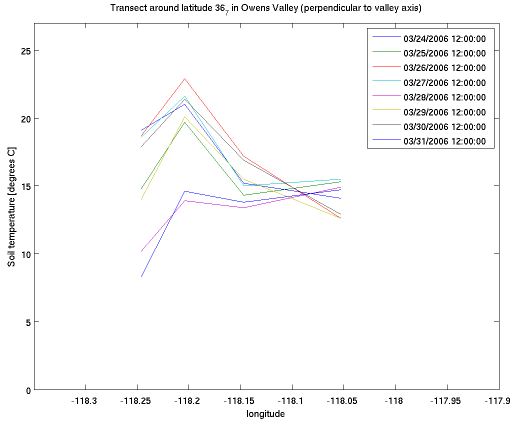


(d)

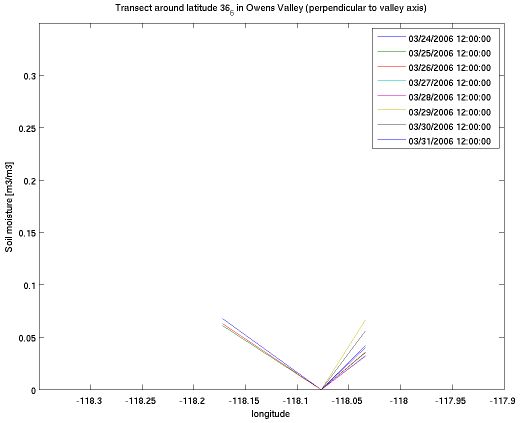


(e)

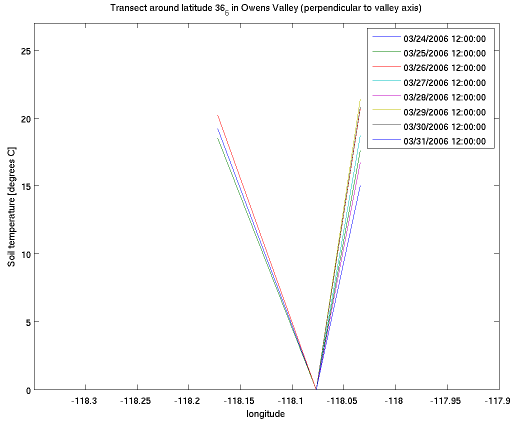


(f)

Figure 5.6. (a,b) Northern cross-valley (west-east) transect, around 36.8 degrees latitude. (c,d) Middle cross-valley transect, around 36.7 degrees latitude. (e,f) Southern cross-valley transect, around 36.6 degrees latitude.

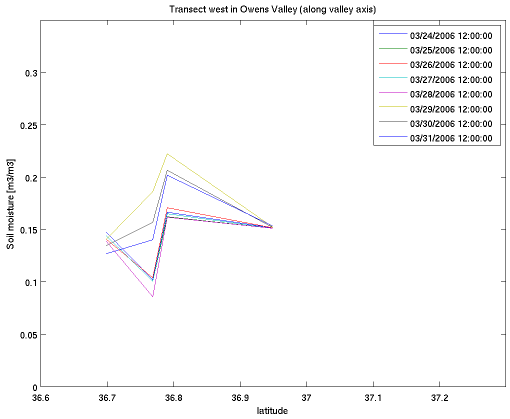


(a)

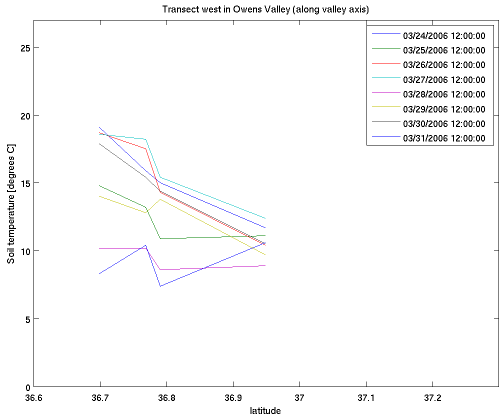


(b)

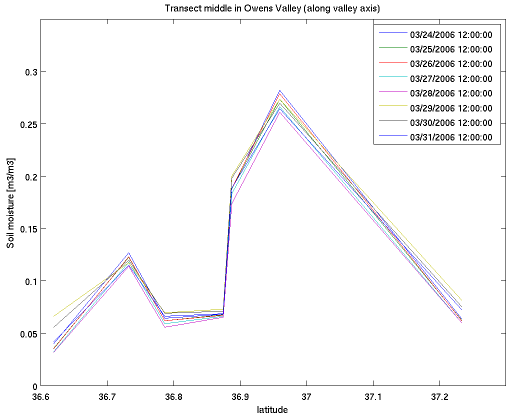


(c)

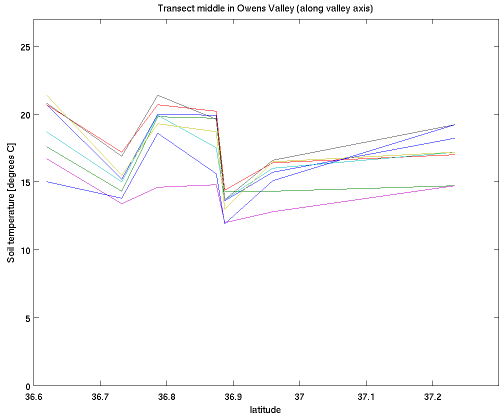


(d)

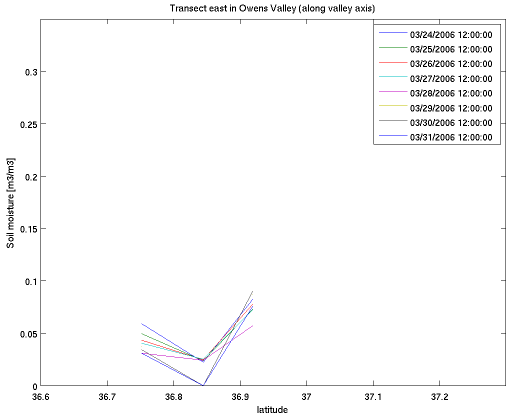


(e)

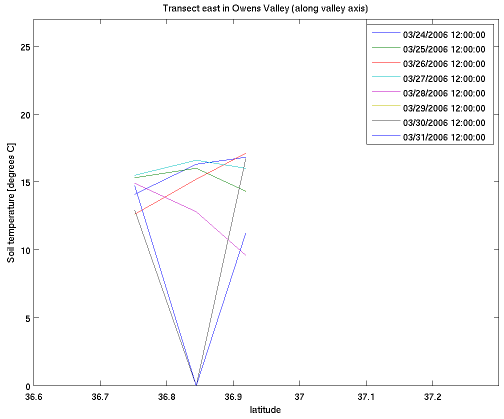


(f)

Figure 5.7. (a,b) Western along-valley (north-south) transect. (c,d) Middle along-vallet transect. (e,f) Eastern along-valley transect.

# Chapter 6

# Simulations of boundary layer flow over complex terrain: effects of providing improved surface conditions

## 6.1 Introduction

This chapter draws from the topics discussed in all previous chapters. The sensitivity tests described in Chapter 2 provide strong evidence of the need for more accurate initial soil moisture for high-resolution simulations of atmospheric boundary layer flow in complex terrain. Coupled hydrologic modeling discussed in Chapters 3 and 4 provides high-resolution soil moisture data validated by the field measurements presented in Chapter 5. Presented here are simulations of two observing periods from the Terrain-Induced Rotor Experiment (T-REX) performed with four different soil moisture and snow cover initializations. Results of these simulations are compared to observations from T-REX.

## 6.2 Background

Mountainous topography and corresponding heterogeneous land-surface characteristics and conditions can strongly affect flow in the atmospheric boundary layer. Soil moisture in particular affects the atmospheric boundary layer through partitioning of the surface heat fluxes. For valleys, a general picture of the expected behavior of wind systems during calm conditions has emerged, classifying winds as up-slope and up-valley during the day, and down-slope and down-valley at night, with the breakup of a nocturnal inversion layer during the day leading to a well-mixed valley atmosphere [*Whiteman*, 2000; *Rampanelli et al.*, 2004]. These flow transitions and the thermal

structure of the valley atmosphere are affected by irregularities in valley geometry, synoptic flow forcing, and land-cover heterogeneities.

Soil moisture initialization is particularly important for numerical simulation of thermally-forced flows because of its effect on surface heat fluxes [see e.g. *Ookouchi et al.*, 1984; *Patton et al.*, 2005; *Banta and Gannon*, 1995]. Previous work in the Riviera Valley in the Swiss Alps showed that soil moisture initialization was a very sensitive parameter for correct prediction of valley wind transitions [*Chow et al.*, 2006b]. The onset of up-valley winds in the Riviera was delayed by 3-4 hours in initial simulations compared to observations. Initializing with soil moisture fields from a hydrologic model (WaSiM-ETH) reduced the delay to 1-2 hours, illustrating the importance of land-surface characteristics and the need for accurate specification of these bottom boundary conditions [*Chow et al.*, 2006b].

Most land-surface models used in meso-scale simulations are initialized using data from external large-scale forcing data. Errors in these initial fields are exacerbated in complex terrain, where terrain features are smoothed by the coarse resolution. The 12 km resolution commonly used by regional models, for example, is not able to resolve steep and narrow mountain valleys, often causing specification of incompatible surface data due to elevation differences. As suggested by *Chow et al.* [2006b], it may therefore be necessary to provide higher-resolution surface initial conditions as the atmospheric model resolution is increased.

Studies focusing on land-surface heterogeneity effects in complex terrain have traditionally been done for quiescent conditions because it is often assumed that surface conditions do not significantly affect flow under strong synoptic forcing. While this hypothesis is generally true over flat terrain, it is does not necessarily hold for complex terrain. In Chapter 2 of this dissertation, it was shown that simulations of atmosperic boundary layer flow over the complex terrain of Owens Valley, California are sensitive to soil moisture initialization under both weak and strong meteorological forcings. It is hypothesized that under strong forcing, dynamically-forced circulations within the valley allow air to be in contact with the surface long enough to be heated or cooled by it, thus allowing surface conditions to significantly affect the flow. In Owens Valley, such dynamically-forced circulations occur frequently as atmospheric rotor events, and are somewhat analogous to a hydraulic jump in water [*Kuettner*, 1959], only surface heating plays a role in the atmospheric case. *Doyle and Durran* [2002] investigated effects of surface heating on the lee side of a bell-shaped mountain for two-dimensional rotor flow and found that the strength of the reversed flow decreased by more than 50% and the depth of the circulation nearly doubled compared to the simulations with no heating, even with very weak surface heat flux (50 W/m$^2$). *Smith and Skyllingstad* [2009] found that surface heating and cooling significantly affected rotor flow over a two-dimensional bell-shaped ridge in a three-dimensional domain. *Jiang and Doyle* [2008] found strong diurnal variation in rotor flow with diurnal changes in surface fluxes in Owens Valley during the Sierra Rotors Project.

This chapter investigates the effects of soil moisture (and consequently temperature) on simulations of the atmospheric boundary layer in Owens Valley, CA under both quiescent and strong forcing conditions. In this chapter, there is an emphasis on methods for more accurate representation of conditions at the land-surface and comparisons of simulation results to field observations. This focus on field observation comparisons distinguishes this chapter from Chapter 2 of this dissertation, which focused only on determining the extent to which extreme soil moisture conditions could potentially affect flow in the atmospheric boundary layer.

Owens Valley was the site of the Terrain-Induced Rotor Experiment (T-REX) which took place in March and April of 2006 [*Grubišić and Kuettner*, 2004]. Simulations are performed using the

Advanced Regional Prediction System (ARPS) [*Xue et al.*, 2000, 2001] for Enhanced Observational Period 2 (EOP2) and Intensive Observational Period 6 (IOP6) of T-REX. EOP2 focused on boundary layer development under quiescent conditions, while IOP6 focused on rotor flow under strong forcing. EOP2 began March 29, 2006 at 0300pm Pacific Standard Time (PST) (2300 UTC) and ended at 1200pm PST (2000 UTC) the following day. IOP6 began at 0900 PST on March 24, 2006 and ended at 2100 PST the following day. The atmospheric conditions and flow structure of these cases are discussed in more detail in Chapter 2 of this dissertation.

Soil moisture and temperature data were collected at 23 sites by the author during T-REX to more accurately characterize the valley surface forcing and to provide calibration points for future use of hydrologic models. These measurements are discussed in detail in Chapter 5. Soil moisture measurements indicate that values provided by coarse meso-scale models are up to a factor of three higher than observed, which could lead to large errors in boundary layer forcing. Model results from simulations using four distinct surface soil moisture and snow cover initializations are compared to field data to quantitatively evaluate the effect of surface initialization.

There are several questions we seek to answer in this study and in ongoing research: How sensitive is the simulation of boundary layer processes to soil moisture initialization? Under what range of synoptic conditions (quiescent to strongly forced) do soil moisture effects dominate? At which grid nesting level or domain size should improved soil moisture data be incorporated? How do land-surface fluxes compete with external forcing through lateral boundary conditions? Answers to these questions will provide valuable information as to the requirements for initial conditions for land surface models in complex terrain.

## 6.3 Owens Valley and T-REX

Owens Valley is a rift valley in southeastern California which lies between the eastern slopes of the Sierra Nevada mountain range and the western slopes of the White Mountains and the Inyo Mountains. The peaks of the Sierras reach above 4,300 m (14,000 ft) while the valley floor lies at about 1,200 m (4,000 ft), making it one of the deepest valleys in the United States. The valley is approximately 120 km in length ($\sim$75 mi) and runs approximately north-south.

The main goal of the T-REX field campaign was to investigate the dynamics of atmospheric rotors and lee waves in Owens Valley, with broader goals including complex terrain boundary layer development, and stratospheric-tropospheric exchange. Additional scientific objectives include using the extensive T-REX datasets to validate numerical models to improve the accuracy of mesoscale and microscale modeling with the hope of being able to better predict aviation hazards, downslope windstorms, as well as transport and dispersion of aerosols.

A wide range of instruments were used in the collection of data for T-REX. Among these were: rawinsondes, dropsondes, lidars, flux towers, aircraft and soil moisture and temperature sensors [*Grubišić et al.*, 2004; *Grubisic et al.*, 2008]. A main source of data for comparison with ARPS model results are the Vaisala rawinsondes launched from Independence, CA at the center of Owens Valley. The sondes were launched every 1.5 hours from Independence Airport during EOP2, and every 3 hours from a site nearby during IOP6. Soundings are extracted from ARPS for direct comparison with rawinsonde data as well as with surface data collected at the Integrated Surface

Flux Facility (ISFF) central tower (in center of domain in Fig. 6.1), located near the Independence Airport.

## 6.4 Soil moisture and temperature measurements

Thirty soil moisture capacitance probes and temperature sensors were installed at 23 locations throughout Owens Valley to capture the spatial variability of land surface conditions (see Figure 6.1). A detailed discussion of the collection and calibration of these measurements can be found in Chapter 5, but are given briefly here. Decagon's ECH2O EC-20 soil moisture probes were used, along with ECH2OTemp temperature sensors and ECH2O EM50 data loggers. Most soil moisture probes and temperature sensors were located approximately 5 cm below the ground surface. A few were additionally placed 20-50 cm below the surface. Sensors were installed in two phases (September 2005 and January 2006) to allow adequate time for the soil disturbed in the installation procedure to return to its natural state. Data loggers recorded data every 5 minutes throughout the duration of the T-REX campaign (March and April, 2006). (Additional sets of sensors were placed at the three ISFF flux towers but these were managed separately.)

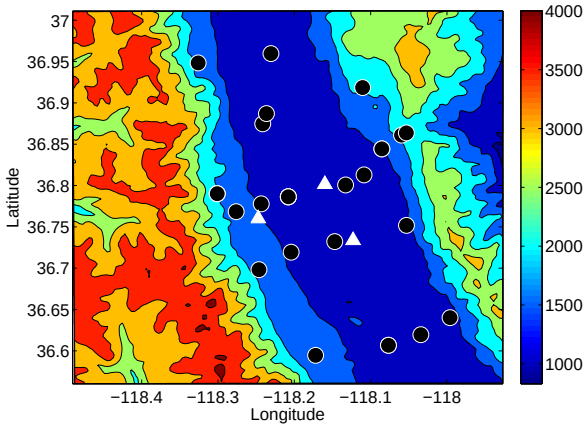


Figure 6.1. Elevation contours (m) of Owens Valley centered around Independence, CA from the 350 m resolution simulation domain. Circles indicate locations of soil moisture measurement sites and triangles show the three ISFF flux towers. An additional soil sensor was placed north of Independence, near Bishop (not shown).

In addition, two sets of soil cores were collected for gravimetric soil moisture measurements at the 23 sites around Owens Valley to serve as validation data for the ECH20 probes; the first set coincided with EOP2 and was taken over a period of 5 days from March 27 to March 31, 2006. These gravimetric measurements provided the average voumetric water content (VWC) of each soil sample at a depth of ∼5 cm. The average value (over all sites) of these measurements was 0.09 $m^3m^{-3}$. There was no precipitation in this area during this time. The spatial variability of observed soil moisture in Owens Valley is illustrated in Figure 6.2. Data from the 23 sites is linearly interpolated to provide the map shown. In general the soil in the valley is very dry (less than 0.1 $m^3m^{-3}$), except for a few sites near the Owens River which are significantly wetter (more than 0.3 $m^3m^{-3}$).

Two standard initialization datasets are used in this investigation to compare the impact of external forcing data: the North American Mesoscale model (NAM, 12 km horizontal resolution, Weather Research and Forecasting (WRF) model with analysis), and the North American Regional Reanalysis (NARR, 32 km horizontal resolution). NAM and NARR provide average soil moisture values of about 0.25 and 0.36 $m^3m^{-3}$ respectively, over the finest ARPS domain, approximately a factor of three or more times larger than observed. Gravimetric and capacitance data discussed in Chapter 5, and the results of coupled hydrologic modeling for Owens Valley discussed in Chapter 3 have been used to provide the ARPS simulations with more accurate soil moisture initialization data. Observations from the capacitence probes were used to validate the choice of altitude-dependent soil moisture levels for the valley based on 2D coupled hydrologic model simulations. These observations were also used to make a very simple adjustment to the NARR soil moisture field, such that the adjusted initial soil moisture everywhere in the domain is a factor of three less than the original standard NARR soil moisture. Initial soil moisture for the standard NAM and NARR initialization is shown in Figure 6.3 along with the altitude-dependent soil moisture field and the simple factor of three adjustment after an adjustment to the snow field discussed in section 6.5.3. We will be comparing the results of five simulations (summarized in Table 6.1) for each observing period (EOP2 and IOP6) to observations from T-REX. Comparisons will be made mainly between the REF and SM simulations; results of the SNO simulation will be discussed in terms of average differences between simulations and observations in section 6.8.

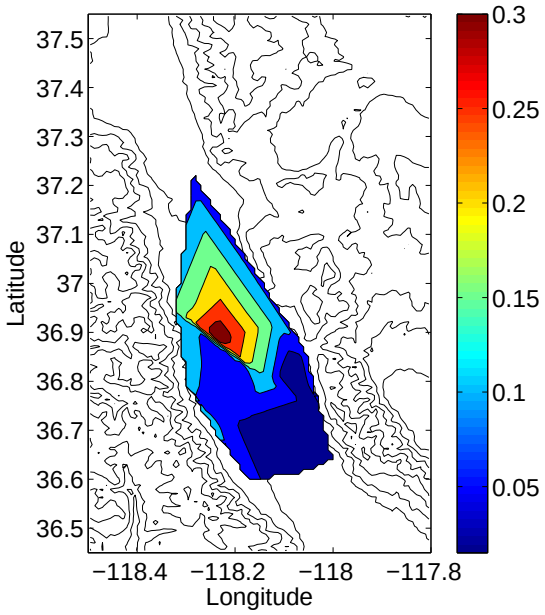


Figure 6.2. Contours of measured soil moisture ($m^3m^{-3}$) in Owens Valley using gravimetric sampling from March 27 to 31, 2006. Black contour lines show terrain elevation.

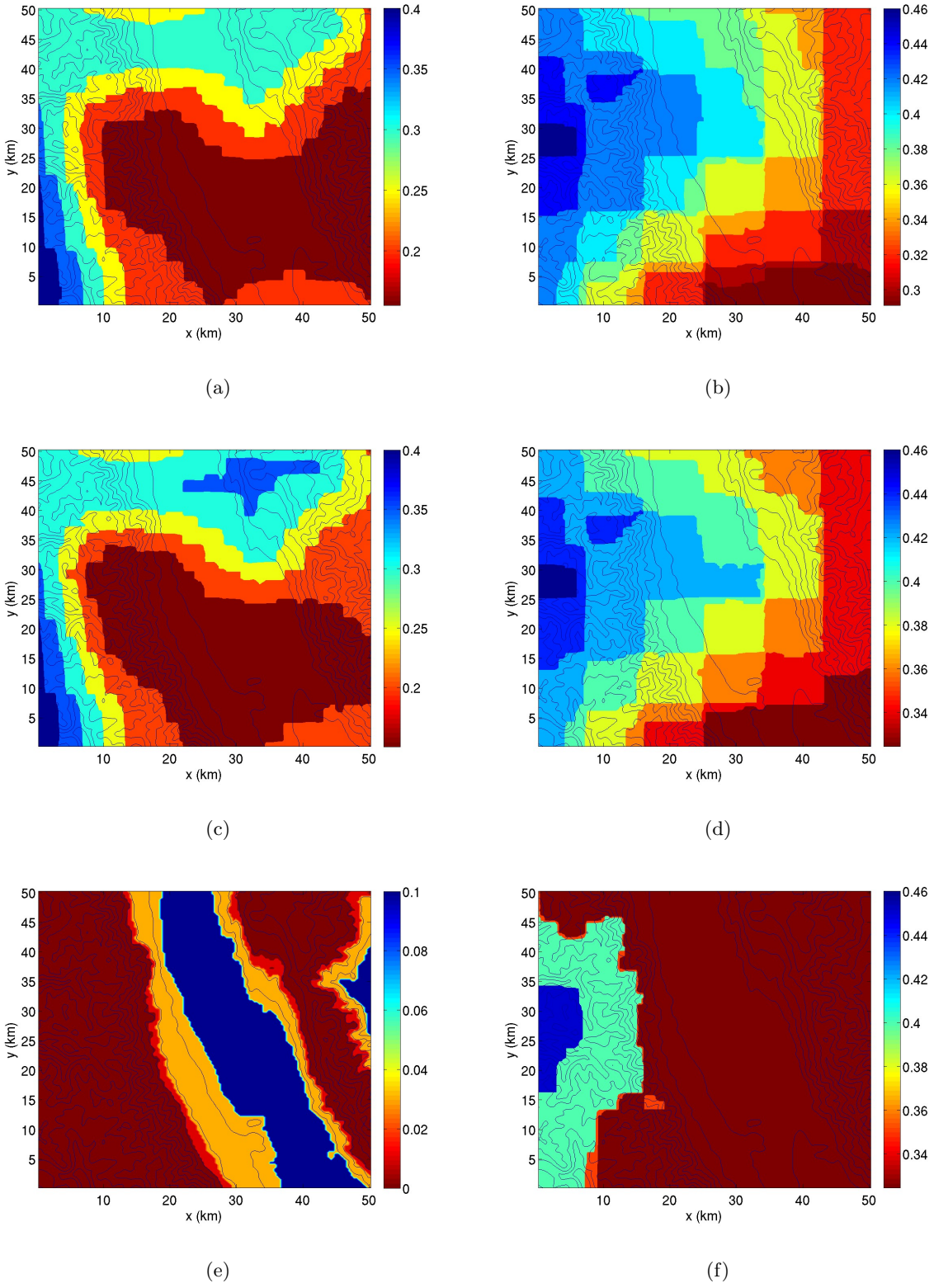


Figure 6.3. Initial soil moisture ($m^3/m^3$) Note difference in colorbars. Solid contours are terrain on 350 m grid. (a) NAM REF IOP6 (b) NARR REF IOP6 (c) NAM REF EOP2 (d) NARR REF EOP2 (e) NAM SM EOP2 (f) NARR SM EOP2

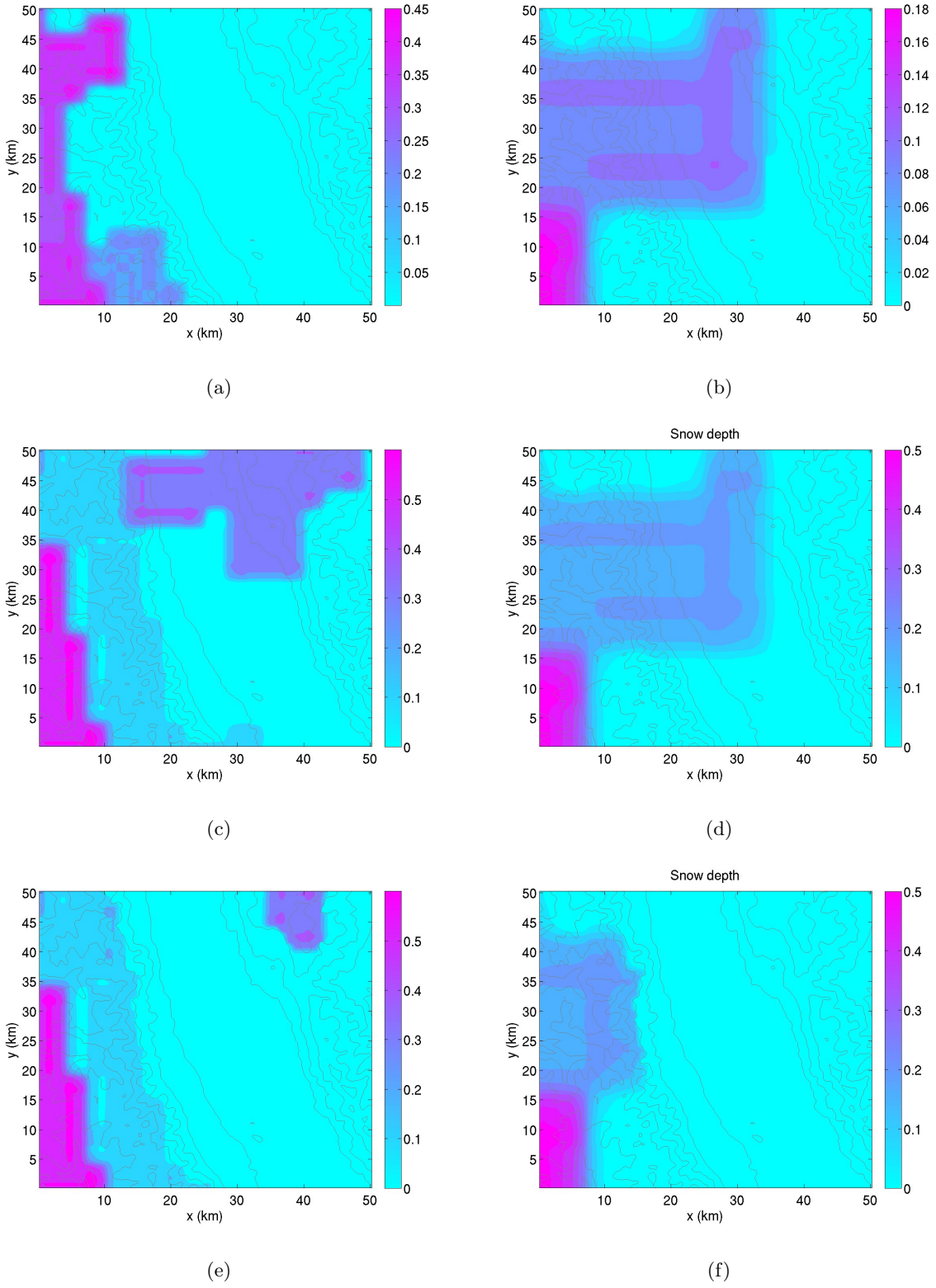


Figure 6.4. Initial snow depth (m). Solid contours are terrain on 350 m grid. (a) NAM REF IOP6 (b) NARR REF IOP6 (c) NAM REF EOP2 (d) NARR REF EOP2 (e) NAM SM EOP2 (f) NARR SM EOP2

Table 6.1. Initialization set-up.

| Name | Soil Moisture | Snow Cover |
|---|---|---|
| NAM REF | Interpolated (no modifications) | Interpolated (no modifications) |
| NAM SNO | Interpolated (no modifications) | Snow removed below 2500 m |
| NAM SM | Altitude-dependent | Snow removed below 2500 m |
| NARR REF | Interpolated (no modifications) | Interpolated (no modifications) |
| NARR SM | Uniformly adjusted | Snow removed below 2500 m |

## 6.5 Numerical simulation setup

ARPS is a comprehensive regional to storm-scale modeling and prediction system [*Xue et al.*, 2000, 2001, 2003]. It is a fully three-dimensional, nonhydrostatic, compressible numerical weather prediction model in generalized terrain-following coordinates and includes a full postprocessing package. Computations were performed using 16 to 64 processors at the Scientific Computing Division of the National Center for Atmospheric Research (NCAR). ARPS is used here in large-eddy simulation (LES) mode with a 1.5 TKE turbulence closure [*Deardorff*, 1980; *Moeng*, 1984]. Future work will include investigations of the different turbulence model options available in ARPS including dynamic mixed models [see *Chow et al.*, 2005].

### 6.5.1 Grid nesting and topography

For simulations initialized with NARR, four one-way nested grids are used to simulate flow conditions in Owens Valley at horizontal resolutions of 9 km, 3 km, 1 km, and 350 m (see Table 6.2 and Figure 6.5). For NAM, only the 3 finest grids are used. Topography for all grid resolutions was obtained using the USGS 3 arcsecond topography dataset. The terrain is smoothed at the edges of each subdomain so that the elevations at the boundaries match those of the surrounding coarser grid.

Horizontal grid spacing ($\Delta h$) is uniform in both directions. In ARPS, the minimum vertical spacing ($\Delta z_{min}$) is near the ground in a terrain-following $\sigma$-coordinate system. This minimum spacing, as well as the average vertical spacing ($\Delta z_{avg}$) are shown in Table 6.2. The domain height ($\sim 25$ km) extends beyond the tropopause. Large ($\Delta t$) and small ($\Delta \tau$) time steps must be specified in the mode-splitting scheme used in ARPS (see Table 6.2). These selections of grid spacing, time steps, and other parameters such as computational mixing coefficients, were made using experience gained through previous simulations over complex terrain [*Chow et al.*, 2006b; *Weigel et al.*, 2006].

### 6.5.2 Initialization and lateral boundary conditions

Initial and boundary conditions are set using data from the National Oceanic and Atmospheric Administration (NOAA) NAM and NARR datasets which are available at 12 km and 32 km resolution respectively. Relaxation towards the lateral boundary conditions was applied in a 12 grid-cell zone around the edge of the 9 km domain for NARR and the 3 km domain for NAM. NAM forcing

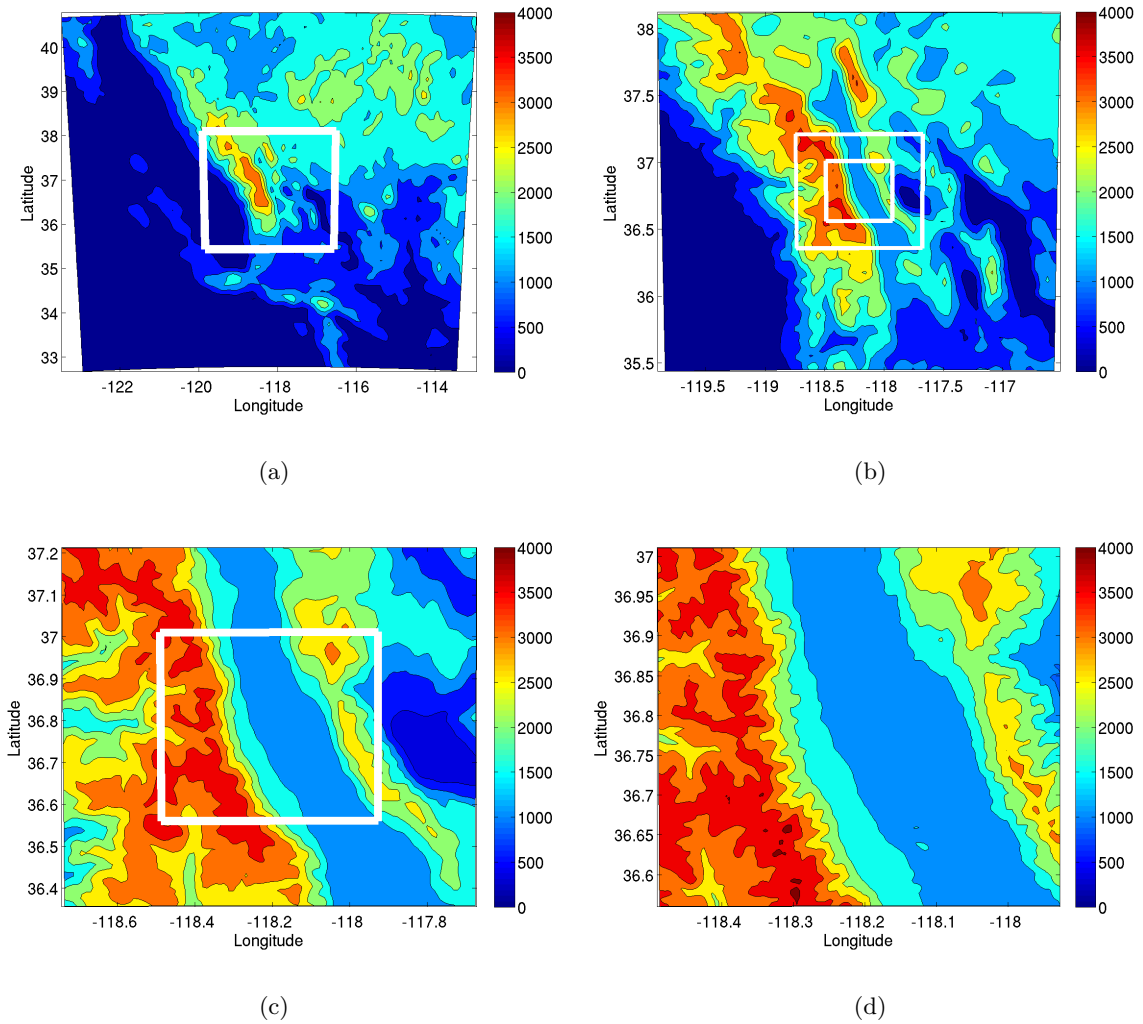


Figure 6.5. Terrain contours (meters above sea level) for the 9km, 3km, 1km, and 350m horizontal grid nests in ARPS. White boxes show extent of the next finer grid or grids. All four nests were used for simulations initialized with NARR. Simulations initialized with NAM used only the finest 3 grids.

Table 6.2. Simulation parameters for each grid level.

| (nx,ny,nz) | $\Delta h$ | $\Delta z_{min}$,$\Delta z_{avg}$ | $\Delta t$,$\Delta \tau$ |
|---|---|---|---|
| (103,103,53) | 9 km | 50 m, 500 m | 10 s, 10 s |
| (103,103,53) | 3 km | 40 m, 500 m | 2 s, 4 s |
| (99,99,63) | 1 km | 40 m, 400 m | 1 s, 1 s |
| (147,147,63) | 350 m | 30 m, 350 m | 1 s, 0.2 s |

was available at 6-hour intervals and NARR at 3-hour intervals; linear interpolation was used at intermediate times. An 11-hour spinup of each simulation was begun at 0400am PST (1200 UTC) March 29, 2006 for EOP2 and 1000pm PST (0600 UTC) March 24, 2006 for IOP6. Output was saved at hourly intervals for the 9km and 3km grids, and half-hourly intervals for the 1km and 350m grids. This output data was interpolated and used as lateral boundary forcing data for subsequent simulations at finer grid resolutions.

### 6.5.3 Land-surface model and land-use data

The characteristics of the land surface determine sensible and latent heat flux exchange with the atmosphere. The ARPS land-surface soil-vegetation model solves surface energy and moisture budget equations, described in detail in *Xue et al.* [2001]; *Ren and Xue* [2004]. ARPS generally uses 13 soil types (including water and ice), and 14 vegetation classes (following the United States Department of Agriculture classifications). Land use, vegetation, and soil type data for all Owens Valley grids are obtained from USGS 30 second global data.

For the soil temperature and moisture budgets, two soil layers of depths 0.01 m and 0.99 m for the surface and deep soil are used. In the standard procedure (used in the REF cases), soil temperature and moisture for all grids are initialized using values interpolated from the 12 km NAM or 32 km NARR fields. Interpolated initial soil moisture from NAM and NARR for IOP6 are shown in Figures 6.3(b) and 6.3(a). Values are higher for EOP2 interpolated NAM data (shown in Figure 6.3(d)) due to snow cover discussed in the following paragraph. The soil moisture and temperature values at 9 km resolution for NARR and 3 km resolution for NAM are then interpolated to the finer grids. The NARR soil moisture field (shown in Figure 6.3(c) has an average value of 0.36 $m^3m^{-3}$, approximately three times larger than the mean observed gravimetric value of 0.09 $m^3m^{-3}$. As a simple adjustment to this standard initialization, the NARR soil moisture field values are reduced by a factor of three and then used to initialize the ARPS 3 km domain for the NARR SM simulations.

In addition to modification of soil moisture, the initial snow depth is adjusted to correct for incompatabilities of the NAM and NARR snow fields with fine-resolution ARPS grids. For EOP2, both NAM and NARR data contain large 10-km patches of snow 0.2-0.4 m in depth at the northern end of the valley floor while no snow was actually present (see Figures 6.4(c) and 6.4(d)). This inconsistency is due to the coarse (12 km and 32 km) resolution terrain used by NAM and NARR which effectively smooths out Owens Valley ($\sim$20km wide near Independence) so that locations on the valley floor appear to be at much higher elevations where snow might be expected. For IOP6, NARR still shows a large snow patch across the valley floor (see Figure 6.4(b)), but NAM for March 24 shows that the snow visible on March 29 for EOP2 has not yet accumulated (see Figure 6.4(a)). This is a major difference in initial conditions between EOP2 and IOP6. To compensate for the lack of initialization data with a fine enough resolution to resolve Owens Valley, a minimum snow level elevation is imposed on all grids for the SM cases, such that the snow depth below 2500 m is always zero (see Figures 6.4(e) and 6.4(f)). While the snow level is imposed for both EOP2 and IOP6, its impact is far greater for EOP2. Simulation NARR SM is performed with an imposed snow level of 2500 m and an adjusted soil moisture field which approximates the observed field in an average sense. (See Figure 6.3(f).)

Altitude-dependent soil moisture is used to initialize the NAM SM simulations on the 1 km grid. Soil moisture values and bins were selected similar to *Chow et al.* [2006b] based on the results

of coupled hydrologic modeling discussed in Chapter 3 as well as the soil moisture measurements discussed in 5. Three bins were selected, with the wettest bin at the lowest part of the valley (below 1300 m), where the Owens River flows, a drier bin up the valley side walls (1300-1800 m), and the driest above 2000 m. See Figure 6.3(e). Since the model only considers soil moisture in cells where is there is no snow cover, soil moisture values beneath snow in the mountains do not affect the simulations.

## 6.6 Effects on surface variables

Soil temperature, sensible and latent heat fluxes all show marked sensitivity to snow cover and soil moisture initialization. Figures 6.6 and 6.7 show soil temperature in the late afternoon for EOP2 and IOP6, respectively. On both days, elevated soil moisture levels and snow patches on the valley floor of the REF cases leads to lower soil temperatures overall, especially in the snow-covered areas. For the SM cases, soil temperature contours follow the valley axis, with highest temperatures along the west-facing valley side-wall corresponding to the angle of the afternoon sun, and showing the influence of topography on heating of the land-surface. Soil temperature results from the altitude-dependent initialization (NAM SM) shown in Figures 6.6(b) and 6.7(b) show the most heating overall, especially on the valley floor.

Trends visible in soil temperature are also visible in plots of sensible heat flux shown in Figures 6.8 and 6.9, demonstrating that heating of the land-surface translates to heating of the air above the land-surface. On both days, the SM heat flux pattern follows the valley axis, showing largest fluxes on the west-facing slope as expected for this time of day. The REF heat flux pattern, on the other hand, is strongly affected by the large snow patch in the northern part of the domain, giving an unrealistic heat flux distribution. Maximum heat flux values occurring on the peaks of the Sierras correspond to high-elevation areas that are not covered by snow, but receive a high level of radiation at this time of day because of their prominent terrain height.

Soil moisture affects partitioning of energy into the sensible and latent heat fluxes. It follows that while the REF simulations show less sensible heat flux than the SM simulations, the opposite is true for latent heat flux shown in Figures 6.10 and 6.11. REF simulations show higher latent heat flux due to their higher soil moisture values which lead to more evaporation and less heating of the air (lower sensible heat flux) while SM simulations show lower latent heat flux and higher sensible heat flux because less water is available for evaporation and therefore more energy goes toward heating of the air.

## 6.7 Boundary layer evolution

Analysis of rawinsonde and surface data indicates that the winds in the Owens Valley during EOP2 exhibited some of the classic features of thermally-driven valley wind systems, while IOP6 exhibits the unique strength and intermittency of turbulent rotor flow. All results shown are from the 350 m resolution grid unless otherwise noted.

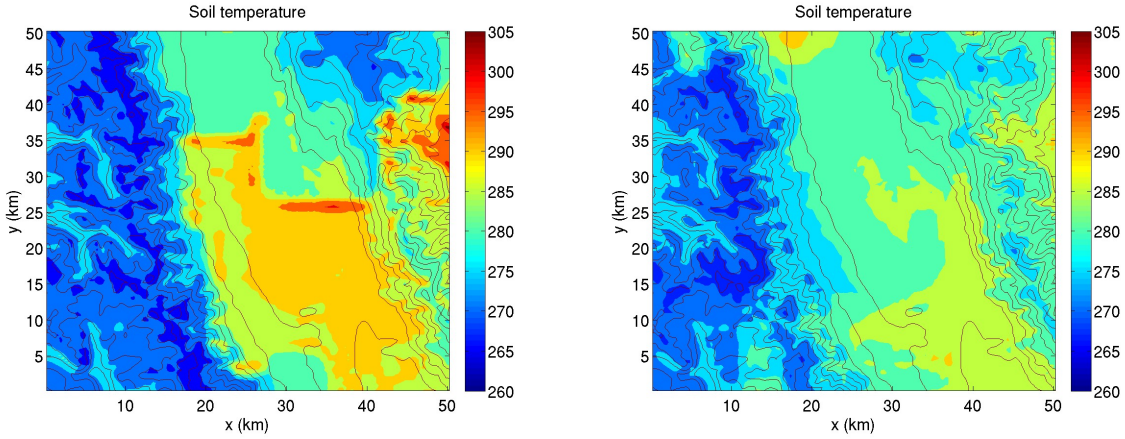


(a)




(b)

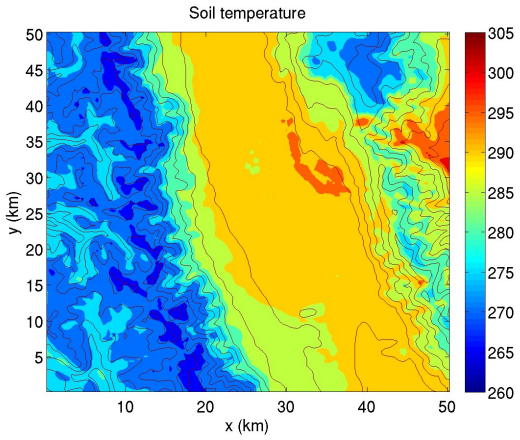


(c)

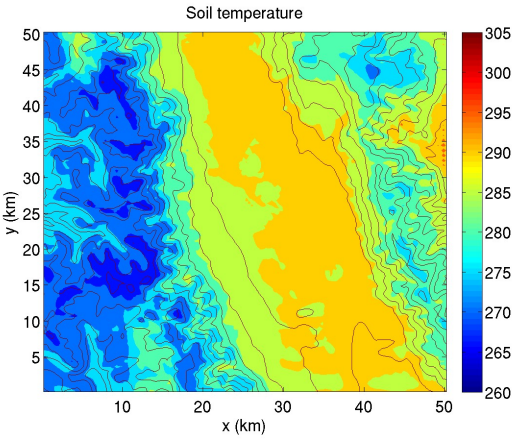


(d)

Figure 6.6. Contours of soil temperature (K) for EOP2 from REF (top) and SM (bottom) simulations at 0300pm PST (2300 UTC) on March 30, 2006. Solid lines show topography contours. (a) NAM REF (b) NARR REF (c) NAM SM (d) NARR SM

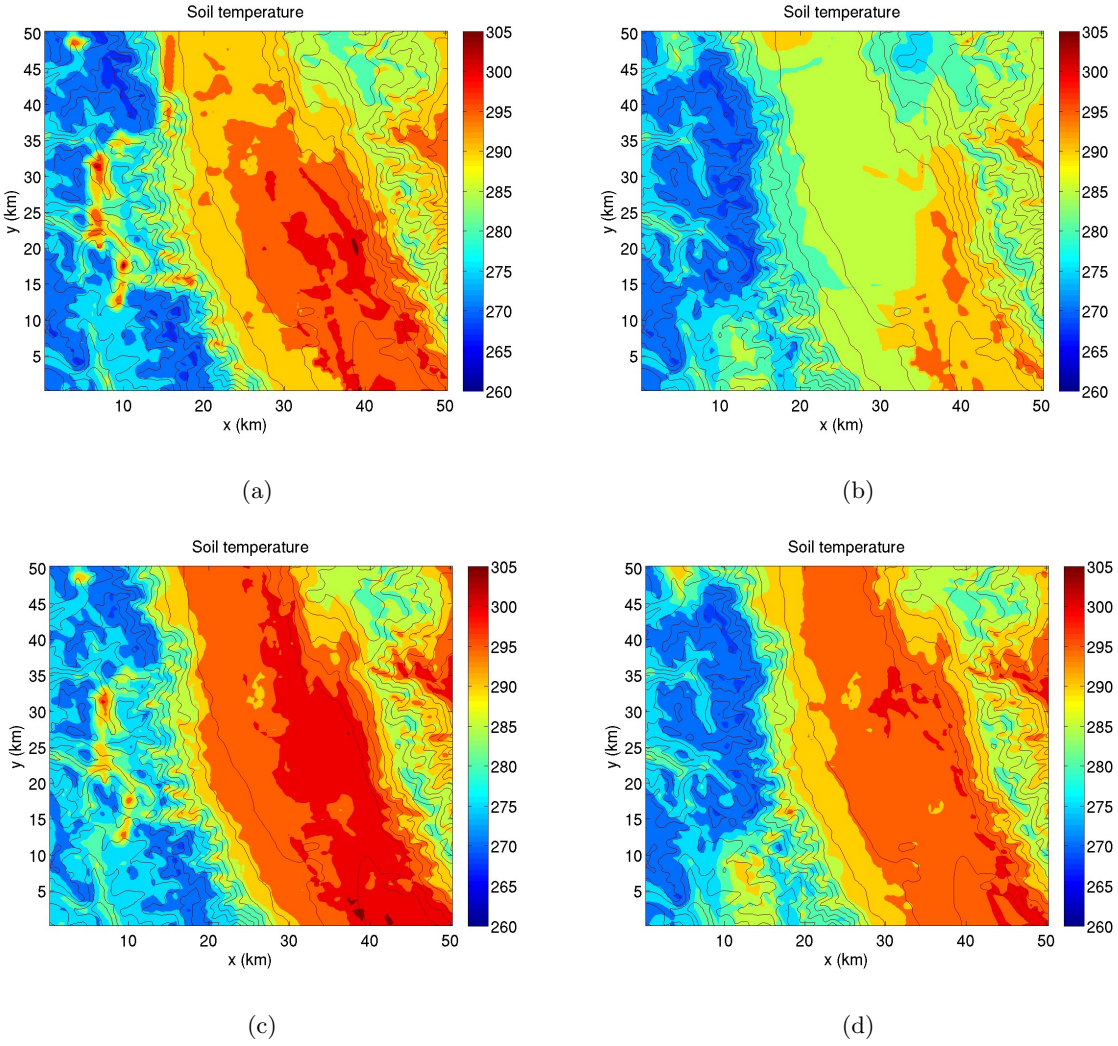


Figure 6.7. Contours of soil temperature (K) for IOP6 from REF (top) and SM (bottom) simulations at 0300pm PST (2300 UTC) on March 24, 2006. Solid lines show topography contours. (a) NAM REF (b) NARR REF (c) NAM SM (d) NARR SM

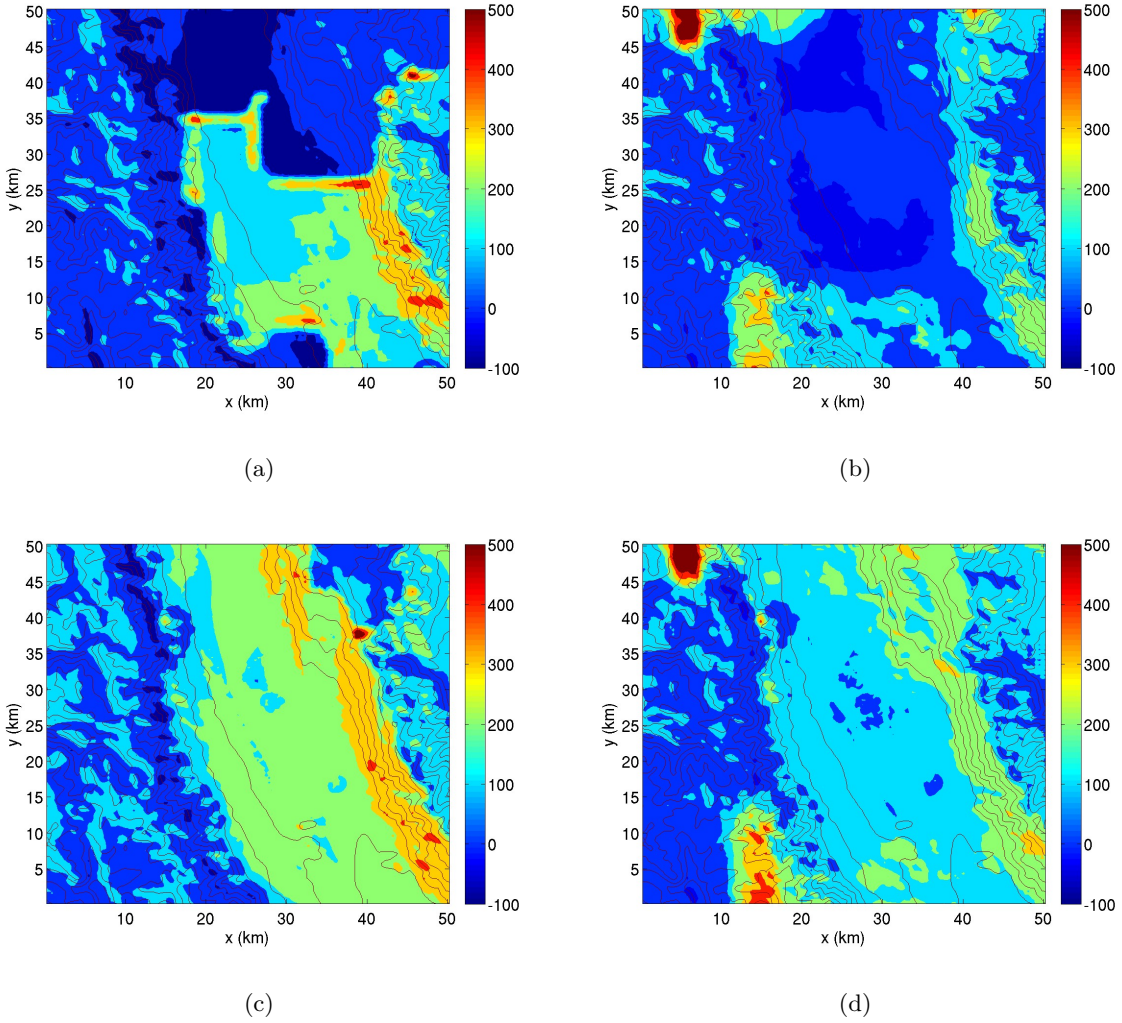


Figure 6.8. Contours of sensible heat flux (W/m$^2$) for EOP2 from REF (top) and SM (bottom) simulations at 0300pm PST (2300 UTC) on March 30, 2006. Solid lines show topography contours. (a) NAM REF (b) NARR REF (c) NAM SM (d) NARR SM

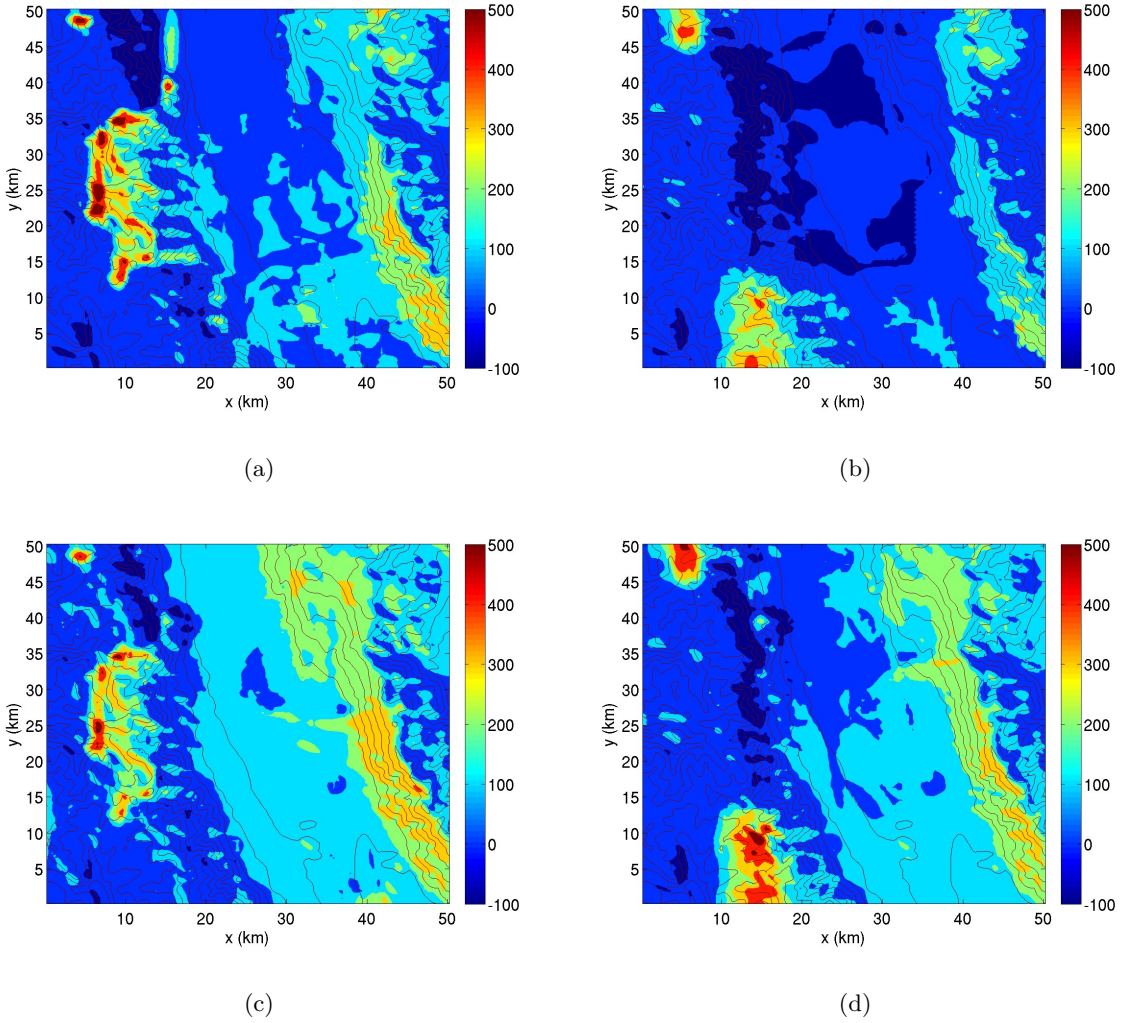


Figure 6.9. Contours of sensible heat flux ($W/m^2$) for IOP6 from REF (top) and SM (bottom) simulations at 0300pm PST (2300 UTC) on March 24, 2006. Solid lines show topography contours. (a) NAM REF (b) NARR REF (c) NAM SM (d) NARR SM

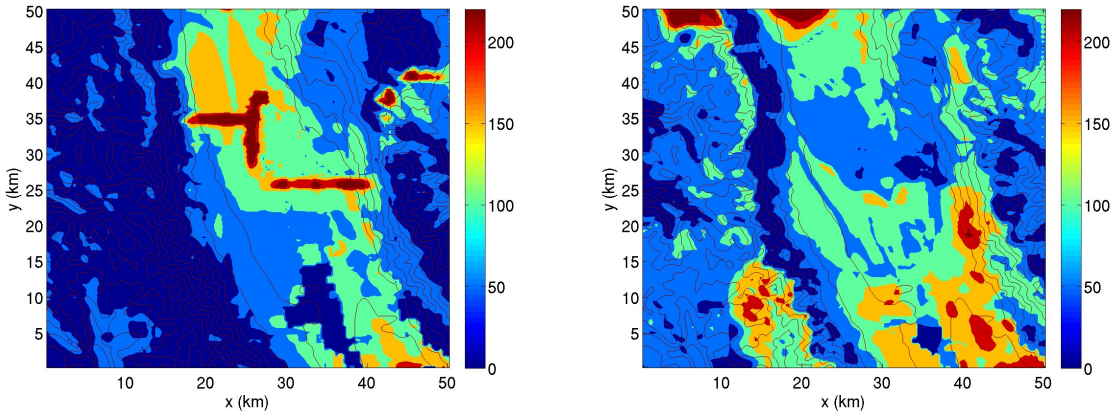


(a)




(b)

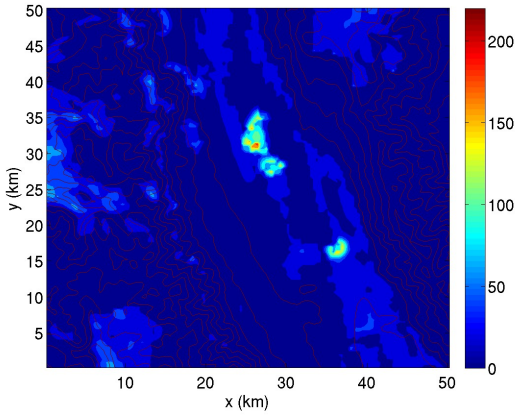


(c)

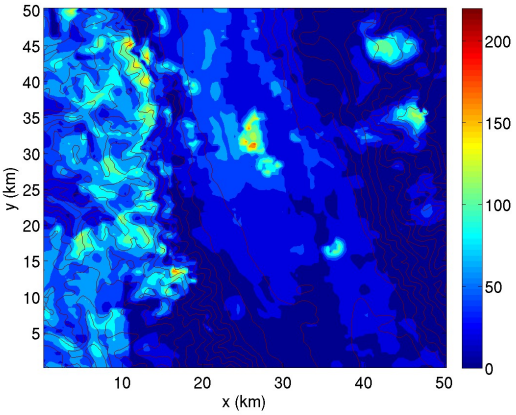


(d)

Figure 6.10. Contours of latent heat flux (W/m$^2$) for EOP2 from REF (top) and SM (bottom) simulations at 0300pm PST (2300 UTC) on March 30, 2006. Solid lines show topography contours. (a) NAM REF (b) NARR REF (c) NAM SM (d) NARR SM

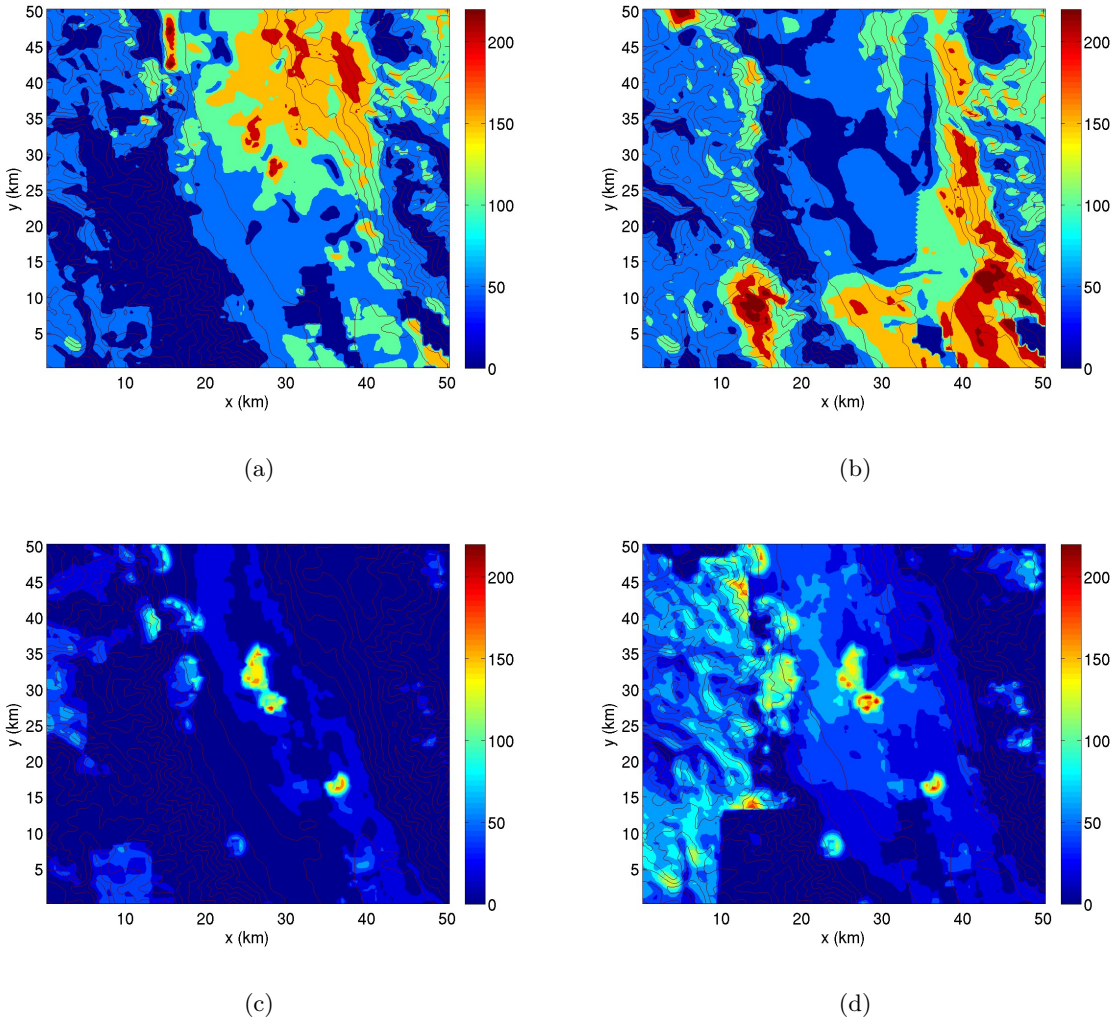


Figure 6.11. Contours of latent heat flux (W/m$^2$) for IOP6 from REF (top) and SM (bottom) simulations at 0300pm PST (2300 UTC) on March 24, 2006. Solid lines show topography contours. (a) NAM REF (b) NARR REF (c) NAM SM (d) NARR SM

### 6.7.1 Comparisons to surface observations

Figures 6.12, 6.13, and 6.14 show the evolution of potential temperature, surface wind speed and direction, and specific humidity at the ISFF central flux tower (see Figure 6.1) near the center (118.1600 W, 36.8015 N) of the simulation domains, compared to results from the REF and SM simulations.

For EOP2, the surface observations show down-valley flow at the surface at the beginning of the EOP and continuing throughout the night, until 1500 UTC (7am PST) when a gradual transition in winds is apparent (Figure 6.12(a)); an intermediate between up-valley and up-slope flow (100 degrees) is established by 1800 UTC (10am PST). The wind direction transition is accompanied by an increase in wind speed beginning at about 1700 UTC (9 am PST) (Figure 6.12(b)).

All four ARPS simulations (REF and SM) capture the general features of the surface time series well. The predicted potential temperature from the REF simulations are too low by ∼3-6 K throughout the EOP, with somewhat better performance from the SM results. The SM simulations exhibit a morning wind transition at approximately the time observed but includes more of an up-valley wind component (winds observed aloft display primarily up-valley flow as seen later in Figure 6.15). The REF cases show a delayed wind transition after sunrise compared to the observations, (see Figures 6.12(a) and 6.12(b)); REF surface winds at the ISFF flux tower site remain down-valley for 3 hours after the observed transition in wind direction and neither NAM REF nor NARR REF produce the observed increase in wind speeds. Simulated specific humidity values are also much improved for the SM cases. NARR SM is drier than NAM SM, leading to lower humidity values and higher potential temperature for the beginning of EOP2, but overall NAM SM predicts wind transitions most accurately. These results will be quantified in section 6.8.

The rotor flow conditions of IOP6 make interpretation of surface winds less straight-forward. While winds are up-valley at the beginning of IOP6, they become highly changeable overnight, along with surface wind speeds. The night and second day of IOP6 can be characterized as having turbulent flow structure, showing high variability of wind speed and direction. The simulations using NAM initialization data do moderately well at capturing the observed surface wind speeds, and have some success in capturing observed surface wind direction, though they are unable to reproduce the high variability characteristic of the observed winds. The NAM simulations do however capture the breakthrough of westerlies (270 degrees) in the last few hours of IOP6. It is possible that a simulation with higher grid resolution would have more success at capturing the smaller-scale turbulent structures which are present in the observations. Such simulations would require a much smaller domain size, however horizontal domain extent is limited by the need to include the mountain peaks within the domain so as to include effects of terrain shading.

Even without higher resolution, the simulations using NAM initialization data are able to capture the diurnal potential temperature variation of IOP6 quite well. Exceptions include oscillations between high and low temperatures visible overnight, which may be due to stable stratification and intermittent turbulence. NAM simulations predict consistently low values overnight, and NARR predicts the higher end of the observed range, but neither are able to capture the observed variability. Two delayed morning transitions are apparent during IOP6 for all four (REF and SM) simulations, which may be due to a spurious cloud layer around 8 km which is present in both sets of initialization data.

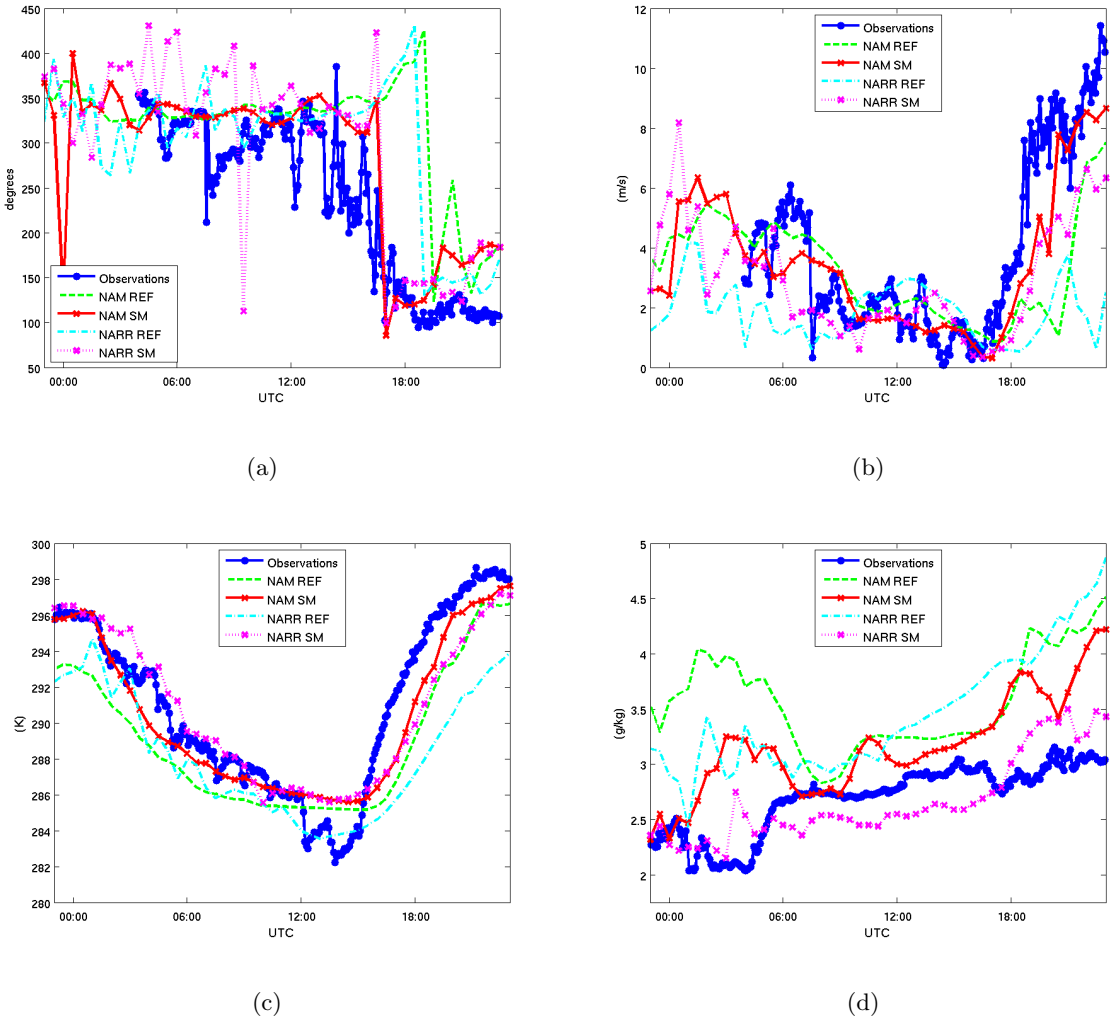


(a) (b)

(c) (d)

Figure 6.12. EOP2 surface data time series at ISFF central tower (valley floor) for (a) wind direction, (b) wind speed, (c) potential temperature, and (d) specific humidity. Observations at 15 m AGL (blue), NAM REF (green), NAM SM (red), NARR REF (cyan), NARR SM (magenta)

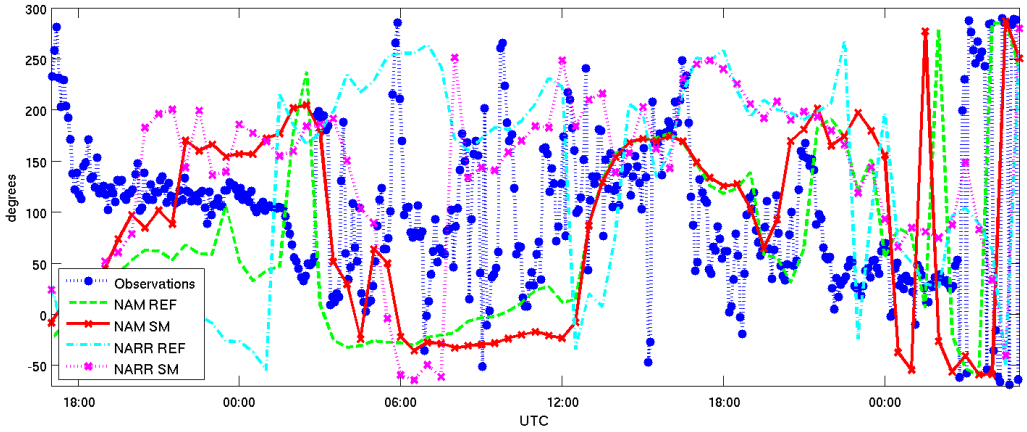


(a)

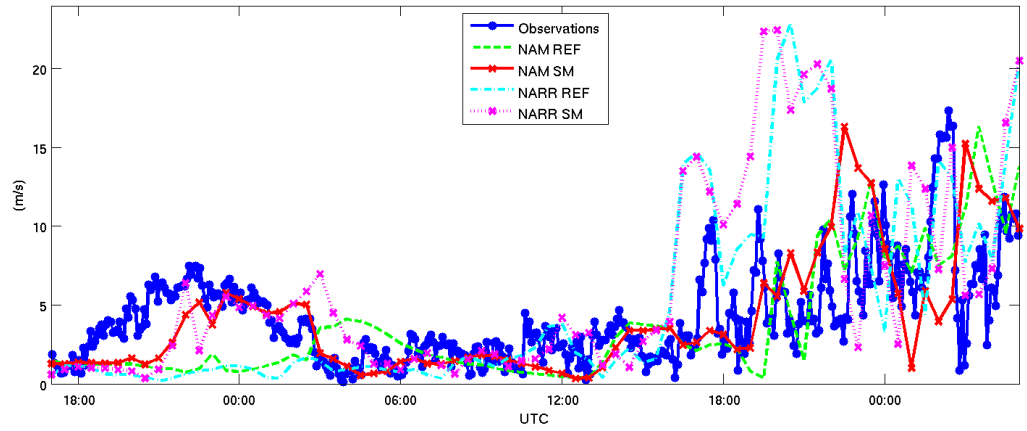


(b)

Figure 6.13. IOP6 surface data time series at ISFF central tower (valley floor) for (a) wind direction and (b) wind speed. Observations at 15 m AGL (blue), NAM REF (green), NAM SM (red), NARR REF (cyan), NARR SM (magenta)

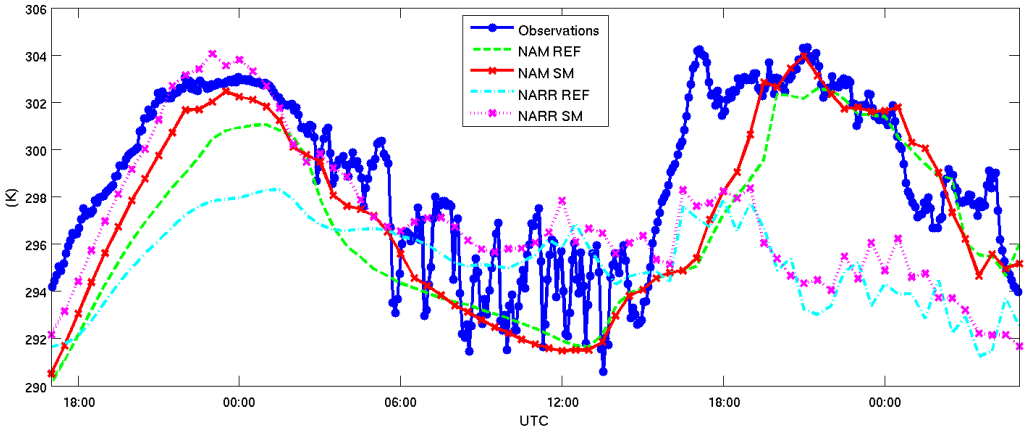


(a)

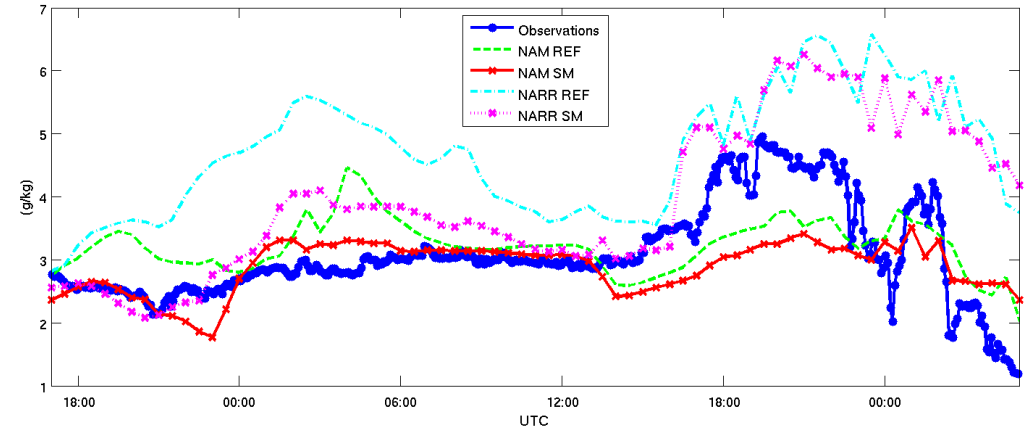


(b)

Figure 6.14. IOP6 surface data time series at ISFF central tower (valley floor) for (a) potential temperature, and (b) specific humidity. Observations at 15 m AGL (blue), NAM REF (green), NAM SM (red), NARR REF (cyan), NARR SM (magenta)

### 6.7.2 Comparisons to sounding observations

#### Discussion of EOP2

Analysis of vertical profiles in Owens Valley reveals a much more complex wind structure. Soundings were extracted from the ARPS simulations and compared directly to data from rawinsondes launched from Independence, CA (at Independence Airport, at the ISFF central tower site) at approximately 1.5 hour intervals during EOP2 (see Fig. 6.15). An additional sounding from 0300pm PST (2300 UTC) on March 30 is included here as well. Rawinsonde data show a neutral atmosphere up to about 4.5 km ASL (approximately ridge-top level) in the late afternoon on March 29, with a 12-14 degree elevated inversion between 4.5 and 5 km ASL. A nighttime surface inversion layer begins to grow just after sunset and increases through the night. As the surface inversion grows, the elevated inversion sinks (approximately 1 km in 12 hrs), reaching its lowest point just before sunrise. In general all four (REF and SM) simulations match the observations up to this time; the two SM simulations match particularly well in the evening hours and show much improvement in specific humidity values. All simulations, however, predict cooler overnight surface temperatures than the observations and are significantly delayed in predicting the development of the convective boundary layer after sunrise. This under-predication of nighttime surface temperature results in the potential temperature profiles of all simulations lagging behind by about three hours in establishing the surface mixed layer. Even as late as noon, only the SM simulations show a mixed layer, and then it is 3-4 degrees colder than and not as deep as observed (Figure 6.15). The representation of the elevated inversion is quite poor in both simulations during this time; a lack of high enough resolution at this altitude may contribute to the smearing of this profile. As seen in the time series plots above (Figure 6.12), the near-surface winds in the REF case do not show up-valley flow soon enough after sunrise.

Rawinsonde profiles reveal the development of elevated layer of opposing flow, beginning in the late evening hours of March 29th. The profiles shown for 0251am PST (Figure 6.15), for example, clearly show three distinct wind layers. Figure 6.16 shows a vertical cross section of along-valley wind contours from the NAM SM simulation; the down-valley and up-valley flow structure within the valley atmosphere are clearly delineated. The down-valley flow at the surface has a magnitude of 5-10 m/s and is initially coupled with a return flow (up-valley) of weaker magnitude which occurs between 2600 and 3400 m asl. The layer of opposing flow grows and the down-valley surface wind weakens during the night, with a layer of flow of magnitude 5-10 m/s occurring between 2000 and 3300 m asl just before sunrise. These winds are entirely decoupled from winds above the surrounding mountain tops, being separated by a strong inversion. The capping inversion subsides during the night, with the valley boundary layer depth decreasing from ridge crest height ($\sim$4200 m) to 3300 m asl by sunrise. Within an hour or two after sunrise, the down-valley flow disappears entirely, and up-valley flow is observed over the whole boundary layer depth. These valley-confined return flows are often weaker than flows at the valley floor and much weaker than the prevailing synoptic winds, and are therefore infrequently observed [*Whiteman*, 2000; *Buettner and Thyer*, 1966; *Reuten et al.*, 2005; *McGowan*, 2004]. This flow structure is discussed further in related work [*Schmidli et al.*, 2009].

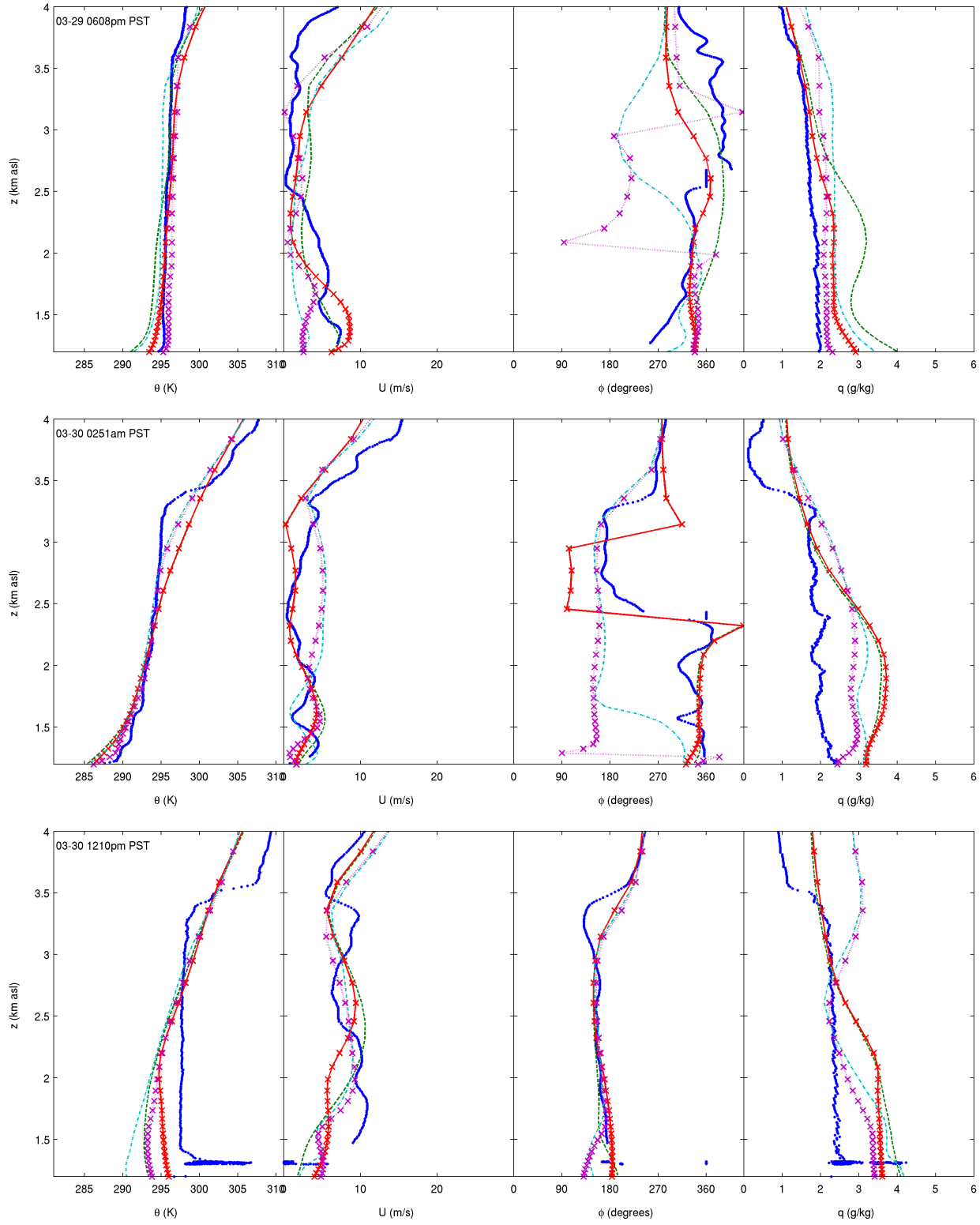


Figure 6.15. Selected soundings from EOP2 at Independence Airport of potential temperature, wind speed, wind direction, and specific humidity at 0608pm PST, 0251am PST, and 1210pm PST. Observations at 15 m AGL (blue), NAM REF (green –), NAM SM (red x), NARR REF (cyan .-), NARR SM (magenta x)

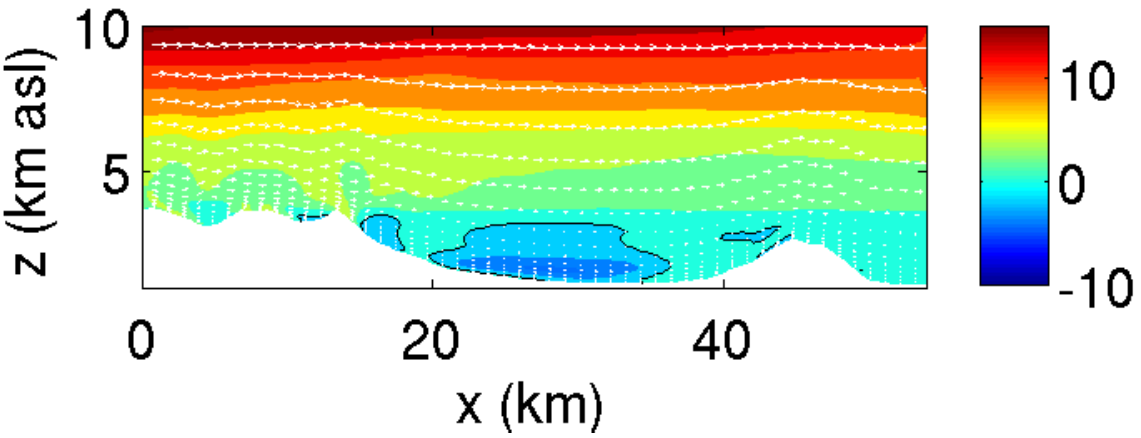


Figure 6.16. Vertical cross section of along-valley winds at 0300am PST from the SM simulations. Slice passes through Independence, perpendicular to the valley axis. Velocities have been rotated to be aligned with the valley axis so that $u$ is cross-valley (to the north-east) and $v$ (shown here) is along-valley (to the north-west).

**Discussion of IOP6**

Rawinsonde data from IOP6 reveal many interesting features including evidence of downward velocities strong enough to force an ascending sonde to descend over more than 1.5 km in one case, and over 1 km in several others. An example of this is the March 25 07:12pm PST sounding shown in Figure 6.17. Often the wind speed and direction data was not retrieved during these soundings due to instrument failure under exceptionally strong wind conditions, and even the soundings which did return wind data show evidence of strong turbulent motions below ridge crest height (approximately 4 km ASL, e.g. first two soundings of Figure 6.17). Figure 6.18 shows cross sections perpendicular to the valley axis where the simulations capture vortex shedding off the Sierra crest. In these plots, the slice through the REF case shows distinct vortices, but the SM case shows clear vortex shedding at later times (not shown). The elevated high-vorticity layer shown in Figure 6.19 persists throughout the night of March 24, 2006 and into the following day.

## 6.8 Quantifying differences between simulations and observations

A more quantitative comparison of model results and observations can be obtained by examining the magnitude of errors between the observations and the simulation results. Tables 6.3 and 6.4 show the root-mean-square errors (rmse) and mean errors (bias) at the surface and from soundings respectively for EOP2, while Tables 6.5 and 6.6 are for IOP6. Comparisons are between observations and simulations for potential temperature, wind speed and direction, and specific humidity at the ISFF central tower and from the radiosonde data (averaged over all 18 launch times for EOP2 and 10 launch times for IOP6). The bias provides an indication of the average direction of deviation of the modeled from the observed data, whereas the rmse provides an estimate of the magnitude of

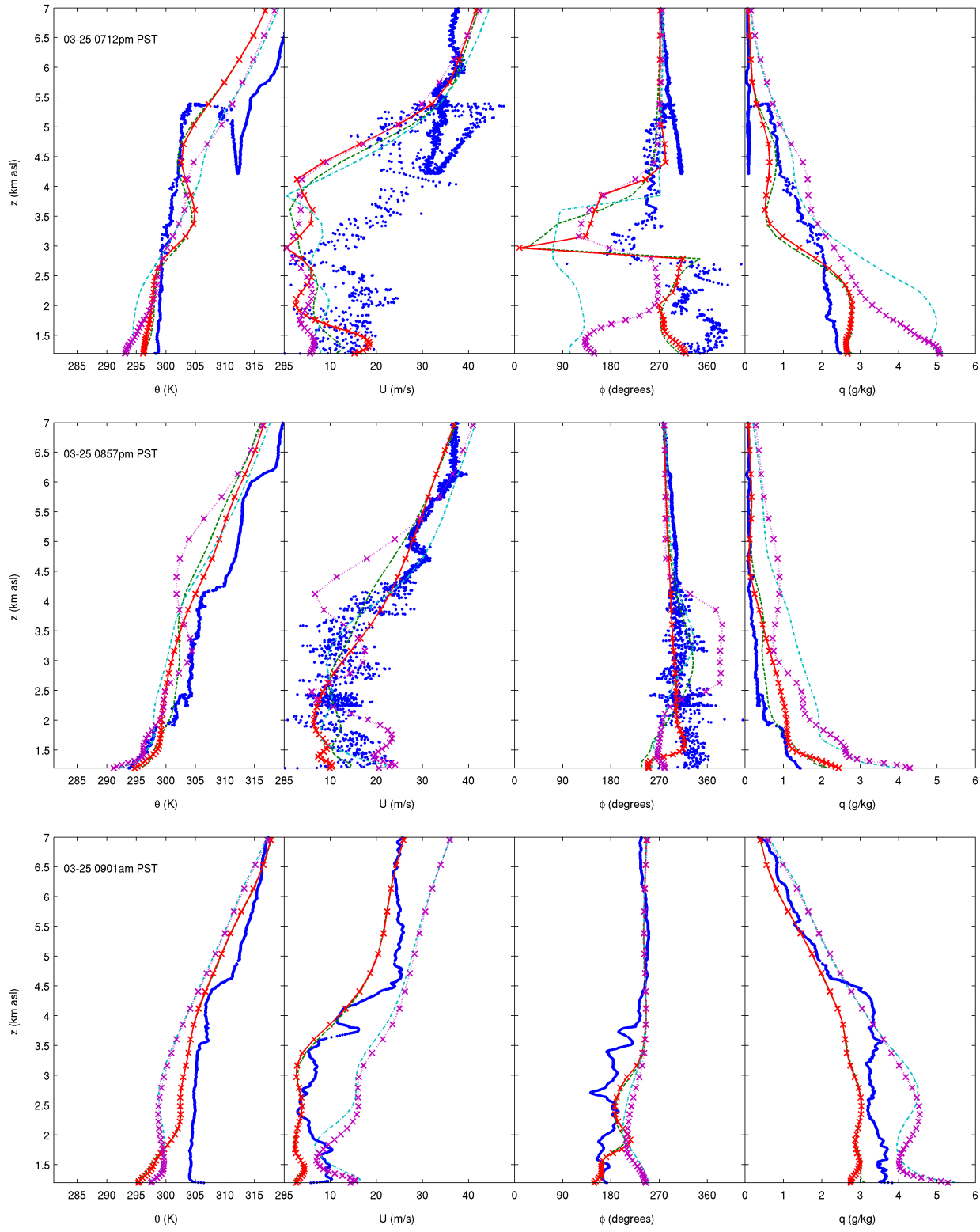


Figure 6.17. Selected soundings from IOP6 near Independence Airport of potential temperature, wind speed, wind direction, and specific humidity at 0608pm PST, 0251am PST, and 1210pm PST. Observations at 15 m AGL (blue), NAM REF (green –), NAM SM (red x), NARR REF (cyan .-), NARR SM (magenta x)

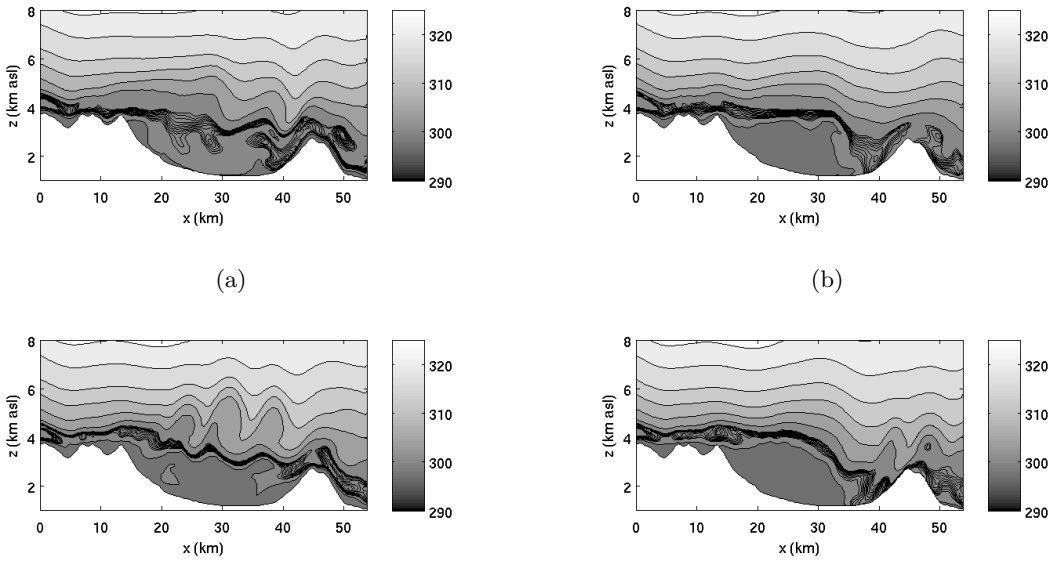


Figure 6.18. Comparison of vertical cross sections of potential temperature. Flow structure varies considerably between REF and SM at this time. Slice passes through Independence, perpendicular to the valley axis. (a) NAM REF at 1700 PST March 24, 2006 (0100 UTC March 25, 2006) (b) NAM SM at 1700 PST (c) NAM REF at 1730 PST (d) NAM SM at 1730 PST

the error. For EOP2, the errors are overall larger for the surface time series comparisons than for the rawinsonde data while the opposite was true for IOP6. Wind direction bias values could likely be reduced with some smoothing of the observations which fluctuate significantly, especially when winds are weak. For EOP2, errors for the SM case are significantly smaller than for the standard REF results, while the SNO simulation (standard interpolated soil moisture, but with the snow level imposed) shows intermediate improvement over the REF simulation, with the notable exception of specific humidity, which shows higher rmse and bias for the SNO simulation, most likely due to the exposed high soil moisture soil providing water for evaporation. The SM results significantly reduce the errors in all comparisons (e.g. rmse values for potential temperature are resduced from 2.87 to 1.63), indicating the improvement that can be obtained with better land-surface data for initialization.

The trend is less clear for IOP6 (see Tables 6.5 and 6.6). Surface time series errors are lower for the SM simulations than REF for potential temperature during IOP6 for both NAM and NARR, but for NAM there is no definitive improvement in comparisons to winds and humidity, while there generally is for NARR. Comparisons to sounding data lead to similar conclusions; NARR SM simulations show improvement over NARR REF, but NAM REF, SNO, and SM show comparable rmse and bias values. This may be because there was almost no difference in snow cover in the NAM initialization data for IOP6. It is interesting to note that simulation results differ between NAM REF, NAM SNO, and NAM SM, as shown for REF and SM in Figures 6.13 and 6.14, but average rmse and bias do not show a trend. It is possible that the conditions during IOP6 (high winds) make it difficult to compare with observations since radiosondes are blown far away from their launch location and we are therefore comparing one column location (directly above the launch site) from

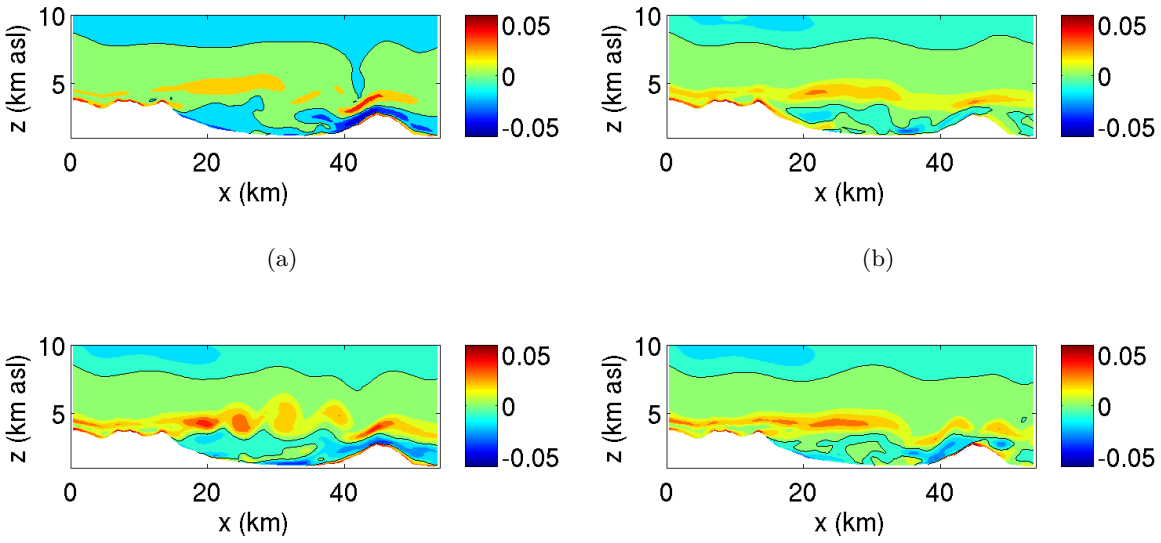


Figure 6.19. Comparison of vertical cross sections of the cross-valley component of vorticity. Strength of rotation is stronger in REF than SM at this time. Slice passes through Independence, perpendicular to the valley axis. (a) NAM REF at 1700 PST March 24, 2006 (0100 UTC March 25, 2006) (b) NAM SM at 1700 PST (c) NAM REF at 1730 PST (d) NAM SM at 1730 PST

the simulation to locations which are potentially several kilometers away. This could partially explain why comparisons to surface observations of potential temperature show improvement in NAM SM over NAM REF while sounding comparisons do not. Better methods of comparison may be key to determining whether improved soil moisture and snow cover initialization are necessary to increase accuracy of simulations under conditions similar to IOP6.

## 6.9 Discussion and future work

The work described in this chapter seeks to characterize the effects of the land surface on the development of the atmospheric boundary layer over complex terrain under weak and strong meteorological forcing through comparisons to field observations. Both accurate initialization datasets and improved land-surface models are ultimately needed to understand the role of surface forcing on the atmosphere.

The simulations presented here were able to capture the overall structure of the Owens Valley atmosphere during the T-REX field campaign, including the development of an elevated opposing flow layer during the night of EOP2 as well as vortex shedding in the lee of the Sierra Nevada during IOP6. The NARR SM simulations with soil moisture adjusted to better match measurements from gravimetric sampling in the valley, and for EOP2 the NAM SM simulations with altitude-dependent soil moisture, were better able to capture the structure of the observed rawinsonde profiles than

Table 6.3. EOP2 overall root-mean-square errors (rmse) and mean errors (bias) for potential temperature, wind speed, wind direction, and specific humidity predicted by five ARPS cases compared to surface observations at the ISFF central tower.

| | NAM REF | NAM SNO | NAM SM | NARR REF | NARR SM |
|---|---|---|---|---|---|
| $\theta$ rmse (K) | 2.87 | 1.89 | 1.63 | 3.85 | 1.77 |
| $\theta$ bias (K) | -2.28 | -0.75 | -0.77 | -3.33 | -0.54 |
| $U$ rmse (m/s) | 2.47 | 2.25 | 1.77 | 3.42 | 2.16 |
| $U$ bias (m/s) | -0.50 | -0.81 | -0.29 | -1.95 | -0.82 |
| $\phi$ rmse (deg) | 61.69 | 46.20 | 52.25 | 55.51 | 66.22 |
| $\phi$ bias (deg) | 22.26 | 27.46 | 33.25 | 14.09 | 45.98 |
| $q$ rmse (deg) | 1.07 | 1.05 | 0.61 | 0.92 | 0.29 |
| $q$ bias (deg) | 0.91 | 0.98 | 0.47 | 0.81 | -0.01 |

Table 6.4. EOP2 overall root-mean-square errors (rmse) and mean errors (bias) for potential temperature, wind speed, wind direction, and specific humidity predicted by five ARPS cases compared to soundings at Independence Airport.

| | NAM REF | NAM SNO | NAM SM | NARR REF | NARR SM |
|---|---|---|---|---|---|
| $\theta$ rmse (K) | 1.56 | 1.38 | 1.29 | 1.66 | 1.17 |
| $\theta$ bias (K) | -0.52 | -0.19 | -0.27 | -0.56 | -0.09 |
| $U$ rmse (m/s) | 1.96 | 1.97 | 1.85 | 2.05 | 1.96 |
| $U$ bias (m/s) | -0.29 | -0.37 | -0.29 | -0.33 | -0.31 |
| $\phi$ rmse (deg) | 24.70 | 22.55 | 23.23 | 40.82 | 40.85 |
| $\phi$ bias (deg) | 2.12 | 0.47 | 1.35 | -1.50 | 3.84 |
| $q$ rmse (g/kg) | 0.81 | 0.88 | 0.78 | 0.74 | 0.57 |
| $q$ bias (g/kg) | 0.50 | 0.54 | 0.47 | 0.48 | 0.34 |

Table 6.5. IOP6 overall root-mean-square errors (rmse) and mean errors (bias) for potential temperature, wind speed, wind direction, and specific humidity predicted by five ARPS cases compared to surface observations at the ISFF central tower.

| | NAM REF | NAM SNO | NAM SM | NARR REF | NARR SM |
|---|---|---|---|---|---|
| $\theta$ rmse (K) | 3.15 | 3.05 | 2.62 | 4.96 | 3.86 |
| $\theta$ bias (K) | -2.34 | -2.31 | -1.69 | -3.74 | -1.91 |
| $U$ rmse (m/s) | 3.52 | 3.47 | 3.61 | 5.39 | 5.62 |
| $U$ bias (m/s) | -0.62 | -0.63 | -0.24 | 0.79 | 1.72 |
| $\phi$ rmse (deg) | 79.30 | 84.96 | 80.75 | 123.67 | 98.21 |
| $\phi$ bias (deg) | -20.13 | -14.81 | 0.45 | -9.91 | 33.02 |
| $q$ rmse (deg) | 0.72 | 0.73 | 0.68 | 1.88 | 1.29 |
| $q$ bias (deg) | 0.18 | 0.26 | -0.19 | 1.68 | 0.89 |

Table 6.6. IOP6 overall root-mean-square errors (rmse) and mean errors (bias) for potential temperature, wind speed, wind direction, and specific humidity predicted by five ARPS cases compared to soundings at Independence Airport.

| | NAM REF | NAM SNO | NAM SM | NARR REF | NARR SM |
|---|---|---|---|---|---|
| $\theta$ rmse (K) | 2.58 | 2.56 | 2.72 | 3.63 | 3.29 |
| $\theta$ bias (K) | -0.95 | -0.93 | -1.00 | -1.48 | -1.21 |
| $U$ rmse (m/s) | 3.82 | 3.30 | 3.86 | 4.38 | 4.67 |
| $U$ bias (m/s) | -1.22 | -0.95 | -1.27 | -0.40 | -0.41 |
| $\phi$ rmse (deg) | 38.29 | 30.49 | 30.99 | 33.52 | 33.78 |
| $\phi$ bias (deg) | -5.36 | -6.29 | -5.28 | 2.72 | 0.70 |
| $q$ rmse (g/kg) | 0.71 | 0.69 | 0.66 | 1.28 | 1.03 |
| $q$ bias (g/kg) | 0.13 | 0.13 | 0.11 | 0.55 | 0.39 |

the REF cases. A major difference between the EOP2 and IOP6 simulations was the presence of snow on the valley floor for the NAM REF case of EOP2 which was completely lacking in the IOP6 NAM REF case. Thus the improved performance evidenced by significant reductions in mean and rmse errors for SM over REF during EOP2 is not as clear for IOP6, though surface time series rmse and bias were significantly reduced.

The simulations presented here provide evidence of the need for better surface initialization of mesoscale models in complex terrain. Simulations run with standard NAM soil moisture, but with a snow level imposed show that there is some improvement in comparisons to observations when snow is removed from the valley floor, however, the most significant improvement is achieved when both soil moisture and snow cover are addressed. To make a complete analysis of soil moisture, snow cover, and atmospheric initialization and lateral forcing data (e.g. NAM vs NARR), simulations using NARR and NAM with the two soil moisture initialization alternatives as well as a NARR simulation with standard interpolated soil moisture and an imposed snow level (NARR SNO) are planned for future work.

Problems common to all simulations include the tendency to smooth out sharp elevated inversions, under-predict nighttime surface temperatures, and consequently lag behind the observations in predicting the onset and development of the surface mixed layer after sunrise. Future work could also include an investigation into turbulence parameterizations and surface flux formulations to provide some insight into the cause of these model discrepancies. Specification of lateral boundary forcing may also prove to be important [*Warner et al.*, 1997; *Nutter et al.*, 2004].

The ten simulations presented here have shown that ARPS is sensitive to soil moisture and snow cover initialization and that even when soil moisture is approximated in an average sense using measured values from the observation site, the simulation performs significantly better than with soil moisture data from a coarse dataset such as NAM or NARR (with the exception of IOP6 using NAM). Predictions from both sets of simulations improved as the grid resolution was refined (not shown). A comprehensive dataset described in Chapter 5 was created to initialize the land-surface model used by ARPS and other codes, as well as to evaluate the evolution of the soil properties as simulations progress. Generation of initial soil moisture fields for different grid resolutions and domain sizes was addressed in Chapter 2.

In addition to improved initialization data, efforts are needed to improve the current land-

surface models which are coupled to meso-scale codes. Most land-surface models do not allow for lateral flow of water. Thus rain accumulated on the steep Sierra slopes will not flow to the valley floor because each grid cell is completely isolated. Future work may include further investigations employing the coupled hydrologic model, PF.CLM described in Chapter 3 of this dissertation and used in the study by *Chow et al.* [2006a] which does allow for surface runoff and three-dimensional subsurface groundwater flow.

# Chapter 7

# Concluding Remarks

This dissertation seeks to quantify the effects of surface soil moisture initialization on simulations of atmospheric boundary layer (ABL) flow over complex terrain as well as explore options for providing more accurate surface initialization data for mesoscale models. A combination of numerical simulations using the Advanced Regional Prediction System (ARPS), a mesoscale atmospheric model, and PF.CLM, a coupled hydrologic model, as well as field observations are employed to address these issues for the region of complex terrain of Owens Valley, California. Owens Valley was the site of the Terrain-Induced Rotor Experiment (T-REX) which took place in March and April of 2006 and provided a wide range of observations for comparison to simulations. Results of a sensitivity study indicate strong sensitivity to soil moisture initialization under both weak and strong synoptic forcing. Simulations of both the ABL and the coupled land-surface-surface water-groundwater system have been performed and the results compared to observations. Results show that more accurate surface soil moisture initialization based on soil moisture observations and the results of coupled hydrologic modeling yields clear improvements in comparisons of simulations to observations under calm wind conditions. Simulations performed under strong meteorological forcing show some improvement depending on the initialization dataset.

Chapter 2 describes a sensitivity study where high-resolution simulations (350 m horizontal grid spacing) are performed under weak and strong meteorological forcings with fully saturated (wet) and zero soil moisture (dry) initializations. Both the quiescent and the strongly-forced cases show keen sensitivity to soil moisture based on heat budget analysis and comparisons of potential temperature, turbulent kinetic energy, and specific humidity. Specifically, a 24-hour average difference of 2 K in potential temperature at the surface between wet and dry simulations was found in both the weak and strong forcing cases. This result was not expected for the strong forcing case because it has generally been thought (based on a large body of research focused on flat terrain) that surface conditions do not significantly affect flow in the ABL under strong forcing. Simply changing the soil moisture initialization in these simulations over complex terrain leads to major differences in the dynamics and structure of the flows in each case and provides evidence of the need for more accurate soil moisture data for initialization of mesoscale atmospheric models.

Chapter 3 addresses the issue of obtaining more accurate high-resolution soil moisture data through the use of coupled hydrologic modeling. Both two-dimensional and three-dimensional simulations are performed using the groundwater model ParFlow coupled to the land-surface model,

the Common Land Model, CLM. Results of two 2D multi-year spin-up simulations are presented and compared to soil moisture observations from T-REX (described in Chapter 5). The 2D simulations are able to capture the general trend in a transect of soil moisture observations, specifically the region of increased soil moisture near the Owens River and the increase in soil moisture higher up the slopes of the mountains. Results of a partial (3-month) spin-up of the 3D simulation are presented and indicate that the choice of altitude-dependent soil moisture for initialization of atmospheric simulations based on results of the 2D spin-ups is appropriate for Owens Valley or similar catchments.

In Chapter 4, flow routing is addressed through the introduction of a novel algorithm. Overland flow routing for the 3D PF.CLM simulations is problematic due to the fact that the Owens River is too narrow to be resolved on a 350 m grid. Current flow direction enforcement algorithms for routing across flat areas are mostly commercial and operate only in the context of ESRI ARC-GIS. Available programs are not general enough to be used in the context of PF.CLM due to constraints on flow direction which are intrinsic to the model's overland flow module. The algorithm presented in this chapter takes stream location data, maps it to a model grid, then delineates a continuous flow path along a streamline by ensuring that all slopes along the flow path point to a down-stream neighboring cell. Employing this flow direction enforcement algorithm as a pre-processing step for the 3D PF.CLM simulations is key to obtaining realistic soil moisture distribution results from the simulations. This algorithm is general and may be applied in a variety of other contexts to achieve more realistic flow networks in hydrologic modeling.

Chapter 5 describes the soil moisture measurements obtained during T-REX as well as the procedure used to calibrate observations from the capacitance probes using gravimetric measurements. Observations from the capacitance probes show that the probes are able to capture increases in soil moisture following precipitation events, as well as increases in soil moisture high on the slopes of the Sierras most likely due to snow melting on warmer days. Observations of soil moisture described in this chapter are used to validate the coupled hydrologic modeling in Chapter 3 as well as select more accurate soil moisture initialization values for realistic simulations of atmospheric flow described in Chapter 6. Thus field observations are critical in determining more accurate initial soil moisture for mesoscale atmospheric models.

The final chapter (Chapter 6) describes a set of ten simulations with comparisons to observations from T-REX. Standard North American Mesoscale model (NAM) 12 km data as well as North American Regional Reanalysis (NARR) 32 km data are used to initialize ARPS for two observing periods: one quiescent and the other strongly forced. In addition to the standard NAM and NARR soil moisture and snow cover initializations, altitude-dependent soil moisture based on the results of PF.CLM simulations as well as a simple uniform adjustment provide two more accurate soil moisture initialization cases. All simulations capture the main characteristics of the flow, but there is significant variation among simulations. More accurate soil moisture initialization yields a clear improvement in comparisons of simulations to observations for the quiescent case. For the strongly forced case, there is clear improvement between the standard NARR and the more accurate adjusted soil moisture initializations, but not between standard NAM and the altitude-dependent soil moisture initialization. Simulations performed with the standard interpolated initial NAM soil moisture and an imposed snow level showed intermediate improvement for the queiscent case compared to the simulations in which both soil moisture and snow cover were addressed, while no definitive improvement can be seen for the strong forcing case. Better methods for comparison to observations may be important under strong forcing since radiosondes may be blown far from their

launch points and there may be considerable spatial and temporal variation in measured quantities under rotor flow conditions.

## 7.1 Summary and recommendations

In summary, model sensitivity to soil moisture initialization is demonstrated using ARPS for simulations of atmospheric boundary layer flow under both strong and weak synoptic forcing. Standard initialization data is too coarse to resolve a topographic feature the size of Owens Valley, thus using more accurate soil moisture and snow cover initialization data yields clear improvement in comparisons of simulations to observations in most cases. Coupled hydrologic modeling can provide more accurate high-resolution soil moisture for simulations of ABL flow, and even simple 2D simulations may be sufficient to provide guidence for selecting appropriate altitude-dependent soil moisture bins for a catchment similar to Owens Valley which has a quasi-two-dimensional structure. Even in the absence of coupled hydrologic modeling, simple adjustments to initial soil moisture and snow cover based on point measurements can still provide significant improvments in simulation results compared to standard initialization procedures.

Relatively simple and cost-effective methods for measuring soil moisture are available. It is therefore recommended that soil moisture measurements be included as part of field campaigns aimed at understanding flow in the atmospheric boundary layer. Even a few well-chosen measurement sites can provide enough data for simple adjustments to intial model soil moisture, or can be used to validate results of hydrologic modeling so that significant improvements in model performance can be acheived even with very minimal changes to the model set-up.

Future work could include the implementation of a "balloon following" algorithm in ARPS or other mesoscale models for better comparisons to sounding observations under strong forcing conditions. Investigation into the effects of soil moisture intialization, and land-surface heterogeneity in general, in other regions of complex terrain may also be included in future work where generalization of the "weak" versus "strong" threshold may be pursued through scaling analysis.

# Bibliography


Ashby, S. F., and R. D. Falgout, A parallel multigrid preconditioned conjugate gradient algorithm for groundwater flow simulations, *Nuclear Science and Engineering*, *124*, 145–159, 1996.

Banta, R. M., and P. T. Gannon, Influence of soil moisture on simulations of katabatic flow., *Theor. Appl. Climatol.*, *52*(1/2), 85 – 94, 1995.

Buettner, K. J., and N. Thyer, Valley winds in the Mount Rainier Area, *Archiv fuer Meteorologie, Geophysik und Bioklimatologie*, *14*(1), 125–147, 1966.

Chen, F., K. W. Manning, D. N. Yates, M. A. LeMone, S. B. Tries, R. Cuenca, and D. Niyogi, Development of high resolution land data assimilation system and its application to WRF. Paper 22.3, *20th Conf. Wea. Analysis and Forecasting/16th Conf. Num. Wea. Prediction, AMS Ann. Meeting*, p. 5 pages, 2004.

Chow, F. K., R. L. Street, M. Xue, and J. H. Ferziger, Explicit filtering and reconstruction turbulence modeling for large-eddy simulation of neutral boundary layer flow, *J. Atmos. Sci.*, *62*(7), 2058–2077, 2005.

Chow, F. K., S. J. Kollet, R. M. Maxwell, and Q. Duan, Effects of soil moisture heterogeneity on boundary layer flow with coupled groundwater, land-surface, and mesoscale atmospheric modeling. Paper 5.6, *17th Symposium on Boundary Layers and Turbulence, American Meteorological Society*, 2006a.

Chow, F. K., A. P. Weigel, R. L. Street, M. W. Rotach, and M. Xue, High-resolution large-eddy simulations of flow in a steep Alpine valley. Part I: Methodology, verification, and sensitivity studies, *Journal of Applied Meteorology and Climatology*, *45*(1), 63–86, 2006b.

Costa-Cabral, M., and S. Burges, Digital Elevation Model Networks (DEMON) - A model of flow over hillslopes for computation of contributing and dispersal areas, *WATER RESOURCES RESEARCH*, *30*(6), 1681–1692, 1994.

Dai, Y., et al., The Common Land Model, *Bull. Amer. Met. Soc.*, *84*, 1013–1023, 2003.

Daniels, M. H., F. K. Chow, and G. S. Poulos, Effects of soil moisture initialization on simulations of atmospheric boundary layer evolution in Owens Valley. Paper 7.2., *12th Conference on Mountain Meteorology, American Meteorological Society*, 2006.

Daniels, M. H., R. M. Maxwell, and F. K. Chow, Providing high-resolution surface conditions using a coupled land-surface groundwater model: effects on atmospheric boundary layer simulations over Owens Valley, CA. Paper 11A.1, *18th Symposium on Boundary Layers and Turbulence, American Meteorological Society*, p. 9 pp., 2008.

Danskin, W. R., Evaluation of the Hydrologic System and Selected Water-Management Alternatives in the Owens Valley, CA, *Technical Report Water-Supply Paper 2370-H*, United States Geological Survey, 1998.

Deardorff, J. W., Stratocumulus-capped mixed layers derived from a 3-dimensional model, *Bound.-Layer Meteor.*, *18*(4), 495 – 527, 1980.

Doyle, J. D., and D. R. Durran, The dynamics of mountain-wave-induced rotors., *Journal of the Atmospheric Sciences*, *59*(2), 186 – 201, 2002.

Doyle, J. D., and D. R. Durran, Rotor and subrotor dynamics in the lee of three-dimensional terrain, *JOURNAL OF THE ATMOSPHERIC SCIENCES*, *64*(12), 4202–4221, doi:{10.1175/2007JAS2352.1}, 2007.

Fairfield, J., and P. Leymarie, Drainage networks from grid digital elevation models, *WATER RESOURCES RESEARCH*, *27*(5), 709–717, 1991.

Grubisic, V., et al., THE TERRAIN-INDUCED ROTOR EXPERIMENT A Field Campaign Overview Including Observational Highlights, *BULLETIN OF THE AMERICAN METEOROLOGICAL SOCIETY*, *89*(10), 1513+, doi:{10.1175/2008BAMS2487.1}, 2008.

Grubišić, V., and J. P. Kuettner, Sierra rotors and the Terrain-induced Rotor Experiment (T-REX), Paper P2.1, *11th Conference on Mountain Meteorology, American Meteorological Society*, p. 7 pages, 2004.

Grubišić, V., , J. D. Doyle, J. P. Kuettner, G. S. Poulos, and C. D. Whiteman, T-REX: Terrain-induced rotor experiment scientific overview document and experiment design, p. 72 pages, 2004.

Hellweger, F., AGREE - DEM Surface Reconditioning System, `http://www.ce.utexas.edu/prof/maidment/gishydro/ferdi/research/agree/agree.html`, 1997.

Huang, H.-Y., and S. A. Margulis, On the impact of surface heterogeneity on a realistic convective boundary layer, *WATER RESOURCES RESEARCH*, *45*, doi:{10.1029/2008WR007175}, 2009.

Hutchinson, M., A new procedure for gridding elevation and stream line data with automatic removal of spurious pits, *JOURNAL OF HYDROLOGY*, *106*(3-4), 211–232, 1989.

Jiang, Q., and J. D. Doyle, On the diurnal variation of mountain waves, *JOURNAL OF THE ATMOSPHERIC SCIENCES*, *65*(4), 1360–1377, doi:{10.1175/2007JAS2460.1}, 2008.

Jiang, Q., and J. D. Doyle, The Impact of Moisture on Mountain Waves during T-REX, *MONTHLY WEATHER REVIEW*, *137*(11), 3888–3906, doi:{10.1175/2009MWR2985.1}, 2009.

Jones, J. E., and C. S. Woodward, Newton-Krylov-multigrid solvers for large-scale, highly heterogeneous, variably saturated flow problems, *Adv. in Water Resourc.*, *24*, 763–774, 2001.

Kang, S.-L., and K. J. Davis, The effects of mesoscale surface heterogeneity on the fair-weather convective atmospheric boundary layer, *JOURNAL OF THE ATMOSPHERIC SCIENCES*, *65*(10), 3197–3213, doi:{10.1175/2008JAS2390.1}, 2008.

Kenny, F., and B. Matthews, A methodology for aligning raster flow direction data with photogrammetrically mapped hydrology, *COMPUTERS & GEOSCIENCES*, *31*(6), 768–779, doi:{10.1016/j.cageo.2005.01.019}, 2005.

Kenny, F., B. Matthews, and K. Todd, Routing overland flow through sinks and flats in interpolated raster terrain surfaces, *COMPUTERS & GEOSCIENCES*, *34*(11), 1417–1430, doi:{10.1016/j.cageo.2008.02.019}, 2008.

Kollet, S. J., and R. M. Maxwell, Integrated surfacegroundwater modeling: A free-surface overland flow boundary condition in a parallel groundwater flow model, *Adv. in Water Resourc.*, *29*, 945–958, 2006.

Kollet, S. J., and R. M. Maxwell, Capturing the influence of groundwater dynamics on land surface processes using an integrated, distributed watershed model, *Water Resourc. Res.*, *44*(W02402), 2008.

Krajewski, W. F., et al., A remote sensing observatory for hydrologic sciences: A genesis for scaling to continental hydrology, *Water Resources Research*, *42*, W07,301, 2006.

Kuettner, J., The rotor flow in the lee of mountains, *Geophysics Research Directorate Research Notes No. 6, Air Force Cambridge Research Center*, p. 20, 1959.

Liu, Y., F. Chen, T. Warner, S. Swerdlin, . Bowers, and S. Halvorson, Improvements to surface flux computations in a non-local-mixing PBL schemes, and refinements to urban processes in the NOAH land-surface model with NCAR/ATEC real-time FDDA and forecast system. Paper 22.2, *20th Conference on Weather Analysis and Forecasting and 16th Conference on Numerical Weather Prediction, American Meteorological Society*, p. 8 pages, 2004.

Marks, D., J. Dozier, and J. Frew, Automated basin delineation from digital elevation data, *GEOPROCESSING*, *2*(3), 299–311, 1984.

Maxwell, R. M., and N. L. Miller, Development of a Coupled Land Surface and Groundwater Model, *J. Hydromet.*, *6*, 2005.

Maxwell, R. M., F. K. Chow, and S. J. Kollet, The groundwater-land-surface connection: Soil moisture effects on the atmospheric boundary layer in fully-coupled simulations, *Adv. in Water Resourc.*, *30*, 2447–2466, 2007.

McCumber, M. C., and R. A. Pielke, Simulation of the Effects of Surface Fluxes of Heat and Moisture in a Mesoscale Numerical Model., *JGR*, *86*(C10), 9929 – 9938, 1981.

McGowan, H. A., Observations of anti-winds in a deep alpine valley, Lake Tekapo, New Zealand, *Arctic, Antarctic, and Alpine Research*, *36*(4), 495–501, 2004.

Mizgalewicz, P. J., and D. R. Maidment, Modeling agrichemical transport in midwest rivers using geographic information systems, in *Center for Research in Water Resources Online Report 96-6*, pp. 1–338, University of Texas, Austin, TX, 1996.

Moeng, C.-H., A large-eddy-simulation model for the study of planetary boundary-layer turbulence, *J. Atmos. Sci.*, *41*(13), 2052–2062, 1984.

Nutter, P., D. Stensrud, and M. Xue, Effects of coarsely resolved and temporally interpolated lateral boundary conditions on the dispersion of limited-area ensemble forecasts, *Mon. Wea. Rev.*, *132*, 2358–2377, 2004.

O'Callaghan, J., and D. Mark, The extraction of drainage networks from digital elevation data, *COMPUTER VISION GRAPHICS AND IMAGE PROCESSING*, *28*(3), 323–344, 1984.

Ookouchi, Y., M. Segal, R. C. Kessler, and R. A. Pielke, Evaluation of soil moisture effects on the generation and modification of mesoscale circulations., *Mon. Wea. Rev.*, *112*(11), 2281 – 92, 1984.

Orlandini, S., G. Moretti, M. Franchini, B. Aldighieri, and B. Testa, Path-based methods for the determination of nondispersive drainage directions in grid-based digital elevation models, *WATER RESOURCES RESEARCH*, *39*(6), doi:{10.1029/2002WR001639}, 2003.

Patton, E. G., P. P. Sullivan, and C.-H. Moeng, The influence of idealized heterogeneity on wet and dry planetary boundary layers coupled to the land surface, *J. Atmos. Sci.*, *62*, 2078–2097, 2005.

Press, W. H., S. A. Teukolsky, W. T. Vetterling, and B. P. Flannery, *Numerical Recipes in Fortran 77, Second Edition, The Art of Scientific Computing*, Cambridge University Press, 1999.

Rampanelli, G., D. Zardi, and R. Rotunno, Mechanisms of up-valley winds, *J. Atmos. Sci.*, *61*(24), 3097–3111, 2004.

Reinecke, P. A., and D. Durran, The Overamplification of Gravity Waves in Numerical Solutions to Flow over Topography, *MONTHLY WEATHER REVIEW*, *137*(5), 1533–1549, doi:{10.1175/2008MWR2630.1}, 2009.

Ren, D., and M. Xue, A revised force-restore model for land-surface modeling, *J. Appl. Meteor.*, *43*(11), 1768–1782, 2004.

Reuten, C., D. G. Steyn, K. B. Strawbridge, and P. Bovis, Observations of the relationship between upslope flows and the convective boundary layer in steep terrain, *Bound.-Layer Meteor.*, *116*, 37–61, 2005.

Saunders, W., and D. Maidment, A GIS assessment of nonpoint source pollution in the San AntonioNueces coastal basin, in *Center for Research in Water Resources Online Report 96-1*, pp. 1–222, University of Texas, Austin, TX, 1996.

Schmidli, J., G. S. Poulos, M. H. Daniels, and F. K. Chow, External Influences on Nocturnal Thermally Driven Flows in a Deep Valley, *JOURNAL OF APPLIED METEOROLOGY AND CLIMATOLOGY*, *48*(1), 3–23, doi:{10.1175/2008JAMC1852.1}, 2009.

Smith, C. M., and E. D. Skyllingstad, Investigation of Upstream Boundary Layer Influence on Mountain Wave Breaking and Lee Wave Rotors Using a Large-Eddy Simulation, *JOURNAL OF THE ATMOSPHERIC SCIENCES*, *66*(10), 3147–3164, doi:{10.1175/2009JAS2949.1}, 2009.

Steinwand, A., R. Harrington, and D. Or, Water balance for Great Basin phreatophytes derived from eddy covariance,soil water, and water table measurements, *JH*, *329*, 595–605, 2006.

Tarboton, D., A new method for the determination of flow directions and upslope areas in grid digital elevation models, *WATER RESOURCES RESEARCH*, *33*(2), 309–319, 1997.

Tewari, M., et al., Implementation and verification of the unified NOAH land surface model in the WRF model, *Bulletin of the American Meteorological Society*, pp. 2165 – 2170, 2004.

Warner, T. T., R. A. Peterson, and R. E. Treadon, A tutorial on lateral boundary conditions as a basic and potentially serious limitation to regional numerical weather prediction., *Bull. Amer. Met. Soc.*, *78*(11), 2599 – 617, 1997.

Weigel, A. P., F. K. Chow, M. W. Rotach, R. L. Street, and M. Xue, High-resolution large-eddy simulations of flow in a steep Alpine valley. Part II: Flow Structure and Heat Budgets, *Journal of Applied Meteorology and Climatology*, *45*(1), 87–107, 2006.

Whiteman, C. D., *Mountain meteorology: fundamentals and applications*, 355 pp., Oxford University Press, New York, 2000.

Xue, M., K. K. Droegemeier, and V. Wong, The Advanced Regional Prediction System (ARPS): A multi-scale nonhydrostatic atmospheric simulation and prediction model. Part I: Model dynamics and verification, *Meteor. Atmos. Phys.*, *75*(3-4), 161–193, 2000.

Xue, M., K. K. Droegemeier, V. Wong, A. Shapiro, K. Brewster, F. Carr, D. Weber, Y. Liu, and D. Wang, The Advanced Regional Prediction System (ARPS): A multi-scale nonhydrostatic atmospheric simulation and prediction tool. Part II: Model physics and applications, *Meteor. Atmos. Phys.*, *76*(3-4), 143–165, 2001.

Xue, M., D. Wang, J. Gao, K. Brewster, and K. K. Droegemeier, The Advanced Regional Prediction System (ARPS), storm-scale numerical weather prediction and data assimilation, *Meteorology and Atmospheric Physics*, *82*(1/4), 139 – 70, 2003.

# Appendix A

# Field measurements of soil moisture during T-REX

This appendix contains selected soil moisture and soil temperature data collected during the Terrain-Induced Rotor Experiment, as well as photographs of the selected sites. Tables of site coordinates, soil types, and corresponding calibration for each site are given at the end. Chapter 5 contains references and discussion of field measurements, including the data presented here.

(a)

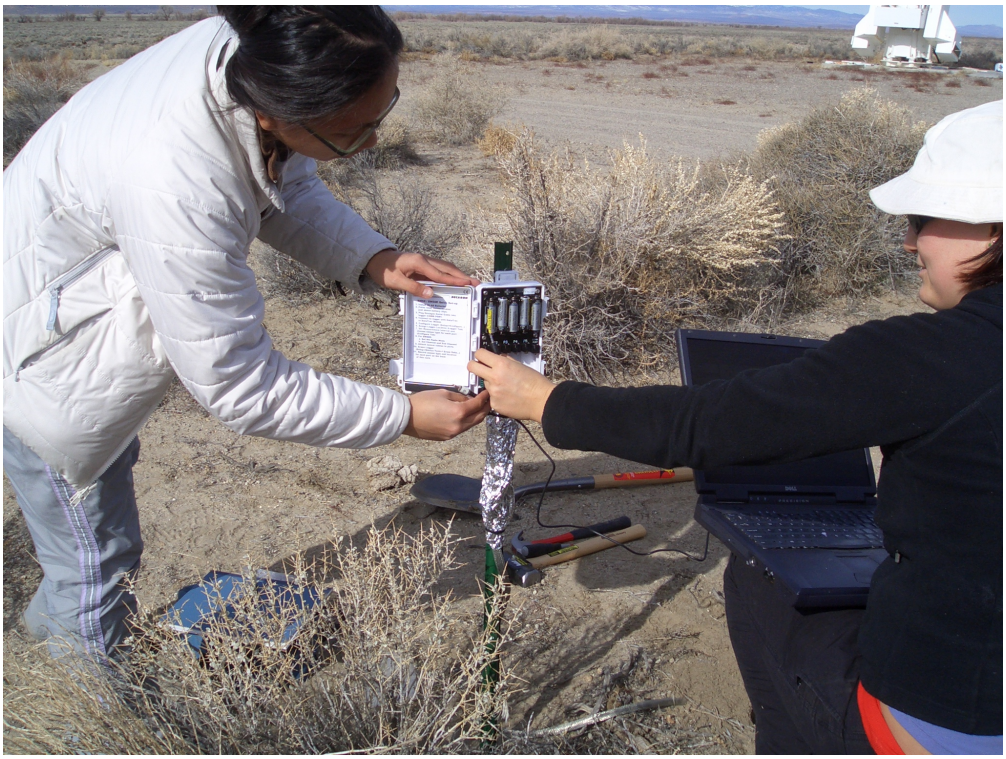

(b)

Figure A.1. (a) Looking west from S1. (b) Datalogger attached to buried sensor at S1.

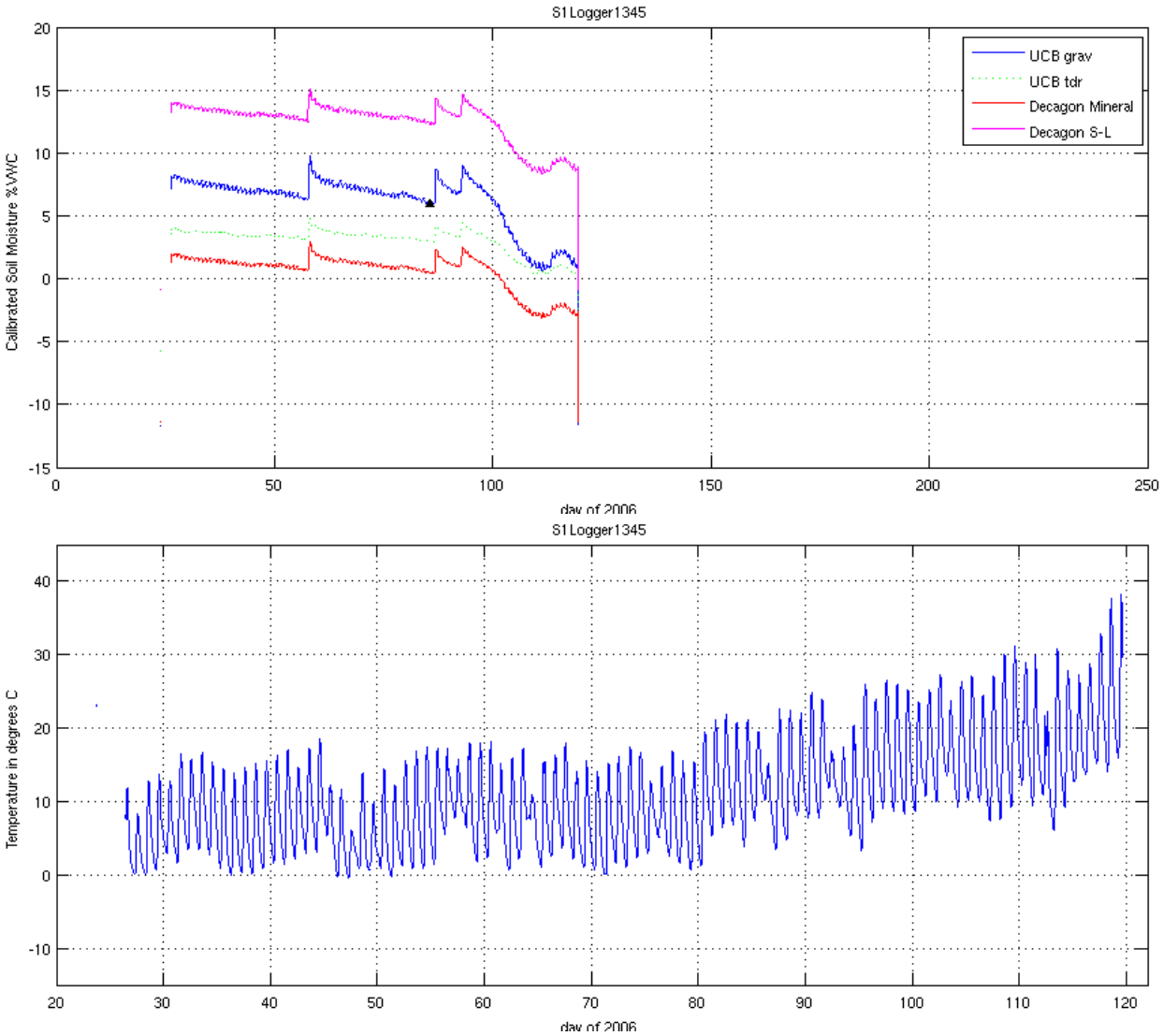


Figure A.2. Soil moisture and soil temperature at S1. We only took one set of gravimetric measurements for this site.

(a)

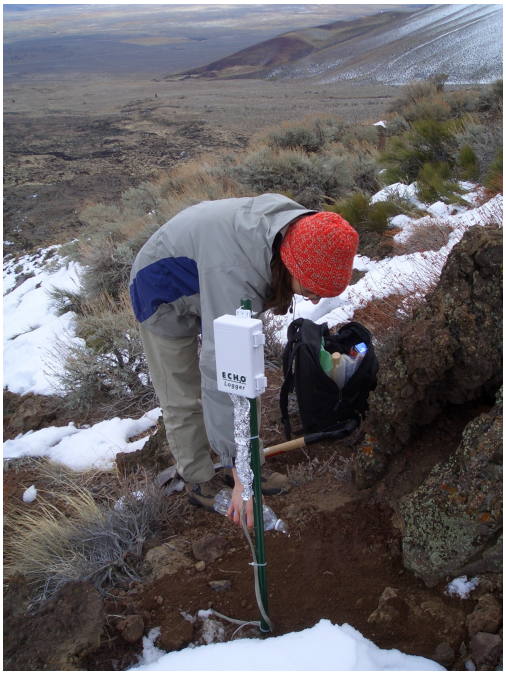


(b)

Figure A.3. (a) Looking southeast from S2. (b) Datalogger attached to buried sensor at S2.

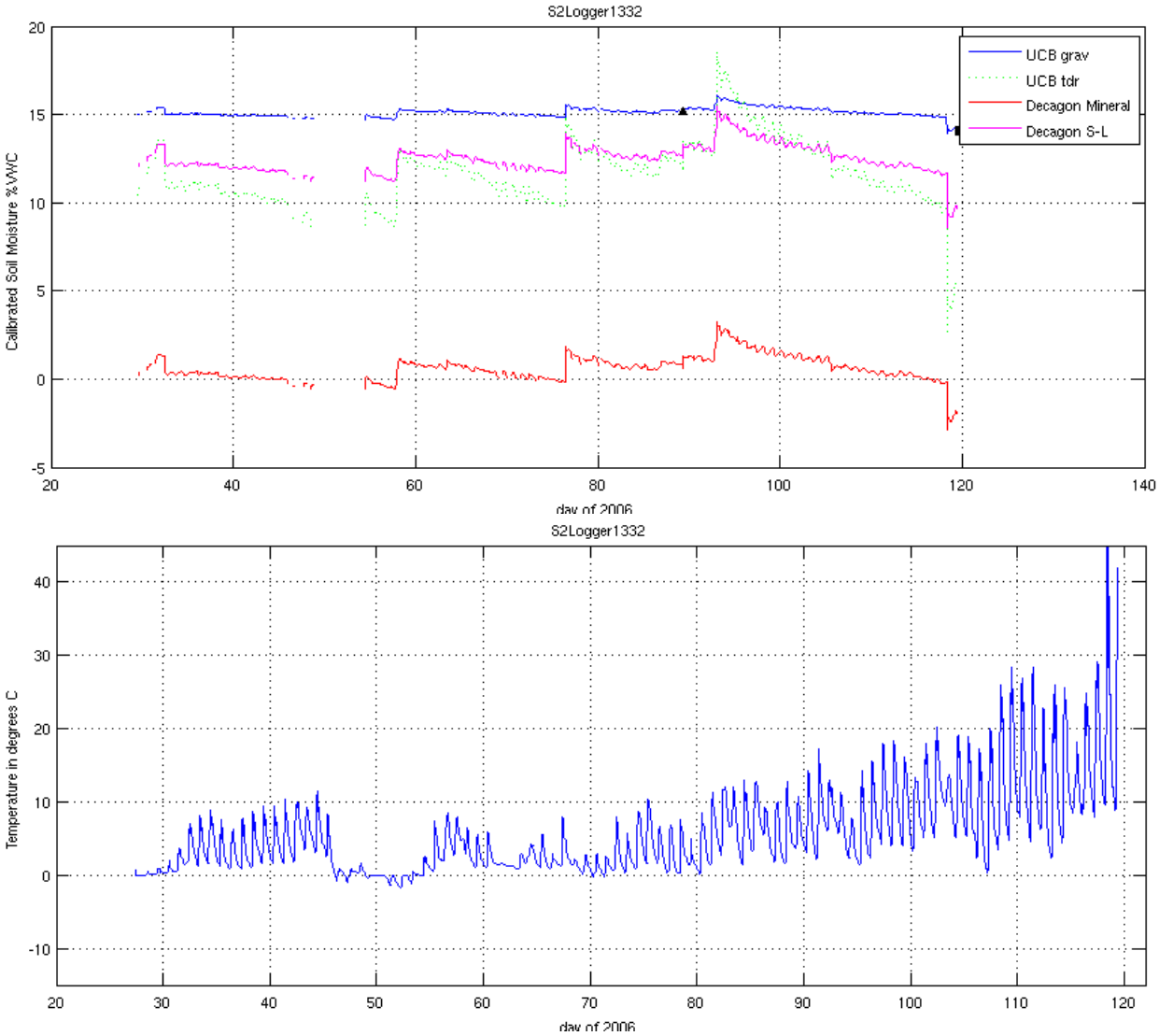


Figure A.4. Soil moisture and soil temperature at S2.

(a)

(b)

Figure A.5. (a) Looking west from S11, (DRI weather station tower, colocated). (b) Installing sensors at S11.

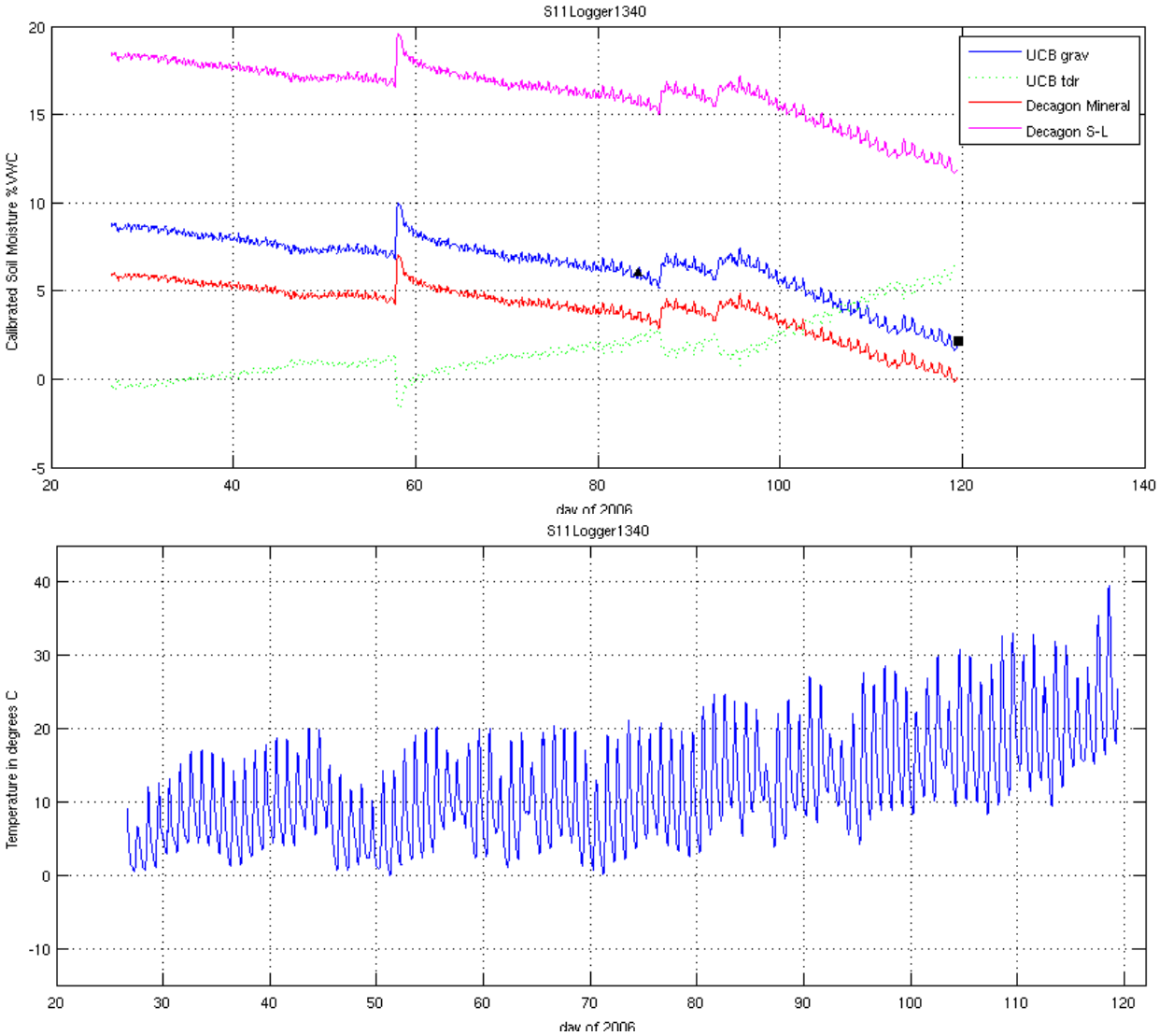


Figure A.6. Soil moisture and soil temperature at S11.

(a)

(b)

Figure A.7. (a) Looking west from S16. (b) Looking south from S16.

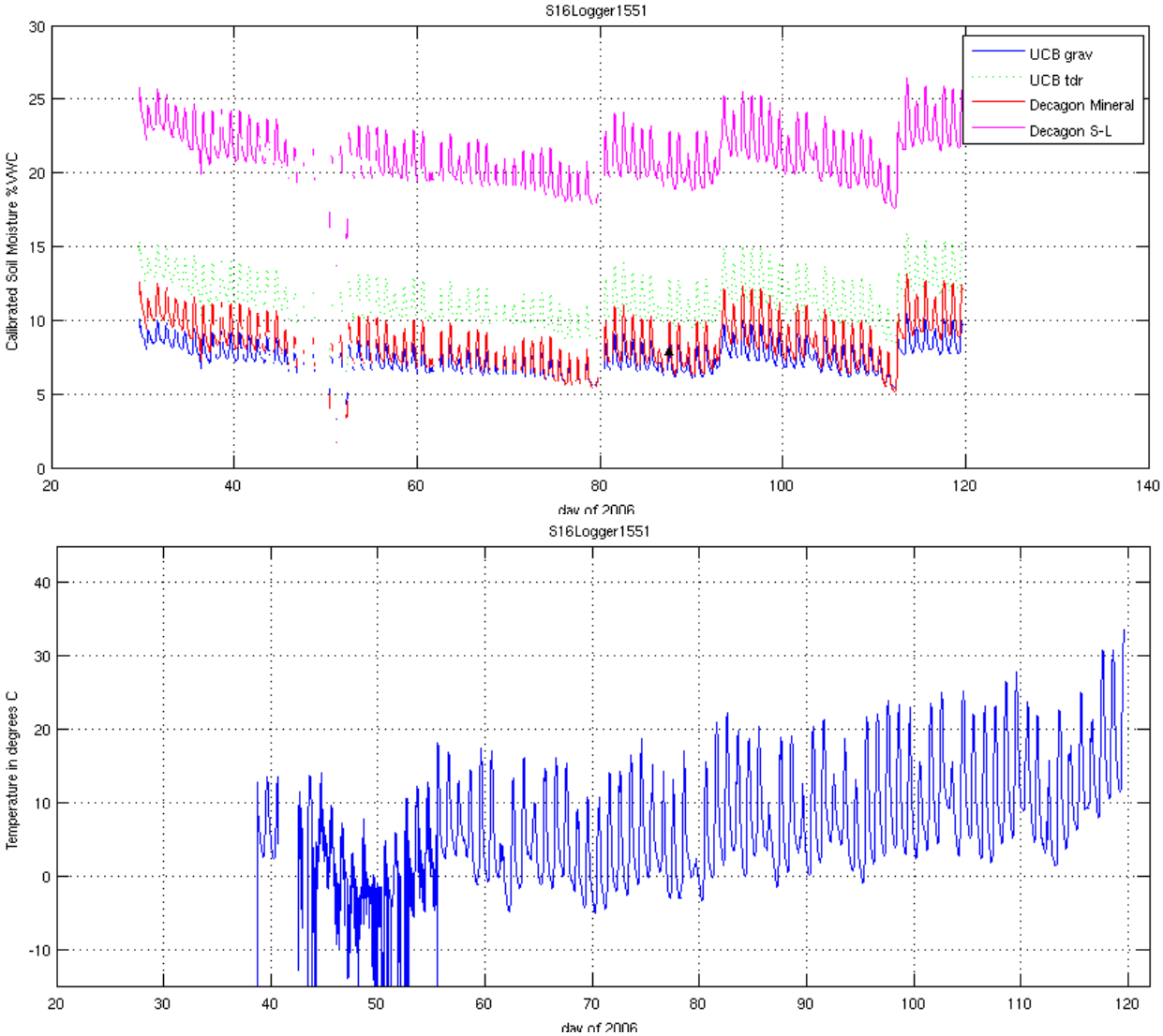


Figure A.8. Soil moisture and soil temperature at S16. Below freezing temperatures appear to have caused spurious temperature readings, though according to Decagon the temperature probe should have been capable of functioning normally in the range of temperatures from -40 °C to 60 °C. We only took one set of gravimetric measurements for this site.

| Site | Logger | Elevation (ft) | Latitude (degrees, minutes) | | Longitude (degrees, minutes) | | Latitude (degrees) | Longitude (degrees) |
|---|---|---|---|---|---|---|---|---|
| S1 | 1345 | 3971 | 37 | 14.000 | 118 | 17.266 | 37.233 | 118.288 |
| S2 | 1332 | 6360 | 36 | 56.901 | 118 | 19.561 | 36.948 | 118.326 |
| S3 | 1342 | 3835 | 36 | 57.576 | 118 | 13.843 | 36.960 | 118.231 |
| S4 | 1445 | 3900 | 36 | 52.477 | 118 | 14.480 | 36.875 | 118.241 |
| S5 | 1333 | 3834 | 36 | 53.219 | 118 | 14.191 | 36.887 | 118.237 |
| S6 | 1446 | 6643 | 36 | 55.109 | 118 | 6.631 | 36.918 | 118.111 |
| S8a* | 1339 | 6766 | 36 | 47.411 | 118 | 18.063 | 36.790 | 118.301 |
| S8b* | 1334 | | | | | | | |
| S8* | 1440 | | | | | | | |
| S9 | 1338 | 5697 | 36 | 46.098 | 118 | 16.566 | 36.768 | 118.276 |
| S10 | 1348 | 4842 | 36 | 46.668 | 118 | 14.598 | 36.778 | 118.243 |
| S11a* | 1340 | 4180 | 36 | 47.184 | 118 | 12.468 | 36.786 | 118.208 |
| S11b* | 1430 | | | | | | | |
| S11c* | 1432 | | | | | | | |
| S11d* | 1439 | | | | | | | |
| S12 | 1341 | 3770 | 36 | 48.043 | 118 | 7.970 | 36.801 | 118.133 |
| S13 | 1435 | 3856 | 36 | 48.766 | 118 | 6.523 | 36.813 | 118.109 |
| S14a* | 1429 | 4870 | 36 | 50.662 | 118 | 5.116 | 36.844 | 118.085 |
| S14b* | 1549 | | | | | | | |
| S15 | 1366 | 7003 | 36 | 51.663 | 118 | 3.571 | 36.861 | 118.060 |
| S16 | 1551 | 7448 | 36 | 51.824 | 118 | 3.190 | 36.864 | 118.053 |
| S17 | 1442 | 5953 | 36 | 41.889 | 118 | 14.778 | 36.698 | 118.246 |
| S18 | 1343 | 4744 | 36 | 43.158 | 118 | 12.254 | 36.719 | 118.204 |
| S19 | 1344 | 3836 | 36 | 43.930 | 118 | 8.821 | 36.732 | 118.147 |
| S20 | 1434 | 4087 | 36 | 45.106 | 118 | 3.176 | 36.752 | 118.053 |
| S22 | 1367 | 5603 | 36 | 35.672 | 118 | 10.333 | 36.595 | 118.172 |
| S23* | 1441 | 3862 | 36 | 36.398 | 118 | 4.600 | 36.607 | 118.077 |
| S23* | 1443 | | | | | | | |
| S24 | 1550 | 3691 | 36 | 37.171 | 118 | 2.053 | 36.620 | 118.034 |
| S25 | 1447 | 4236 | 36 | 38.405 | 117 | 59.763 | 36.640 | 117.996 |

* Indicates multiple sensors at a site

Figure A.9. Site locations and elevations.

| | | | | "Gritty" | | | "Gritty and smooth" | | | "Smooth" | | | | * Indicates multiple sensors at a site |
|---|---|---|---|---|---|---|---|---|---|---|---|---|---|---|
| *Site* | *Logger* | Sand | Loamy Sand | Sandy Loam | Sandy Clay Loam | Sandy Clay | Loam | Clay Loam | Clay | Silt Loam | Silty Clay Loam | Silty Clay | Organic | *Date Sample Taken* |
| S1 | 1345 | • | | | | | | | | | | | | 03/31/06 08:30 AM |
| S2 | 1332 | • | | | | | | | | | | | | 03/28/06 04:09 PM |
| S3 | 1342 | | | | | | | | | | | | • | 03/31/06 12:15 PM |
| S4 | 1445 | | • | | | | | | | | | | | 03/28/06 12:00 PM |
| S5 | 1333 | | | | | | | | | | | | • | 03/28/06 12:00 PM |
| S6 | 1446 | | | | | • | | | | | | | | 03/26/06 11:00 AM |
| S8a* | 1339 | | • | | | | | | | | | | | 03/28/06 01:15 PM |
| S8b* | 1334 | | • | | | | | | | | | | | 03/31/06 10:00 AM |
| S8* | 1440 | | • | | | | | | | | | | | 03/28/06 02:30 PM |
| S9 | 1338 | | | • | | | | | | | | | | 03/26/06 12:00 PM |
| S10 | 1548 | | | • | | | | | | | | | | 03/27/06 04:30 PM |
| S11a* | 1340 | | | • | | | | | | | | | | 03/29/06 11:50 AM |
| S11b* | 1430 | | | • | | | | | | | | | | 03/26/06 01:20 PM |
| S11c* | 1432 | | | • | | | | | | | | | | 03/29/06 02:40 PM |
| S11d* | 1439 | | | • | | | | | | | | | | 03/26/06 11:00 AM |
| S12 | 1341 | | | | | | | • | | | | | | 03/26/06 10:55 AM |
| S13 | 1435 | | | • | | | | | | | | | | 03/28/06 02:45 PM |
| S14a* | 1429 | | | • | | | | | | | | | | 03/28/06 12:55 PM |
| S14b* | 1549 | | | • | | | | | | | | | | 03/26/06 10:50 AM |
| S15 | 1366 | | | | • | | | | | | | | | 03/28/06 12:00 PM |
| S16 | 1551 | | | | | • | | | | | | | | 03/27/06 03:10 PM |
| S17 | 1442 | | • | | | | | | | | | | | 03/31/06 02:00 PM |
| S18 | 1343 | | | • | | | | | | | | | | 03/27/06 05:35 PM |
| S19 | 1344 | | | | | | | | | | | | • | 03/28/06 03:35 PM |
| S20 | 1434 | | • | | | | | | | | | | | 03/28/06 12:15 PM |
| S22 | 1367 | | • | | | | | | | | | | | 03/27/06 05:00 PM |
| S23* | 1441 | | | | • | | | | | | | | | 03/28/06 01:30 PM |
| S23* | 1443 | | | | • | | | | | | | | | 03/29/06 02:35 PM |
| S24 | 1550 | | | • | | | | | | | | | | 03/27/06 06:10 PM |
| S25 | 1447 | | | | • | | | | | | | | | 03/29/06 12:50 PM |

Figure A.10. Soil types corresponding to each site.

| | | Sensor Depth | Calibration Curve | | | |
|---|---|---|---|---|---|---|
| ***Site*** | ***Logger*** | [cm] | *UCB Gravimetric* | *UCB TDR* | *Decagon Mineral* | *Decagon Sandy Loam* |
| S1 | 1345 | 5 | X | | | |
| S2 | 1332 | 5 | X | | | |
| S3 | 1342 | 5 | X | | | |
| S4 | 1445 | 5 | X | | | |
| S5 | 1333 | 5 | | | X | |
| S6 | 1446 | 5 | | | X | |
| S8a* | 1339 | 5 | X | | | |
| S8b* | 1334 | 5 | X | | | |
| S8* | 1440 | 20 | X | | | |
| S9 | 1338 | 5 | X | | | |
| S10 | 1548 | 5 | X | | | |
| S11a* | 1340 | 5 | X | | | |
| S11b* | 1430 | 5 | X | | | |
| S11c* | 1432 | 30 | X | | | |
| S11d* | 1439 | 50 | X | | | |
| S12 | 1341 | 5 | | | X | |
| S13 | 1435 | 5 | X | | | |
| S14a* | 1429 | 5 | X | | | |
| S14b* | 1549 | 20 | X | | | |
| S15 | 1366 | 5 | X | | | |
| S16 | 1551 | 5 | X | | | |
| S17 | 1442 | 5 | X | | | |
| S18 | 1343 | 5 | X | | | |
| S19 | 1344 | 5 | | | | X |
| S20 | 1434 | 5 | X | | | |
| S22 | 1367 | 5 | X | | | |
| S23* | 1441 | 5 | X | | | |
| S23* | 1443 | 20 | NA | NA | NA | NA |
| S24 | 1550 | 5 | | | | X |
| S25 | 1447 | 5 | | | | X |

Figure A.11. Calibration curves corresponding to each site.